Master's thesis

NTNU
Norwegian University of Science and Technology
Faculty of Engineering
Department of Marine Technology

Jonas Ravndal Kildal

Experimental and Numerical Investigation of Coupled Vessel and Moonpool Responses

Master's thesis in Marine Technology
Supervisor: Trygve Kristiansen
June 2020

NTNU
Norwegian University of
Science and Technology

Jonas Ravndal Kildal

Experimental and Numerical Investigation of Coupled Vessel and Moonpool Responses

Master's thesis in Marine Technology
Supervisor: Trygve Kristiansen
June 2020

Norwegian University of Science and Technology
Faculty of Engineering
Department of Marine Technology

NTNU
Norwegian University of
Science and Technology

Preface

This thesis is the final part of my Master of Science degree within Marine Hydrodynamics at the Department of Marine Technology, Norwegian University of Science and Technology (NTNU), Trondheim, Norway. The work is carried out during the spring semester of 2020, with a workload corresponding to 30 ECTS.

The motivation behind the work is related to the sparse amount of coupled moonpool and vessel responses in the literature, and the fact that findings would contribute both in an academic and practical manner.

Even though concepts often are explained from a fundamental point-of-view, the reader of this thesis should be familiar with basic hydrodynamic and moonpool theory.

Trondheim, June 10, 2020, Jonas Ravndal Kildal

Acknowledgement

The present work has been carried out under the supervision of Professor Trygve Kristiansen at the Department of Marine Technology, Norwegian University of Science and Technology (NTNU). I am highly appreciative of his guidance on this thesis. His deep understanding of hydrodynamics and further his ability to easily pass this on are highly appreciated.

The contributions and continuous support of my co-supervisor, Senthuran Ravinthrakumar, have been vital to this thesis. Even though writing his own PhD thesis, he still showed interest in and devoted time to my work, pointing me in the right direction and providing answers when in doubt.

I would also like to address my gratitude to Professor Bernard Molin, providing guidance in the analytical work. Also, the lab technicians Torgeir Wahl, Terje Rosten, Trond Innset and Ole Erik Vinje deserve special recognition. Without them, no model would exist to conduct my experiments on.

J.R.K.

Abstract

The present work investigates coupled moonpool and vessel responses. This is done through experiments and numerical simulations. A parameter study on the moonpool width-to-vessel beam ratio is also conducted. An analytical model is developed to investigate distinct moonpool piston mode periods arising from forced heave and pitch motions in configurations of two and three moonpools.

A literature study is provided, with an emphasis on relevant literature for this thesis. Relevant and fundamental theory regarding moonpools are linear potential flow theory and domain decomposition, which both are outlined in the present work.

The model experiments are conducted with three different moonpool configurations in a model resembling a real ship. The first configuration is of a single moonpool half the model length and half its beam, while the second consist of two square moonpools. The third configuration is of three square moonpools. The experiments were conducted in the laboratory Lilletanken (Small Towing Tank) in head-sea conditions of regular constant-steepness waves. Results, mainly Response Amplitude Operators (RAOs), are compared with numerical simulations. Good agreement is found comparing experiments to numerical simulations and published literature on the single-moonpool configuration. Discrepancies are mainly argued to be non-uniform response time series and coupling between the rigid body motions and moonpool responses.

The presence of sloshing in the single-moonpool configuration distinguishes it's surge response compared to the other two configurations. Relative phases between moonpools in the two- and three-moonpool configuration and the flow separation arising from their piston mode response are argued to be main candidates to explain an observed cancellation in heave.

The potential flow theory solver WAMIT is used in the numerical simulations to replicate the experiments and to conduct the parametric study. WAMIT is also used to verify the presently developed analytical model; whose results show fair agreement compared to numerical simulations.

The parametric study investigates the sensitivity of rigid body motions and moonpool responses with varying moonpool width-to-vessel beam ratio in operational conditions. Four sea states of different peak period and significant wave heights are chosen, based on JONSWAP wave spectra.

Results from the parametric study show sensitivity particularly of the heave motion and moonpool responses with varying moonpool width-to-vessel ratio. A main candidate to explain this behaviour is the increase in wave radiation, due to larger moonpool-to-submerged vessel volume ratio. Apart from the single-moonpool configuration in surge, all three moonpool configurations are relatively unaffected by the varying moonpool width-to-vessel ratio in surge and pitch.

Sammendrag

Denne oppgaven tar for seg den gjensidige koblingen mellom moonpoolrespons og skipsbevegelser, ved gjennomføring av eksperiment og numeriske simuleringer. Et parameterstudie på forholdet mellom moonpoolbredde og skipsbredde er også gjennomført. En analytisk modell er utviklet for å undersøke distinkte piston-mode-perioder som kommer fra tvungne hiv- og stamp-bevegelser i moonpool-konfigurasjoner med henholdsvis to og tre moonpooler.

Et litteraturstudie er gjennomført, med denne oppgaven som bakgrunn. Grunnleggende og relevant teori om moonpooler er lineær potensialteori og domenedekomposisjon, som begge er presentert i denne oppgaven.

Modellforsøkene er gjennomført med tre forskjellige moonpool-konfigurasjoner i en modell som liker et ekte skip. Den første er med én stor moonpool, som er halve lengden og bredden til modellen, mens den andre består av to kvadratiske moonpooler. Den tredje består av tre kvadratiske moonpooler. Eksperimentene er gjennomført i Lilletanken i motsjø som består av regulære bølger med konstant steilhet. Resultat, hovedsakelig RAOer, er sammenlignet med numeriske simuleringer. Gode samsvar ved å sammenligne eksperimentelle resultat med numeriske simuleringer og publisert litteratur på den store moonpoolen er funnet. Avvik er hovedsakelig argumentert til å være ikke-uniforme respons-tidsserier og kobling mellom skipsbevegelsene og moonpoolrespons.

Tilstedeværelsen av sloshing i den store moonpoolen adskiller responsen i jag sammenlignet med konfigurasjonene med to og tre moonpooler. Relative faser mellom moonpoolrespons i konfigurasjonene med to og tre moonpooler og strømnings-separasjon, som kommer fra piston-moden i disse konfigurasjonene, er argumentert å være viktige faktorer som forklarer kansellering i hiv.

Den numeriske potensialteori-løseren WAMIT er brukt til å reprodusere eksperiment og til å gjennomføre parameterstudiet. WAMIT er også brukt til å verifisere den analytiske modellen. Resultat fra denne verifiseringen viser noenlunde gode samsvar mellom den analytiske modellen og numeriske simuleringer.

Parameterstudiet undersøker sensitiviteten til skipsbevegelser og moonpoolrespons med varierende forhold mellom moonpoolbredde og skipsbredde i operasjonelle sjøtilstander. Fire sjøtilstander er valgt; alle basert på JONSWAP-bølgespekter.

Resultat fra parameterstudiet viser særlig sensitivitet i hiv og for moonpoolrespons med varierende forhold mellom moonpoolbredde og skipsbredde. Denne oppførselen kan i stor grad skyldes økende bølgeradiasjon, som forekommer ved økende forhold mellom moonpool-volum og neddykket skipsvolum. Foruten konfigurasjonen med én moonpool, så er alle tre moonpool-konfigurasjoner relativt lite påvirket av forholdet mellom moonpoolbredde og skipsbredde i jag og stamp.

Table of Contents

Nomenclature

Acronyms

BF	Body-fixed
BVP	Boundary value problem
COG	Center of gravity
DOF	Degree of freedom
EF	Earth-fixed
JONSWAP	Joint North Sea Wave Project
RAO	Response Amplitude Operator
VCG	Vertical center of gravity
WAMIT	WaveAnalysisMIT

Greek Letters

η	Rigid body motion
λ	Wave length
Ω	Fluid domain
ω	Angular frequency
ω^*	Non-dimensional angular frequency
ρ	Density of fluid
σ	Standard deviation
φ	Velocity potential

ζ	Free-surface or wave elevation	

Roman Letters

$_a$	Subscript denoting amplitude	
B	Beam of vessel	
b	Moonpool width	
g	Gravitational acceleration	$9.81\ \mathrm{ms}^{-2}$
h	Water depth	
$H(\omega)$	Transfer function, RAO	
H_S	Significant wave height	
k	Wave number	
l	Moonpool length	
L_{pp}	Length of vessel	
$S_\eta(\omega)$	Response spectrum for rigid body motions	
$S_\zeta(\omega)$	Response spectrum for moonpool free-surface elevation	
$S_\zeta(\omega)$	Wave spectrum, herein JONSWAP	
T	Wave or forcing period	
T_p	Spectral peak period	
w	Vertical fluid velocity	
x, y, z	Spatial coordinates	

Chapter 1

Introduction

A moonpool is a vertical opening down to the free-surface in the ship structure. The idea behind moonpools is quite simple: sheltered from environmental loads, for example wind and waves, the moonpool provides safe conditions during marine operations. Current usage of moonpools include offloading of objects such as remotely operated vehicles and diving bells, or to lower risers and umbilicals into the sea.

A problem encountered when using moonpools is the exhibition of resonant modes. These are of importance and can be of concern to both crew and equipment during marine operations. The resonant modes are referred to as piston or sloshing modes, that is, a near-uniform vertical oscillation of the free-surface and standing waves, respectively.

In recent years, the amount of research towards moonpool dynamics have been increasing, but the literature on the mutual interaction between vessel and moonpool responses remain rather sparse. An attempt is thus made to further highlight the importance of understanding these phenomena as well.

1.1 Literature Review

This section will outline published research on moonpools and moonpool dynamics, with an emphasis on applicability towards this thesis. A selection of these will be presented in Chapter 2.

One of the earliest research on moonpools is conducted by Albers (1984), which described the water column inside the moonpool analogously with a damped mass-spring system. He found that the equation of motion *"appeared to be very useful for understanding the behaviour of the water column in the moonpool"*. The results are validated by experiments, with very good agreement. The author highlights the importance of applying empirical values for the quadratic damping if one is to simulate the moonpool motion. This is seen in the numerical simulations in this thesis. Damping plates at the moonpool inlet are also discussed, but is of no interest for this thesis, and will not be discussed further.

Molin (2001) used linearized potential theory and domain decomposition to find analytical expressions of the natural sloshing frequencies and their mode shapes in rectangular

moonpools. Decomposition of the fluid domain into two sub-domains is done; the moonpool and the semi-infinite domain below the keel of the idealized barge, which in the analysis is assumed of infinite length and beam. The water depth is assumed to be infinite. These constraints are all later relaxed by Molin et al. (2018) to finite length and beam of the barge, as well as finite water depth.

Miles (2002) formulated an approach to the eigenvalue problem for slow oscillations in a set of N cylindrical wells. Here, the depth of the wells are assumed large relative to their width, such that the piston mode is assumed the only occurring mode, or, the dominating mode. Comparison with Molin (2001) showed good results in terms of the natural frequencies in a single circular well of the same cross-sectional area, as long as the rectangular moonpool has a moderate aspect ratio.

Several numerical studies, often compared with experiments, are conducted on vessels with single moonpools. Faltinsen et al. (2007) applied vortex-tracking and domain decomposition to the piston mode motion formed by two rectangular hulls. The scheme, though applying linear potential flow, captures the singular behaviour of the velocity potential at the moonpool inlet corners, which in linear potential flow theory isn't captured. Discrepancies between the numerical scheme and dedicated experiments were believed to be free-surface non-linearities, which later was supported by Faltinsen et al. (2015). Fredriksen et al. (2015) used two numerical methods, both a combination of potential and viscous flow. The results compares well with experimental data, where the numerical scheme applying fully non-linear free-surface and body-boundary conditions shows better results than the scheme using linear boundary conditions.

The Master's thesis of Reiersen (2016) aimed to investigate the effect of pitch cancellation in a body consisting of two moonpools. Two-dimensional experiments were conducted with a single moonpool, arguing that the flow fields are similar around the symmetry line in-between the two moonpools. It was found to be cancellation both in heave and in pitch.

Ravinthrakumar et al. (2019) conducted experiments on a quasi three-dimensional body with a single mooonpool, and compared the results with linear potential flow solvers as well as a Navier-Stokes solver. Over-prediction of the response was found using linear potential flow solvers, but the results from the Navier-Stokes solver compared well with experiments. Coupling between the heave, pitch and moonpool responses is observed, with a shift in the piston mode period in freely floating condition compared to forced heave.

(Ravinthrakumar et al., 2020) investigated the hydrodynamic coupling between ship and moonpool, by conducting dedicated three-dimensional experiments with different moonpool sizes. The coupling is found strongest with larger moonpool volume to submerged ship volume ratio.

1.2 Scope of Work and Objectives

The scope in this thesis is to investigate the coupled moonpool and vessel responses on different moonpool configurations. In this respect, one large and two configurations of two and three smaller moonpools are designed.

To further define the scope of the current work, the following objectives are decided upon:

1. Get acquainted with and understand relevant theory on moonpools and moonpool dynamics.
2. Experimentally investigate the coupling of moonpool responses and rigid body motions for the different moonpool configurations.
3. Carry out a numerical study in the moonpool width-to-vessel beam ratio in terms of moonpool responses and rigid-body motions in operational conditions.
4. Develop an analytical model to predict the coupled piston mode periods for the two- and three-moonpool configuration.
5. Make use of numerical simulations as a verification tool in the experimental and analytical work.

1.3 Limitations

This section list relevant limitations and, if applicable, justifications.

- Moonpools using baffles and recess are not considered. The effects of these are available in the literature, and it would be difficult to sort out phenomena directly connected to the scope of this thesis.
- Head sea and freely-floating conditions are applied in the experimental work. That is, the rigid body motions of interest are surge, heave and pitch.
- As a consequence of the head sea conditions (and later obtained experimental results), only longitudinal sloshing modes will be/are present, referred to only as sloshing modes in the thesis.
- Due to small time frame in the experiments, no parametric experimental study is carried out.
- Secondary resonance is not considered, that is, not included in the post-processing and the results.
- Though included in the results, M0 (the none-moonpool comparable vessel) is included for the reader to compare, and is rarely mentioned in the findings of the thesis.

1.4 Approach

The work in relation to this thesis started in the autumn semester of 2019, with a preparatory project report. The model was designed and finalised in the first weeks of 2020, when the almost eight-week long experimental study were conducted. A great amount of time in the beginning was spent to prepare and test the newly-installed wavemaker.

After the experiments, effort was put into post-processing of the results, while also preparing and conducting numerical simulations. Then, time and effort was put into the analytical model and the parametric study.

1.5 Structure of the Thesis

Chapter 2 describe relevant theory in relation to this thesis.

Chapter 3 describe the development of the analytical model. Results, applied on the two- and three-moonpool configuration, are therein included, and not in Chapter 7.

Chapter 4 outline the usage of WAMIT in relation to this thesis. A brief description of WAMIT is given, and different limitations are mentioned.

Chapter 5 present the model experiments and post-processing methodology, including an error source discussion.

Chapter 6 describe the parametric study and the methodology behind it.

Chapter 7 present the experimental and parametric study results, divided in distinct sections and discussed thereafter.

Chapter 8 provide a summarising conclusion and recommendations for further work.

Chapter 2

Theory

This chapter will give important theoretical background in the context of this thesis. Some of this theory is also presented in Kildal (2019), the project thesis connected to this thesis.

Section 2.1 presents theory on linear potential flow theory applicable to this thesis. Section 2.2 outline the procedure of Molin (2001) and the use of domain decomposition to find the natural piston mode period. Section 2.3 briefly present theory on the constant-steepness regular waves used in this thesis' experiments. Section 2.4 present basic sloshing modes. Section 2.5 present a theoretical study on the influence of the surface tension on the natural sloshing modes applicable to this thesis' moonpools.

2.1 Potential Flow Theory

This section will give a brief overview of potential flow theory, because, as drawn from Section 1.1, it is the preferred numerical solution method working on moonpool problems, either by itself or coupled with viscid solvers. Figure 2.1 provides a two-dimensional sketch of the boundary value problem (BVP) used to solve linear (and if desirable - higher order) potential flow problems, illustrating the problem regarding a barge with a moonpool. The theory on potential theory follows the deduction given in Faltinsen (1990).

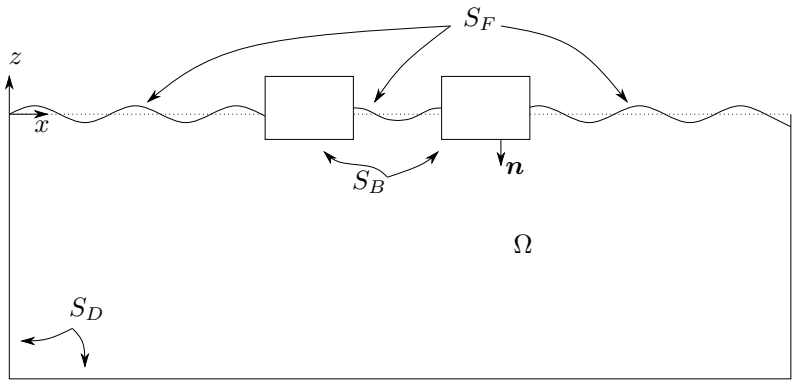

Figure 2.1: Potential flow theory fluid domain. The fluid domain Ω is bounded by the boundaries S_D, free-surface boundary S_F and body boundaries S_B. $\boldsymbol{n}$ is the normal vector on the boundaries.

In potential flow theory, the fluid is assumed incompressible and inviscid, i.e. no change in it's density and no shear forces acting on the fluid elements, respectively. The fluid motion is also assumed irrotational, that is, the flow has zero vorticity. The velocity potential φ is then connected to the fluid velocity vector $\boldsymbol{u}$ through $\boldsymbol{u} = \nabla\varphi$, where ∇ is the nabla operator. Since the fluid is assumed incompressible, the velocity potential has to satisfy the Laplace equation

$$\nabla^2\varphi = 0 \qquad \text{in } \Omega \tag{2.1}$$

To obtain the free-surface elevation or the forces acting on the body, for instance, we have to know φ. This is done by solving Equation (2.1) subject to boundary conditions applying on the boundaries shown in Figure 2.1.

Kinematic boundary condition

On the boundaries S_B, S_D and S_F we have the kinematic boundary condition, that is, that no fluid is to enter or leave through the solid boundaries (S_B and S_D) or a fluid particle on the free-surface stays on the free-surface (S_F). The kinematic boundary conditions on the solid boundaries can be generalized to

$$\frac{\partial\varphi}{\partial n} = \boldsymbol{u}\cdot\boldsymbol{n} \tag{2.2}$$

where $\boldsymbol{n}$ is the normal vector on the boundary, normally positively defined into the fluid.

If we are to define the free-surface as

$$z = \zeta(x,t) \tag{2.3}$$

where ζ is the wave elevation, and subsequently define

$$F(x,z,t) = z - \zeta(x,t) = 0 \tag{2.4}$$

we can write the kinematic boundary condition on the free-surface as

$$\frac{\partial \zeta}{\partial t} + \frac{\partial \varphi}{\partial x}\frac{\partial \zeta}{\partial x} - \frac{\partial \varphi}{\partial z} = 0 \qquad \text{on } S_F \tag{2.5}$$

Dynamic boundary condition

On the free-surface, we also have the dynamic boundary condition, stating that the water pressure is equal to the atmospheric pressure on the free-surface. The pressure in the fluid is given by Bernoulli's equation,

$$p + \rho g z + \rho \frac{\partial \varphi}{\partial t} + \frac{\rho}{2}\left[\left(\frac{\partial \varphi}{\partial x}\right)^2 + \left(\frac{\partial \varphi}{\partial z}\right)^2\right] = C \tag{2.6}$$

where p is the pressure in the fluid, ρ is the density of the fluid and z is the vertical coordinate of the fluid particle according to Figure 2.1. C is an arbitrary function of time, but is regarded an constant as we include it's time dependency in φ. Evaluating Equation (2.6) at $z = 0$, dividing all terms by ρ and assuming zero fluid motion, we get $p/\rho = C$. Thus, by choosing the constant $C = p_0/\rho$, p_0 being the atmospheric pressure, the dynamic boundary condition can be written as

$$g\zeta + \frac{\partial \phi}{\partial t} + \frac{1}{2}\left(\left(\frac{\partial \varphi}{\partial x}\right)^2 + \left(\frac{\partial \varphi}{\partial z}\right)^2\right) = 0 \qquad \text{on } S_F \tag{2.7}$$

Linearization of the BVP

As they are written now, the kinematic and dynamic free-surface boundary conditions, Equations (2.5) and (2.7), are non-linear, and would require large amounts of computational power to solve. They are therefore Taylor-expanded from the instantaneous free-surface position at S_F, $z = \zeta(x,t)$, to the mean free-surface at $z = 0$. The meaning of *linearized* potential theory is only to keep the linear terms of the expansion and disregard the higher-order ones. The kinematic and dynamic free-surface condition is then given from

$$\frac{\partial \zeta}{\partial t} = \frac{\partial \varphi}{\partial z} \qquad \text{on } z = 0 \tag{2.8}$$

and

$$g\zeta + \frac{\partial \varphi}{\partial t} = 0 \qquad \text{on } z = 0, \tag{2.9}$$

respectively. They are further combined to give

$$\frac{\partial^2 \varphi}{\partial t^2} + g\frac{\partial \varphi}{\partial z} = 0 \qquad \text{on } z = 0, \tag{2.10}$$

and, if we are to assume that φ is oscillating harmonically in time with circular frequency ω, the combined free-surface condition, Equation (2.10), can be written as

$$-\omega^2\varphi + g\frac{\partial\varphi}{\partial z} = 0 \qquad \text{on } z = 0 \tag{2.11}$$

Thus, the goal of the (linearized) BVP being to find the velocity potential φ, Equations (2.1), (2.2) and (2.10) has to be solved. If there is a body present, then the kinetic boundary condition on the body, Equation (2.2) must also be Taylor-expanded.

2.2 Domain Decomposition

The approach on finding the natural frequency in a two-dimensional moonpool by Molin (2001) is herein presented, with an emphasis on the domain decomposition. Domain decomposition is the concept of dividing a given problem domain into smaller sub-domains, which are independently solved while matched at the boundaries between sub-domains.

Molin decomposes the fluid domain into two sub-domains. A sketch of the fluid domain is provided in Figure 2.2.

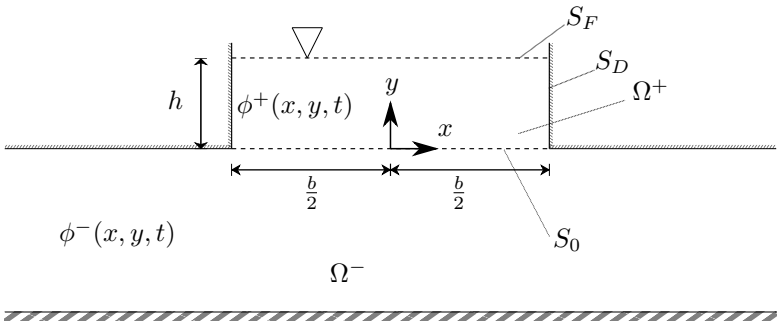

Figure 2.2: Two-dimensional domain decomposition in Molin (2001). The moonpool sub-domain is in $|x| \leq \frac{b}{2}$, $0 \leq y \leq h$, where b is the moonpool width, and the semi-infinite half-plane below the moonpool opening, i.e. on $y \leq 0$. S_0 is the common boundary between the sub-domains on $|x| \leq \frac{b}{2}$, $y = 0$. The upper and lower sub-domain are assigned the velocity potentials $\phi^+(x,y,t)$ and $\phi^-(x,y,t)$, respectively.

The procedure in the domain decomposition is to match the velocity potentials and their normal velocity, i.e. a Neumann boundary condition, on S_0,

$$\phi^+(x,0,t) = \phi^-(x,0,t) \tag{2.12}$$
$$\phi_y^+(x,0,t) = \phi_y^-(x,0,t) \tag{2.13}$$

where $\phi_y^{\pm}(x,0,t) = \frac{\partial}{\partial y}\phi^{\pm}(x,y,t)\Big|_{y=0}$, the vertical velocity on the boundary. The complex velocity potential in the lower sub-domain is then given by

$$f^-(z,t) = -\frac{1}{\pi}\int_{-b/2}^{b/2} \phi_y^-(\zeta,0,t)\ln(z-\zeta)\mathrm{d}\zeta, \tag{2.14}$$

implying a distributed source with source density equal to the vertical velocity on S_0. Equation (2.14) is singular at infinity, as it does not account for any wave radiation, which is physically bound to happen. To compensate for this, Molin placed two sinks a distance $\pm\lambda B/2$, where λ is somewhat larger than 1 and B is the beam of the barge. Equation (2.14) is then rewritten to

$$f^-(z,t) = -\frac{1}{\pi}\int_{-b/2}^{b/2} \phi_y^-(\zeta,0,t)\left[\ln(z-\zeta) - \underbrace{\frac{1}{2}\ln(z-\lambda B/2)}_{\text{sink}} - \underbrace{\frac{1}{2}\ln(z+\lambda B/2)}_{\text{sink}}\right] d\zeta \tag{2.15}$$

By allowing for an error $\mathcal{O}\left(b^2/(\lambda B)^2\right)$, the velocity potential on S_0 becomes

$$\phi^+(x,0,t) = -\frac{1}{\pi}\int_{-b/2}^{b/2} \phi_y^+(\zeta,0,t)\ln\frac{|x-\zeta|}{\lambda B/2}\mathrm{d}\zeta \tag{2.16}$$

by the use of Equations (2.12) and (2.13). By utilizing this, the attention is then turned towards the BVP

$$\nabla^2\varphi = 0 \qquad \text{in } \Omega^+; \tag{2.17a}$$

$$\frac{\partial\varphi}{\partial x} = 0 \qquad \text{in } S_D; \tag{2.17b}$$

$$g\varphi_y - \omega^2\varphi = 0 \qquad \text{on } S_F; \tag{2.17c}$$

$$\varphi^+(x,0) = -\frac{1}{\pi}\int_{S_0} \varphi_y^+(\zeta,0)\ln\frac{|x-\zeta|}{\lambda B/2}\mathrm{d}\zeta \qquad \text{on } S_0; \tag{2.17d}$$

where it is assumed that the solution is oscillating harmonically in time, i.e. $\phi^+(x,y,t) = \mathrm{Re}\{\varphi(x,y)\exp(\mathrm{i}\omega t)\}$. The BVP (2.17) is then solved to give the natural frequency of the piston mode, given by

$$\omega_0 \simeq \sqrt{\frac{g}{h + (b/\pi)\left(\frac{3}{2} + \ln(\lambda B/2b)\right)}} \tag{2.18}$$

The procedure is also repeated to yield the piston and sloshing mode natural frequencies in three dimensions. Molin et al. (2018) extended this work to a barge of finite spatial extension and finite depth. An adaptation of the piston mode and first to third sloshing mode, adapted to this thesis' geometry, is presented in Table 7.2.

2.3 Regular Waves of Constant Steepness

Regular waves in the present thesis are given by wave steepness and period T. The wave steepness is given by the wave height-to-wave length ratio, H/λ. A regular wave is given by

$$\zeta(x,t) = \frac{H}{2}\sin(\omega t - kx) \tag{2.19}$$

where k is the wave number, $\lambda = 2\pi/k$ the wave length and $\omega = 2\pi/T$ the angular frequency. H is the wave height, subject to the wave period and steepness through

$$H = \left(\frac{H}{\lambda}\right)^{*}\lambda = \left(\frac{H}{\lambda}\right)^{*}\frac{2\pi}{k}, \tag{2.20}$$

where $(H/\lambda)^{*}$ denotes the value of the wave steepness, e.g. $(H/\lambda)^{*} = 1/60$ and the wave number k is given by the dispersion relation

$$\frac{\omega^2}{g} = k\tanh(kh), \tag{2.21}$$

assuming finite depth.

2.4 Sloshing Modes

During sloshing, the oscillating free surface will exist in various forms, or *modes*. The different natural modes can be idealised as standing waves in a tank, as presented in Figure 2.3.

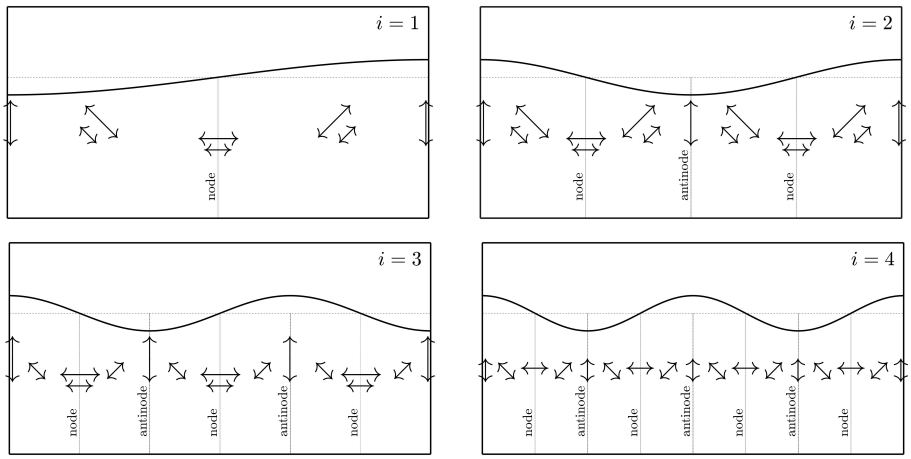

Figure 2.3: Two-dimensional natural sloshing modes in a rectangular tank. Figure inspired by Faltinsen et al. (2009).

A standing wave can be described by nodes and antinodes. A node is the horizontal position of which a fluid particle only has a horizontal motion, and an antinode is the horizontal position of which a fluid particle only has a vertical motion. Further, the sloshing mode can then be odd or even, depending on the symmetry about the center line of the tank.

This can also be extende to three dimensions, as seen in Figure 2.4. Here, the natural sloshing modes i and j are along the x- and y-axis, respectively.

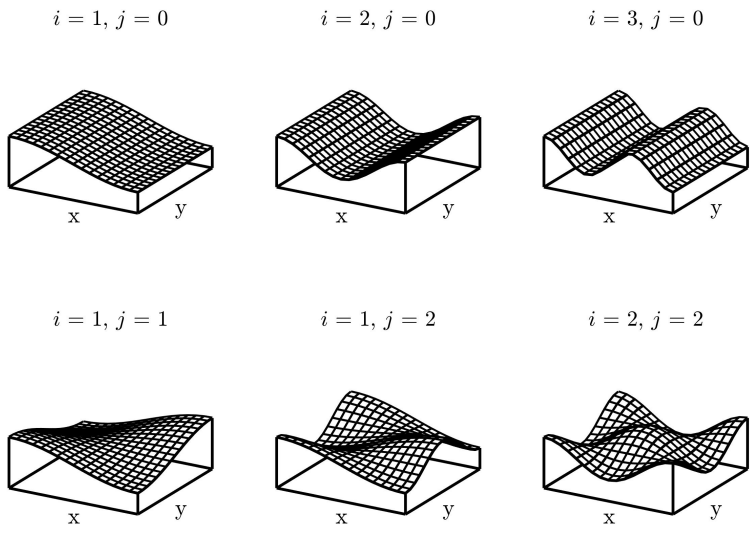

Figure 2.4: Three-dimensional natural sloshing modes.

It is seen that when the product $ij = 0$, the surface elevations will take the form of those in Figure 2.3. These modes are called a *Stokes freestanding wave*.

2.5 Surface Tension

This section presents a theoretical study on the effect of the surface tension on propagating waves, with applicability to this thesis. As the moonpool dimensions (Table C.1) are relatively small, it could be useful to investigate whether some sloshing modes will be affected by the surface tension.

According to Myshkis et al. (1987), the surface tension have a non-neglible effect on the lower natural frequencies when the Bond number,

$$Bo = \frac{gl^2\Delta\rho}{T_s} \tag{2.22}$$

is small. Here, g is the gravitational acceleration, $\Delta\rho$ is the density density difference between the two given states, T_s the surface tension and l the tank breadth for two-dimensional cases and the larger of the tank breadth and tank width for three-dimensional cases. According to Faltinsen et al. (2009), a representative value for the air-water interface is $T_s = 0.073$ Nm^{-1}. Values of Bo for the current moonpool configurations are provided in Table 2.1.

Table 2.1: Bond number for the different moonpool configurations, cf. Table C.1. For M2 and M3, Bo is given for a single moonpool.

Configuration	$l \times b$	Bo
M1	0.50 m $\times$ 0.10 m	33595.9
M2,M3	0.10 m $\times$ 0.10 m	1343.8

There is no defined lower bound for when the Bond number affects the sloshing mode, but an approach could be to look at when the surface tension is non-neglible for two-dimensional propagating waves. It can be shown, see Appendix A.1.1, that the surface tension can be neglected for wave lengths larger than $\sim$0.05 m.

As an example, consider an arbitrary two-dimensional sloshing tank and the first sloshing mode, which is a standing wave with a wave length twice the width of the tank. Now, for the surface tension to have an effect, the width of the tank needs to be ≤ 0.025 m, which corresponds to a Bond number of 84.

Table 2.1 corresponds to the second sloshing mode, as this is a standing wave where it's length is equal to the width of the tank. Thus, according to the reasoned lower bound of $Bo = 84$, the surface tension does not affect the second sloshing mode for the current moonpool configuration.

Developing the idea further, by looking at the implied wave lengths for various sloshing modes in the present moonpool configurations, we can investigate whether the theoretical wave lengths become sufficiently small so that the surface tension can't be neglected, as per the reasoned lower bound. Table 2.2 present the theoretical sloshing mode wave lengths as a function of the sloshing mode and moonpool configuration.

Table 2.2: Theoretical wave lengths λ for natural sloshing modes n for the different moonpool configurations. For M2 and M3, results are given for a single moonpool.

Mode	0	1	2	3	4
M1	-	1.0 m	0.5 m	0.333 m	0.25 m
M2/M3	-	0.2 m	0.1 m	0.067 m	0.05 m

In Table 2.2, mode 0 corresponds to the piston mode, which by definition doesn't have a wave length. The wave length is equal to 0.05 m in M2/M3 for mode 4. The conclusion is then drawn that the surface effect overall can be neglected, as it is not expected that mode 4 is the dominant mode, or will be apparent at all, see Ravinthrakumar et al. (2020, MP2 results).

Chapter 3

Analytical Model

This chapter describes the developed analytical model to obtain the piston mode natural periods of the two- and three-moonpool configuration in this thesis. The model is inspired by Molin (2001) and, in particular, Miles (2002).

Reiersen et al. (2018, in review) determined the two-dimensional piston mode periods for a two-moonpool configuration analogously with Molin (2001) by adding two sinks outside the hull. They investigated their locations by comparing with experimental results. The representation in terms of the lower fluid domain and matching of potentials are also done in a simpler manner than what is presented in the developed analytical model.

The motivation behind the analytical model is to obtain the natural periods of the piston modes arising from the heave and pitch motion. For example, for a two-moonpool configuration, there will be one symmetric mode, connected to the heave motion, and one anti-symmetric mode, connected to the pitch motion.

3.1 Assumptions and Limitations

The developed model is analogous with the one in Molin (2001), in the meaning that the water depth is assumed infinite, and the barge is infinitely large, i.e. the moonpools are not interacting with outer fluid domain. Linear potential flow is assumed. Only the lowest order representation is considered, i.e. only vertical fluid motion in the moonpool. Harmonic motion is assumed, which means that relative phases of the moonpools can be determined from the sign of the vertical velocity w in the moonpool.

3.2 Problem Definition

The overview of the problem for M2, the two-moonpool configuration, is presented in Figures 3.1 and 3.2.

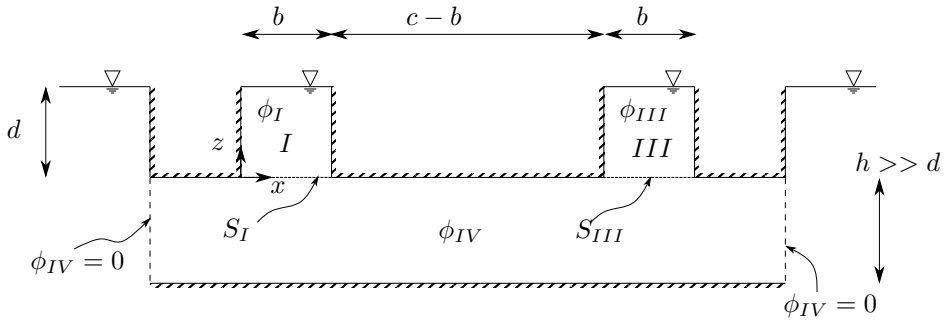

Figure 3.1: Transverse view of the M2 problem. The two moonpools I and III, of width b and spaced apart by c, are described by velocity potentials φ_I and φ_{III} and corresponding boundaries S_I and S_{III}. The semi-infinite lower fluid domain is described by φ_{IV}. $\varphi_{IV} = 0$ at the boundaries implies the spatial extent of the barge, of draft d, to be infinite in the x-direction. $h >> d$ denotes infinite depth.

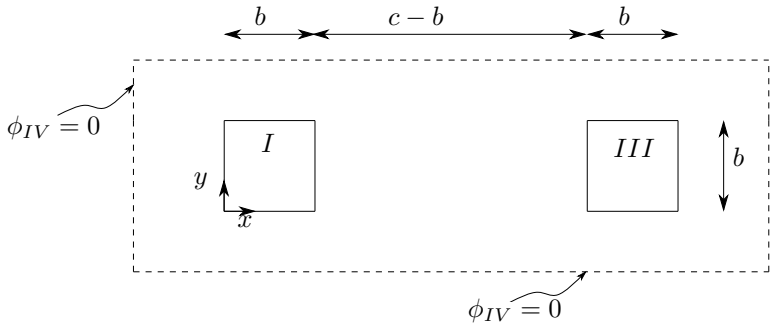

Figure 3.2: Bird's eye view of the M2 problem. The two square moonpools I and III of width b is spaced apart a distance of c. $\varphi_{IV} = 0$ at the boundaries implies the spatial extent of the barge to be infinite.

Unlike Section 2.2, we now have two moonpools, and the description of φ_{IV} is not only described by the source-like behaviour of the two moonpools. The effect of moonpool III on moonpool I, and vice versa, is intrusively incorporated in the model. This is herein referred to as cross-moonpool couplings.

3.3 The Boundary Value Problem

As the piston mode is the only assumed mode, i.e. only vertical fluid motion, the boundary value problem in moonpool I can be written as

$$\nabla^2\varphi_I = 0 \qquad \text{in } I; \tag{3.1a}$$

$$\frac{\partial\varphi_I}{\partial z} = w_1 \qquad \text{on } z = 0; \tag{3.1b}$$

$$g\varphi_z - \omega^2\varphi_I = 0 \qquad \text{on } z = d; \tag{3.1c}$$

where w_1 is the vertical fluid velocity in moonpool I, harmonically oscillating with frequency ω. Exploiting the fact that the Laplace equation, Equation (3.1a), is linear and homogeneous, it's solution is the sum of the solutions on both boundaries, i.e.

$$\varphi_I = \varphi_I|_{z=d} + \varphi_I|_{z=0} \tag{3.2}$$

On $z = d$, the combination of Equations (3.1b) and (3.1c) gives

$$\varphi_I|_{z=d} = \frac{g}{\omega^2}w_1 \tag{3.3}$$

On $z = 0$, we solve wrt. the Laplace equation,

$$\begin{aligned} \nabla^2\varphi_I|_{z=0} = 0 \qquad \Rightarrow \qquad \varphi_I|_{z=0} &= Az + B \\ &= w_1 z - w_1 d \end{aligned} \tag{3.4}$$

where Equation (3.1b) is applied to find A, and B is found by demanding the boundary condition (3.1c) on Equation (3.2). The solution of the BVP, Equation (3.1), is thus given by

$$\varphi_I = w_1\left(z - d + \frac{g}{\omega^2}\right), \qquad 0 \le z \le d \tag{3.5}$$

Now, for φ_{IV}, due to the cross-moonpool couplings, we can write

$$\varphi_{IV} = \varphi_{IV,I} + \varphi_{IV,III}, \tag{3.6}$$

that is, the velocity potential in the lower fluid domain is the sum of the velocity potentials originating from moonpools I and III. Remembering that a three-dimensional source can be written as $1/R$, where the radial distance from the point $(x, y, z) = (\theta, \tau, \gamma)$ is $R = \sqrt{(x-\theta)^2 + (y-\tau)^2 + (z-\gamma)^2}$, we can write

$$\begin{aligned} \varphi_{IV,I}(x, y, z = 0) = &\frac{w_1}{2\pi}\iint_{S_I} \frac{1}{\sqrt{(x-\zeta)^2 + (y-\eta)^2}}\mathrm{d}\zeta\mathrm{d}\eta, \qquad \begin{cases} 0 \le \zeta \le b \\ 0 \le \eta \le b \end{cases} \\ &+\frac{w_2}{2\pi}\iint_{S_{III}} \frac{1}{\sqrt{(x-\theta)^2 + (y-\tau)^2}}\mathrm{d}\theta\mathrm{d}\tau, \qquad \begin{cases} c \le \theta \le c + b \\ 0 \le \tau \le b \end{cases} \end{aligned} \tag{3.7}$$

which shows the cross-moonpool coupling through the velocities w_1 and w_2. The opposite also holds for $\varphi_{IV,III}$.

3.4 General Solution

The procedure shown in Equation (3.7) can be generalized to N moonpools, given by

$$\varphi_{IV}(\boldsymbol{r}) = \sum_{n=1}^{N} \frac{w_n}{2\pi} \iint_{S_n} \frac{\mathrm{d}S\left(\boldsymbol{\rho}_n\right)}{|\boldsymbol{r} - \boldsymbol{\rho}_n|}, \qquad z < 0, \tag{3.8}$$

where $\boldsymbol{\rho}_n$ is the spatial coordinates of moonpool n with vertical velocity w_n in relation to the spatial coordinate system $\boldsymbol{r}$. Now, as the Neumann condition is implied in Equation (3.8) (through w_n), we only need to match φ_{IV} to the N moonpool openings. It can be shown (Miles, 2002) that

$$\sum_{n=1}^{N} \left[\delta_{mn} \left(d - \frac{g}{\omega_{0,n}^2} \right) + A_{mn} \right] b_n w_n = 0, \qquad (m = 1, \ldots, N) \tag{3.9}$$

where

$$A_{mn} \equiv \frac{1}{2\pi b_n^2 b_m^2} \iint \mathrm{d}S\left(\boldsymbol{r}_n\right) \iint \frac{\mathrm{d}S\left(\boldsymbol{\rho}_n\right)}{|\boldsymbol{r} - \boldsymbol{\rho}_n|} = A_{nm} \tag{3.10}$$

δ_{mn} is the Kronecker delta and b_n and b_m is the width of moonpool n and m, respectively. The function of the Kronecker delta is to keep track if one is subject to a cross-moonpool coupling ($m \neq n$) or not ($m = n$).

The non-cross-moonpool terms, which is the integration of the idealized moonpool source over it's domain, is given in Molin (2001) and can be found in Appendix B.1.1, Equation (B.1.5).

The cross-moonpool coupling terms is, by e.g. Miles (2002), Newman (2003) or Vries et al. (2014), all working with circular moonpools, estimated to

$$B = \frac{a^2}{c} = \frac{b^2}{2\pi c} \tag{3.11}$$

where a is the moonpool radius, $b = \sqrt{\pi a^2}$ as the equivalent square moonpool width and c the distance between two moonpools, which should be applicable to moderate moonpool aspect ratios, as recommended by Prof. Bernard Molin in private communications.

3.5 Two Moonpool Configuration

Here, we apply the geometry in Figures 3.1 and 3.2. Two moonpools will, assuming waves propagating along the x-axis in, have two natural piston mode frequencies. The first is connected to the heave motion of the barge, where the moonpool free-surfaces will oscillate in-phase with each other. The second is connected to the pitch motion of the barge, where the moonpool responses are expected to be 180 degrees out-of-phase with each other, intuitively "pushing" and "pulling" on (partly) the same fluid.

Now, Equation (3.9) gives us the two equations

$$\left(d - \frac{g}{\omega_{0,1}^2} + A\right) w_1 + B_{12} w_2 = 0 \tag{3.12}$$

$$B_{21} w_1 + \left(d - \frac{g}{\omega_{0,2}^2} + A\right) w_2 = 0 \tag{3.13}$$

where $A_{11} = A_{22} \equiv A = \frac{1}{2\pi b^3} I_{0000}$ and $B_{12} = B_{21} \equiv B$. I_{0000} is given in Appendix B.1.1, and B is as given in Equation (3.11). Equations (3.12) and (3.13) can be written on matrix form,

$$\begin{bmatrix} \theta & B \\ B & \theta \end{bmatrix} \boldsymbol{w_n} = 0, \qquad \theta \equiv \left(d - \frac{g}{\omega_{0,n}^2} + A\right), \tag{3.14}$$

where $n = 1, 2$ and $\boldsymbol{w_n} = [w_1, w_2]^T$. Non-trivial solutions to Equation (3.14) is given when the determinant of the matrix,

$$\det \begin{bmatrix} \theta & B \\ B & \theta \end{bmatrix} = \left(\theta^2 - B^2\right) \tag{3.15}$$

is equal to zero. Equation (3.15) has the roots $\boldsymbol{\lambda} = \{-B, B\}$ and we are able to solve for the natural frequency $\omega_{0,n}$ from

$$\begin{aligned} \theta &= \lambda_i \\ \Rightarrow d - \frac{g}{\omega_{0,n}^2} + A &= \lambda_i \\ \Rightarrow \omega_{0,n} &= \sqrt{\frac{g}{h + A - \lambda_i}}, \qquad i = n = 1, 2 \end{aligned} \tag{3.16}$$

Thus, the two solutions are obtained from

$$\omega_{0,1} = \sqrt{\frac{g}{h + A + B}} \tag{3.17}$$

$$\omega_{0,2} = \sqrt{\frac{g}{h + A - B}} \tag{3.18}$$

The phases connected to the heave and pitch motion is formally shown by introducing the two solutions $\theta = \pm B$ back into Equation (3.14).

For $\theta = \lambda_2 = -B$, Equation (3.17), this yields

$$\begin{bmatrix} B & B \\ B & B \end{bmatrix} \begin{bmatrix} w_1 \\ w_2 \end{bmatrix} = 0 \quad \Rightarrow \quad w_1 = w_2 \tag{3.19}$$

and for $\theta = \lambda_1 = B$, Equation (3.18), we get

$$\begin{bmatrix} -B & B \\ B & -B \end{bmatrix} \begin{bmatrix} w_1 \\ w_2 \end{bmatrix} = 0 \quad \Rightarrow \quad w_1 = -w_2 \tag{3.20}$$

This shows, that the moonpool modes are in phase at the mode arising from the heave motion of the barge, and 180 degrees out-of-phase at the mode arising from the pitch motion of the barge.

3.6 Three Moonpool Configuration

Extending the idea in the previous section to three moonpools, each spaced apart the distance $c/2$ in a linear array, we can assume that the cross-moonpool coupling is in terms of their relative position to each other, which is

$$A_{mn} \equiv B_{|m-n|} \qquad (m \neq n) \tag{3.21}$$

$A_{nn} = A$ is as previously defined, and Equation (3.9) is then, as shown by Miles (2002), re-written to

$$\sum_{n=1}^{N} \left[\delta_{mn} \left(d + A - \frac{g}{\omega_{0,n}^2} \right) + (1 - \delta_{mn}) B_{|m-n|} \right] w_n = 0, \tag{3.22}$$

which with $N = 3$ reduces to the matrix equation

$$\begin{bmatrix} \theta & B_1 & B_2 \\ B_1 & \theta & B1 \\ B_2 & B_1 & \theta \end{bmatrix} \boldsymbol{w_n} = 0, \qquad \theta \equiv \left(d - \frac{g}{\omega_{0,n}^2} + A \right), \tag{3.23}$$

where $n = 1, 2, 3$ and $\boldsymbol{w_n} = [w_1, w_2, w_3]^T$. The procedure is similar, but more tedious than in Section 3.5, and can be found in Appendix B.1.2. Equation (3.23) yields three solutions, given by

$$\omega_{0,n} = \sqrt{\frac{g}{h + A - \lambda_i}}, \qquad i = n = 1, 2, 3 \tag{3.24}$$

where λ_i is shown in Appendix B.1.2, Equation (B.1.12). Thus, three modes are apparent, which in terms of the moonpool vertical velocities, connected to the roots $\boldsymbol{\lambda}$, are

$$\lambda_1 : \qquad \boldsymbol{w} = \begin{bmatrix} -w_k \\ 0 \\ w_k \end{bmatrix}$$

$$\lambda_2 : \qquad \boldsymbol{w} = \begin{bmatrix} -w_j \\ w_k \\ -w_j \end{bmatrix}$$

$$\lambda_3 : \qquad \boldsymbol{w} = \begin{bmatrix} w_l \\ w_k \\ w_l \end{bmatrix}$$

where the subscripts j, k, l represents similar velocity for a given mode, and the sign represents the relative direction, i.e. phase, in the same mode.

Thus, $\omega_{0,1}$ is connected to the pitch motion with the middle moonpool "at rest". Interestingly, $\omega_{0,2}$ predicts the outer moonpools of similar velocity and 180 degrees out-of-phase with the middle one. Both $\omega_{0,2}$ and $\omega_{0,3}$ arises from the heave motion, and the latter one represents the intuitive mode where all three moonpools are in phase.

3.7 Results

To verify the analytical model, simulations are conducted in WAMIT. See Chapter 4 for a overview of the use of WAMIT in this thesis.

The geometry $b = 0.10$ m, $c = 0.40$ m and $d = 0.05$ m are applied, similar to the experimental setup (Table C.1). The outer moonpools are situated $c/2$ from the origin of the global coordinate system. The inclusion of the middle moonpool, centred at the origin, facilitates the three-moonpool configuration. Similar to the analytical model, the simulations assumes infinite water depth.

Three numerical wave probes, one in the centre of each moonpool, are placed in order to measure the free-surface elevation. To minimize the coupling of the moonpool free-surface response with the outer fluid domain, the barge is extended to a length and width of 1 m, Figure 3.3. WAMIT was not able to run simulations on a larger barge, as error messages indicated WAMIT not being able to carry out the analytical Rankine integrals. Large, local values of the potential due to the small moonpool diameter-to-barge width ratio is expected to be the reason.

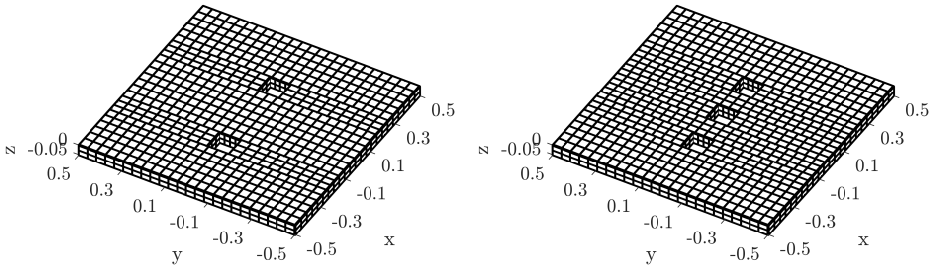

(a) M2 **(b)** M3

Figure 3.3: Mesh for the analytical model. The figures present a course mesh ($N \approx 700$), while the mesh size used is $N = 2858$ for M2 and $N = 2871$ for M3, N being the number of panels over the half-body. Waves are propagating along the negative x-axis.

As WAMIT separately solves the velocity potential for each rigid body mode, we can look at the heave and pitch modes separately. For each mode $i = 1, 2, \cdots, 6$, WAMIT outputs the real, $\Re_i$, and imaginary part, $\Im_i$, of the free-surface elevation RAO, $\bar{\zeta_{i,p}}$ at the probe p at each incident wave period. The absolute value and the phase are then calculated through $|\bar{\zeta_{i,p}}| = \sqrt{\Re_i^2 + \Im_i^2}$ and $\varepsilon_{i,p} = \arctan(\Im_i / \Re_i)$, respectively.

3.7.1 Two Moonpools

The free-surface RAO for the two-moonpool case at wave probes 1 and 3 are presented in Figure 3.4 for both the forced heave and pitch motion. The results from the analytical method applied on the two-moonpool configuration and from WAMIT are provided in Table 3.1.

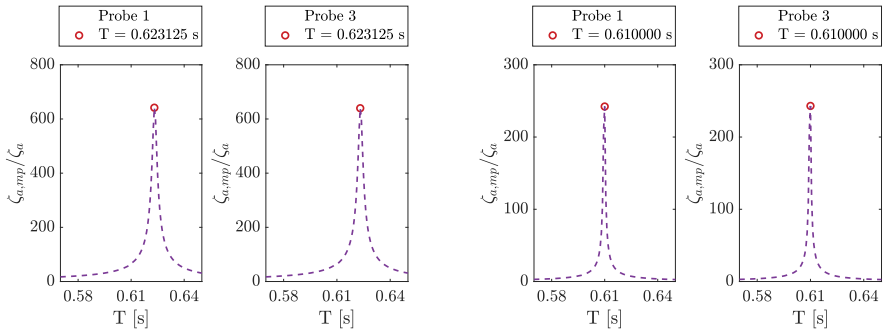

(a) Forced heave **(b)** Forced pitch

Figure 3.4: WAMIT results for the analytical two-moonpool configuration. Numerical wave probe 1 is placed at $(x, y, z) = (0.2, 0, 0)$ and probe 3 at $(x, y, z) = (-0.2, 0, 0)$, cf. Figure 3.3. The vertical axes shows body-fixed RAOs at the numerical wave probes, while the horizontal axes shows the period of oscillation.

Table 3.1: Comparison of the analytical two-moonpool model to WAMIT. The phase angles ε_p for the probes $p = 1, 3$ are relative to the phase of an incident wave in the origin of the coordinate system, cf. Figure 3.3.

Analytical model	WAMIT			
Period [s]	Period [s]	ε_1 [deg]	ε_3 [deg]	Mode
$T = 0.612889$	$T = 0.610000$	118.3328	-61.6661	Pitch
$T = 0.638481$	$T = 0.623125$	-102.0471	-102.0292	Heave

As seen in Figure 3.4, the free-surface RAOs shows one unique piston mode period, both in forced heave and pitch. There is a fair agreement between our analytical model and WAMIT; the analytically predicted piston mode period due to forced heave, Table 3.1, is 2.47% higher compared to the period predicted by WAMIT, while the analytical predicted pitch period is 0.47% higher. The value of the RAOs, seemingly equal in each mode, indicates that the moonpool elevation in each moonpool are the same. This agrees with Equations (3.19) and (3.20); that the moonpool velocities are of equal magnitude in each mode.

The relative phase angles between the moonpools, Table 3.1, are virtually 0 and 180 degrees in/out-of-phase for the heave and pitch motion, respectively. Strictly,with a precision of four decimals, they are 0.0179 and 179.9989 degrees for the heave and pitch, respectively. The reason could be coupling with the outer fluid domain, as the results seem sensitive to the barge size, or numerical errors. As seen in Appendix B.1.3, WAMIT simulations with the width of the barge equal to 0.5 m, i.e. half of what herein is presented, the natural piston mode periods differ compared to the WAMIT results in Table 3.1, being 1.2% and 0.4% lower in heave and pitch, respectively

If one is to increase c, the spacing of the moonpools, while keeping b constant, the

cross-moonpool couplings are expected to decay, and the moonpools will then act as single moonpools, each with a piston mode period agreeing with Molin (2001). The result of applying this to the analytical model can be seen in Figure 3.5, which shows that this is in fact the case.

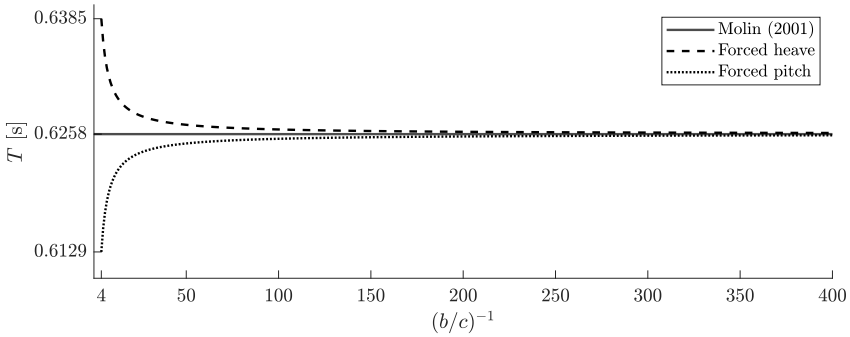

Figure 3.5: Comparison of the analytical two-moonpool model to Molin (2001). Keeping b constant and increasing c, each moonpool are approaching the natural period from Molin (2001) of $T = 0.6258$ s, both in forced heave and pitch. The current geometry are given by $b/c = 0.25$, or, according to the figure, $(b/c)^{-1} = 4$.

3.7.2 Three Moonpools

The free-surface RAO at wave probes 1, 2 and 3 are presented in Figure 3.6 for both the forced heave and pitch motion. The results from the analytical method applied on the two-moonpool configuration and from WAMIT are provided in Table 3.2.

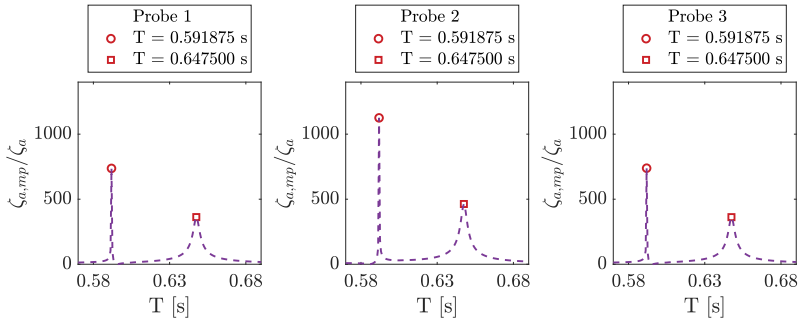

(a) Forced heave

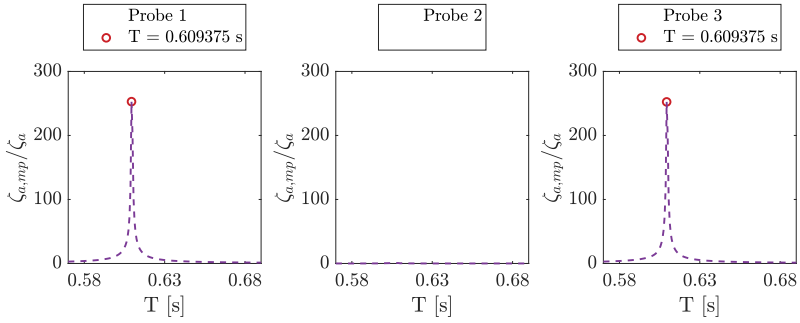

(b) Forced pitch

Figure 3.6: WAMIT results for the analytical three-moonpool configuration. Numerical wave probe 1 is placed at $(x, y, z) = (0.2, 0, 0)$, probe 2 at $(x, y, z) = (0, 0, 0)$ and probe 3 at $(x, y, z) = (-0.2, 0, 0)$, cf. Figure 3.3. The vertical axes shows body-fixed RAOs at the numerical wave probes, while the horizontal axes shows the period of oscillation.

Table 3.2: Comparison of the analytical two-moonpool model to WAMIT. The phase angles ε_p for the probes $p = 1, 2, 3$ are relative to the phase of an incident wave in the origin of the coordinate system, cf. Figure 3.3.

Analytical model	WAMIT				
Period [s]	Period [s]	ε_1 [deg]	ε_2 [deg]	ε_3 [deg]	Mode
$T = 0.594693$	$T = 0.591875$	-137.3617	43.4711	-137.3627	Heave
$T = 0.612889$	$T = 0.609375$	54.5122	-	-125.4908	Pitch
$T = 0.667565$	$T = 0.647500$	-98.9259	-98.6331	-98.9191	Heave

As seen in Figure 3.6, the free-surface RAOs show two unique piston mode periods for forced heave, and one unique period for forced pitch. The analytically predicted heave periods, Table 3.2, are 0.49% and 3.10% (lower and higher period, respectively) higher compared to the period predicted by WAMIT, while the analytically predicted pitch period is 0.58% higher. Given the approximations in our model, we consider this to serve as a first verification.

Agreeing with Section 3.6, Table 3.2 shows two unique heave mode natural periods; one where the two outer moonpools are 180 degrees out-of-phase with the middle moonpool and one where all three moonpools are in-phase. The deviation from "perfectly" 0 -and 180-degrees in/out-of-phase is in order similar as for the two-moonpool simulation, and again it is believed to originate form the finite spatial extension of the barge, or numerical errors.

The value of the RAOs, seemingly not equal for the three moonpools in forced heave, agrees with the result in Appendix B.1.2; that the middle moonpool has a larger velocity than the two outer ones. The physical meaning of this is that, all three moonpools harmonically oscillating with the same frequency ω_0, the middle moonpool will have a larger free-surface displacement. The pitch mode piston natural period is analogous with the two-moonpool configuration, with the middle moonpool at rest.

Similar to the two-moonpool configuration, increasing c while keeping b constant, all piston mode periods are expected to agree with Molin (2001), which, as seen in Figure 3.7, is the case.

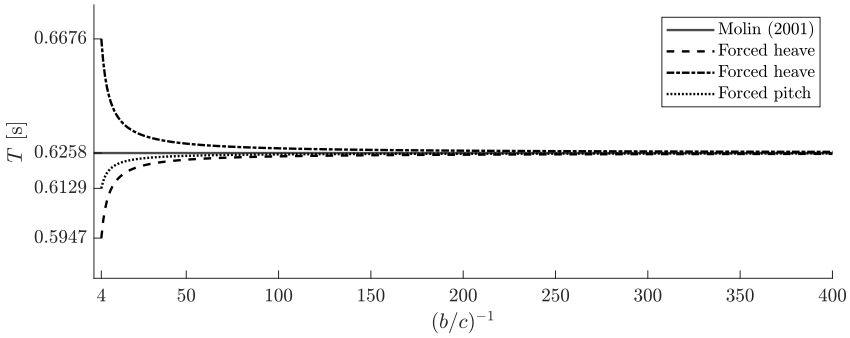

Figure 3.7: Comparison of the analytical three-moonpool model to (Molin, 2001). Keeping b constant and increasing c, each moonpool are approaching the natural period from Molin (2001) of $T = 0.6258$ s, both in forced heave and pitch. The current geometry are given by $b/c = 0.25$, or, according to the figure, $(b/c)^{-1} = 4$.

Chapter 4

Numerical Simulations

This chapter covers the use of the linear potential flow theory solver WAMIT. One of the objectives was to carry out numerical replications of the experiments, which, if carried out successfully, would coincide with the experimental results.

WAMIT, specifially version 6.4, is also used in the analytical and parametric studies, and this chapter will work as a background for these.

In addition the the three moonpool configurations, cf. Table C.1, a fourth geometry is included, denoted M0. This is a vessel of similar main properties, but with no moonpools. M0 acts as a tool for comparing vessel responses with and without moonpol(s), to further study the effect of moonpools on the vessel response.

First, a brief overview of WAMIT and important particulars of WAMIT in relation to this thesis is given. Then, an overview of the solution procedure is provided, before some limitations on the use of WAMIT is briefly discussed. Lastly, input geometry and results from the mesh sensitivity study is presented.

4.1 Overview of WAMIT

WAMIT is a linear potential flow theory solver (see Section 2.1 for an outline of potential flow theory), solving the radiation and diffraction problem, along with the rigid body motions. WAMIT makes use of the Boundary Element Method (BEM). A fundamental assumption is that the solution is harmonically dependent, which facilitates the use of Green's second identity; transforming volume integrals to surface integrals. Thus, one only need to solve for the given boundary conditions. Further, free-surface Green functions take care of the free-surface boundary condition, and only the body boundary condition and domain boundary conditions (vertical domain boundaries and seabed) is to be considered. Hence, the only discretisation demanded by the user is the discretisation of the body boundary in terms of panels.

4.1.1 WAMIT Particulars in this Thesis

WAMIT, developed as a linear potential flow solver, also provides a higher-order method, where the body panels can be represented using other techniques than just flat panels. The velocity potential on the body is represented by a continuous B-spline, rather than approximating the velocity potential constant over each panel. In the numerical simulations carried out, the lowest-order method is used.

Version 6.4 only facilitates the inclusion of a single vertical wall, while in version 7.2, two vertical walls can be present, which could be used to further replicate the experiments in this thesis. All simulations in this thesis are done in open-sea conditions.

WAMIT also have the option to include external damping. This is most commonly done in roll, for example by using the work of Ikeda et al. (1993), as WAMIT often will over-predict roll motion (and further influence the sway motion). As the present study is concerned with a vessel in head-sea, no external damping is provided.

As a consequence of the solution procedure using Green functions, an infinitely number of non-physical resonant modes can be excited, solely coming from a mathematical point-of-view. To remove these irregular frequencies, WAMIT provides the possibility to mesh the interior (dry) surface of the body (Lee et al., 2006). Hence, all simulations are run with an interior "free-surface" to remove these frequencies.

4.1.2 Solution Procedure

A brief overview of the solution procedure is provided in the following.

1. The mesh is input, and symmetry planes is exploited, facilitating faster CPU time.
2. Based on the input COG, stiffness coefficients are calculated. The input inertia matrix is also input along with the geometry, fundamental for the roll, pitch and yaw responses. External system stiffness, e.g. from mooring lines, are also input, along with the mass matrix. Any external damping is also input here.
3. WAMIT then solves for the radiation potentials for specified modes, analogous with forced motion of the geometry.
4. The diffraction potentials are then solved to get the wave excitation loads.
5. WAMIT then used the result from 3) and 4), to compute the rigid body motion RAOs. Specified field point values (pressure on the body, fluid velocity or free-surface elevation) are also output.

4.2 Limitations on Linear Potential Flow Solvers

In the use of any numerical method approximating the "real world", one need to be aware of and cautious with the given method's limitations.

Concerning linear potential flow theory solvers, the assumption of inviscid flow is the limitation often of biggest concern. Applied to the present case, with a moonpool vessel, flow will separate and vortices will be shed at sharp corners, for example in the

moonpool opening or at the bilge keels in roll motion (thus often the need to include external damping). Potential flow theory are not capable of capturing these phenomena. As vortices will act as damping on the vessel, physically by transferring energy away from the system, responses may be over-predicted in proximity of resonance.

Analogously, radiated waves, captured by the radiation velocity potentials, will remove energy from the system, and thus act as a damping mechanism. As WAMIT captures this, we can compare experimental results and numerical simulations to get an idea of the effect of, in our case flow separation, of various responses. This can be done as flow separation and wave radiation are the two main contributors to the damping of the vessel.

Another worth-to-mention limitation of linear potential flow theory is that the free-surface is linearized, and higher-order free-surface elevation, for instance secondary resonance in the moonpools, are not captured.

4.3 Mesh and Mesh Convergence Study

Prior to carrying out the simulations, a mesh sensitivity analysis needed to be conducted. The input meshed geometry, based on a developed code in Ravinthrakumar et al. (2020) and further developed in the present work, is presented in Figure 4.1.

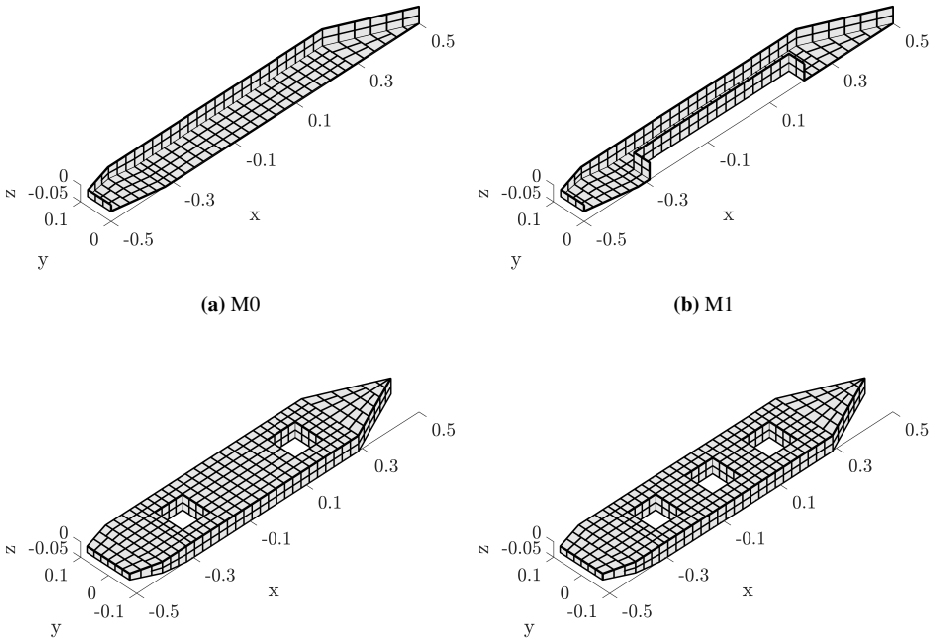

(a) M0 **(b)** M1

(c) M2 **(d)** M3

Figure 4.1: Example of mesh for M0, M1, M2 and M3. The mesh of M0 and M1 present no interior free-surface and the symmetry plane at $y = 0$, which is exploited to run the simulations only on the half-body. The presented mesh, for clarity quite coarse, have $N \sim 300$, N being the number of panels over the half-body.

The mesh sensitivity study was carried out by investigating the moonpool, heave and pitch responses for a selection of wave periods, cf. Section 5.2.1. Results showed large sensitivity in the proximity of resonance, as is expected. Satisfactory convergence is achieved at $N \geq 250$, where N is the number of panels over the half-body. The present simulations are run with $N \sim 1100$ panels over the half-body. Results for the mesh sensitivity study for M1 and M3 are presented in Figure 4.2.

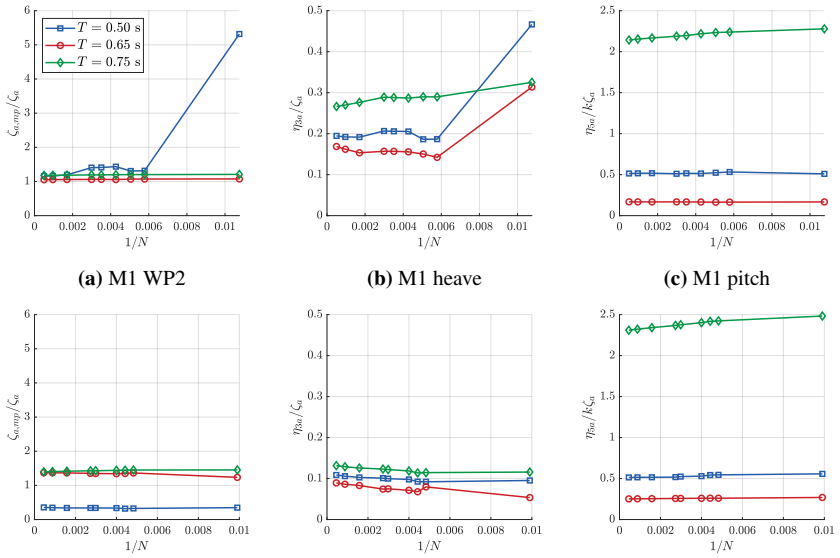

(a) M1 WP2 **(b)** M1 heave **(c)** M1 pitch

(d) M3 WP2 **(e)** M3 heave **(f)** M3 pitch

Figure 4.2: Mesh sensitivity analysis of moonpool, heave and pitch responses for M1 and M3 for selected wave periods. Satisfactory convergence is achieved for $N \geq 250$. Numerical wave probe WP2 is used, analogous with experimental wave probe WP2, cf. Figure C.1.

4.4 Coordinate System

For the free-surface elevation at numerical wave probes, WAMIT outputs this in an Earth-fixed coordinate system. In order to directly compare this with experimental body-fixed results, we need to convert the WAMIT result to a body-fixed coordinate system. A pragmatic way of doing this, given a numerical wave probe situated at (x, y), cf. Figure C.1, is to create time series of the local heave motion and wave probe free-surface elevation,

$$s_3 = |H_3(\omega)| \sin(\omega_i t + \varepsilon_3) - x|H_5(\omega)| \sin(\omega_i t + \varepsilon_5) \tag{4.1}$$

$$\zeta_{WP,EP} = |H_{WP}(\omega)| \sin(\omega_i t + \varepsilon_{WP,EF}) \tag{4.2}$$

where $|H_j(\omega)|$ and ε_j respectively is the RAO and phase angle (relative to the phase of an incident wave in $(x, y) = (0, 0)$), for the response j at wave period $T_i = 2\pi/\omega_i$. The subscripts WP and EF denote wave probe and Earth-fixed, respectively. The time series t should be covering at least one wave period T_i. The body-fixed RAO is then found from

$$|H_{WP,BF}(\omega)| = \max\left(s_3 - \zeta_{WP,EP}\right) \tag{4.3}$$

due to the orientation of the coordinate system.

Chapter 5

Experiments

This chapter describes the model tests and post-processing carried out in relation to this thesis. The experimental setup is provided and possible error sources are further discussed, before preparation of the experiments and the post-processing is presented.

The model tests were carried out in January and February 2020 at the experimental laboratory Lilletanken (Small Towing Tank) at NTNU, with the aim to obtain vessel and moonpool responses for the different geometries. The vessel geometry is based on the one in Ravinthrakumar et al. (2020) and Ravinthrakumar (2020), where one of the moonpool configurations also is based upon. The remaining two are developed for this thesis. The different moonpool configurations are obtained by adding or removing boxes in the moonpool section of the model. A photo of M3 is presented in Figure 5.2. The experimental water depth was 0.8 m, and constant-steepness waves are generated by a piston-mode wavemaker, between the periods 0.4 s to 1.0 s.

5.1 Experimental Setup

The model has a length of 1 m, and a scale of 1:138 is imagined, cf. Ravinthrakumar et al. (2020) and Ravinthrakumar (2020). The three different moonpool configurations are named M1, M2 and M3, as seen in the principal model layout, Figure 5.1. Main properties can be found in Table C.1.

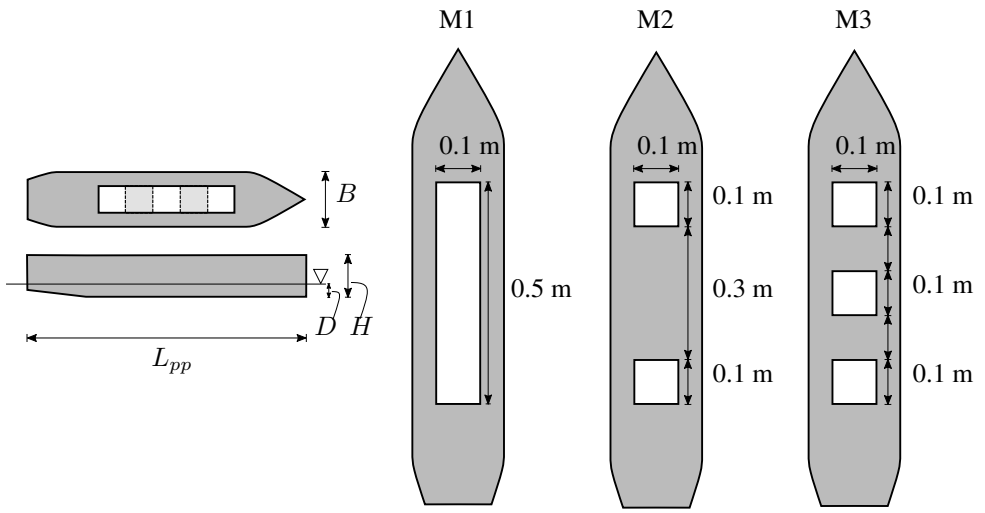

Figure 5.1: Principal model layout. The main dimensions are $L_{pp} = 1$ m, $B = 0.20$ m, $D = 0.05$ m and $H = 0.15$ m.

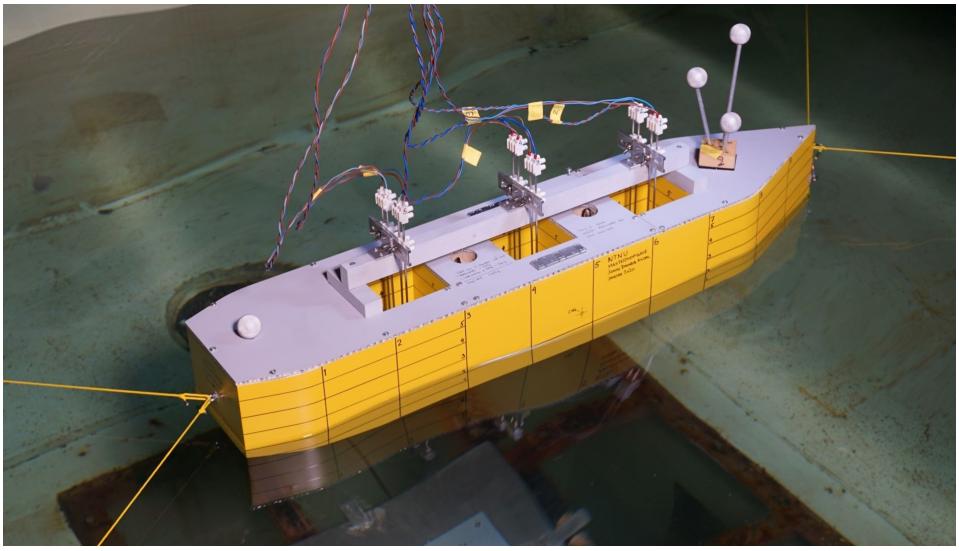

Figure 5.2: M3 model. The model is equipped with six body-fixed wave probes, two in each moonpool, and four marker spheres in order to measure six degree-of-freedom motions using the Oqus software. The model is moored with four horizontal mooring lines. The distance between the horizontal markings on the hull is 0.025 m. Weights are placed in the removable boxes between moonpools to obtain the specified deplacement.

5.1.1 Instrumentation

A sketch of the experimental setup can be seen in Figure 5.3.

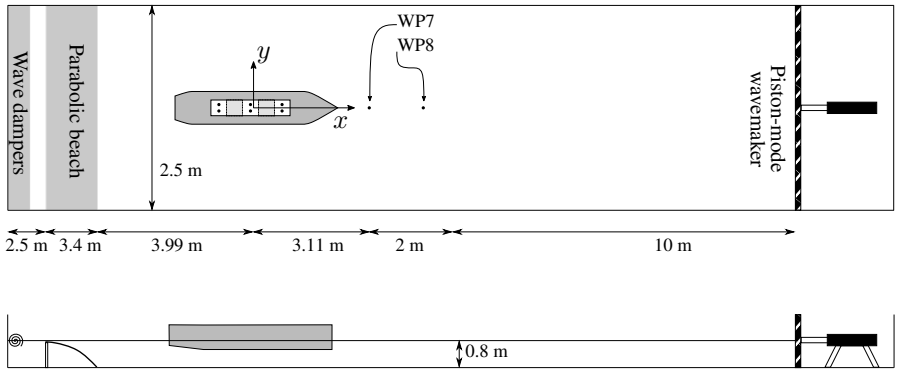

Figure 5.3: Sketch of the experimental setup. The mooring lines are not shown. All measurements are relative to COG of the model, cf. Table C.1. Two wave probes were installed in front of the vessel, denoted WP7 and WP8. The six body-fixed wave probes, WP1-WP6, are placed and numbered in increasing order from starboard to port and from fore to aft. The slotted parabolic beach is positioned a couple of cm below the free surface, suggested by prof. Trygve Kristiansen, as tests have shown good wave removal capabilities compared to having it flush with the free surface, or rising above it. The wave dampers are provisionally made up of chicken wire.

Wave probes

Six body-fixed wave probes, WP1-WP6, whose layout is given in Figure C.1, as well as two movable wave probes, WP7 and WP8, are used. WP7 and WP8 are used to calibrate the wavemaker (described below) as well as to measure the incident waves in each test.

The wave probes was calibrated each day, to ensure correct readings. The wave probe will give a linear relation between the surface elevation ζ and output voltage E, subject to the linear system

$$E(\zeta) = a\zeta + b \tag{5.1}$$

where a is the calibration factor and b relates to the still water level. b is disregarded, as the mean of a given time series is subtracted from the series itself to obtain the oscillation around the mean free-surface. The probes are then mounted in a jig, and at each relative submergence to the starting point the output voltage is measured. The data points are then plotted and linearly interpolated to find the calibration factor, see Figure 5.4.

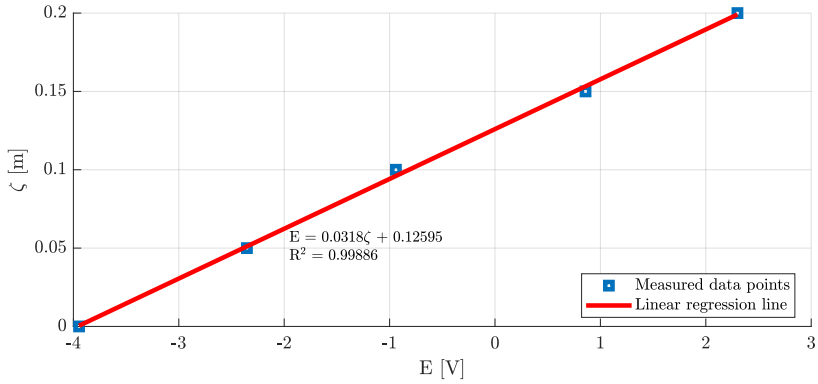

Figure 5.4: Example of the procedure in the wave probe calibration. The R^2-value indicates linearity in the measurements.

Before the wave probe calibrations, the probes were cleaned to remove debris and dirt that potentially could corrupt the readings. Wave probes are sensitive to potential temperature changes in the water, but this was not measured.

With the mass of the model relatively small, it was important to diminish the effect of the wave probe wiring. This was achieved by routing the wiring as seen in Figure 5.5.

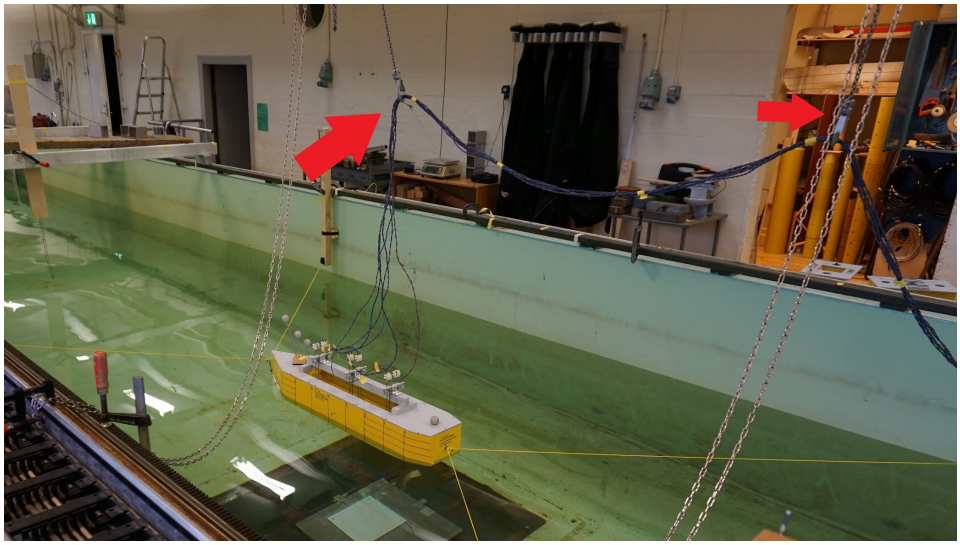

Figure 5.5: M1 model. Photo of the routing of wave probe wiring. The wiring are given some slack above the model, and is then routed directly above the model, as the red arrows indicate, and then to the amplifier (not pictured).

Mooring Lines

The model was moored with four horizontal mooring lines, each in an angle of 45° relative to the model, routed through a pulley and connected to a spring with stiffness $k = 29.19$ Nm^{-1} (essentially the mooring line stiffness). The pulley and spring was mounted to the piece of wood seen directly below the left arrow in Figure 5.5. The mooring lines was constructed so they were parallel with VCG, the vertical centre of gravity, see Figure 5.6.

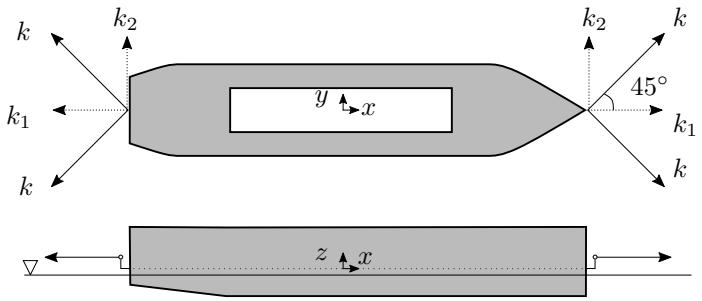

Figure 5.6: Layout of the mooring lines, each with stiffness $k = 29.19$ Nm^{-1}. k_1 and k_2 is the components of the mooring in the x -and y-direction, respectively.

The mooring component not shown in Figure 5.6 is the pretension, F_{pre}, due to the fact that the mooring springs are extent, applying a force on the model through the mooring lines. The pretension are measured by dividing the mean spring extension by the spring stiffness.

To replicate the experiments in the numerical simulations, the external system stiffness needs to be accounted for. As the mooring forces are acting through VCG, the only non-zero entries into the external stiffness matrix is

$$K_{11} = k_1 \tag{5.2}$$
$$K_{22} = k_2 \tag{5.3}$$
$$K_{55} = BF_{pre} \tag{5.4}$$

where $k_1 = k_2$ due to symmetry and F_{pre} is the component of the pretension in the x-direction.

To investigate whether the sloshing modes will influence the surge motion by being in proximity of it's resonance period, first and foremost for M1, we can look at the natural period in surge of the moored system, given by

$$\omega_{0,\eta_1} = \sqrt{\frac{k_1}{M + A_{11}}} \tag{5.5}$$

where $k_1 = 2k\cos(\pi/2) = 41.28$ Nm^{-1} is the spring stiffness' component in x-direction, $M = 5.839$ kg the model mass (cf. Table C.1) and $A_{11} \cong 1.1M$ the approximated added mass in surge. The natural frequency is then

$$\begin{aligned} \omega_{0,\eta_1} &= \sqrt{\frac{41.28}{2.1 \cdot 5.839}} = 1.8348 \text{ rad/s} \\ T_{0,\eta_1} &= \frac{2\pi}{\omega_{0,\eta_1}} = 3.4244 \text{ s} \end{aligned} \tag{5.6}$$

which is far from the first longitudinal sloshing mode at 0.5845 s (as predicted by (Molin et al., 2018)) and well outside the tested wave periods.

The procedure above works as an initial investigation on the system stiffness. Results from the decay test (Table 7.3) and simulations in WAMIT (Figure C.2) gives a natural period in surge of 2.15 s and 2.27 s, respectively, which is lower than the initial approximated of 3.43 s (Equation (5.6))

Thus, the surge natural period's interference with the sloshing modes for M1, due to the mooring lines, is a possible bias error that now can be disregarded.

Parabolic Beach and Wave Dampers

The parabolic beach is made up of a slotted plate, and it removes wave energy by triggering wave breaking. It's efficiency will decrease with shallow-water-waves, due to the hyperbolic decay of the waves' velocity components. Faltinsen (2006, Tab. 3.2) argues that the shallow-water approximation can be applied for $\lambda/h > 20$. In the present experiment, wave periods of 1.0 s yields $\lambda = 1.56$ m and further $\lambda/h = 1.95$, which indicates that the parabolic beach should function as expected.

The wave dampers, situated behind the parabolic beach, aims to calm down the now-irregular free-surface as much as possible.

Oqus

Oqus is used to measure the six degree-of-freedom motions by using four cameras which monitor the four marker spheres pictured in Figure 5.2. Oqus were set up so that the body motions were measured relative to the COG of M1.

5.1.2 Error Sources

A short discussion on possible error sources follows next. Due to small time frame, no repetition tests were conducted, and precision errors can't therefore be accounted for and/or quantified. Thus, a list of possible bias errors follow.

Tank wall effects between runs

The experiments are performed in a closed tank, resulting in noise propagation on the free-surface from waves being reflected by the walls for each run. The waiting time between

each run is chosen such that the free-surface was visually calm, that is, in $\mathcal{O}([\text{mm}])$. Tank wall effects may still be present, as the smallest waves ($H/\lambda = 1/100$, $T = 0.40$ s) have an amplitude of 1.25 mm, cf. Section 2.3.

It is believed that the parabolic beach and wave dampers' efficiency increase with the wave amplitude, as the relative ratio between reflections, visually observed, and waves become smaller.

Tank wall effects during runs

During runs, waves will be reflected from the model to the tank walls and back to the model again, interfering with the incident waves. Model responses may be increased, decreased or not affected by the reflected waves. During post-processing, time-series are consequently chosen before it is believed that reflected waves will interfere with the incident waves and model response.

Incident waves

Measurements with WP7 and WP8 during tests showed that waves did not always obtain the correct steepness, i.e. the wave amplitude were different than the prescribed one. This is accounted for in terms that the wave amplitudes measured during the runs are used in the post-processing. In general, the wave amplitudes were between $\pm 10\%$ to the prescribed, often with largest deviation for small wave amplitudes.

Mooring lines fastening

As stated, the mooring lines were fastened so that their resulting forces on the acted through VCG corresponding to M1. M2 and M3 have a VCG of 3 mm and 1 mm lower, respectively. This is not accounted for in the numerical replications, as it is assumed their contribution to be neglectable.

Pretension measurements

The pretension was measured based on the extension of the mooring springs. Here is an underlying bias error; the fact that springs in general have an "actuation" length before the springs will obey Hooke's law. This was not accounted for. Force transducers during the experiment was chosen to not be included, as these would, due to the small dimensions, contain noise in the same order as the measured quantities.

Submergence of the mooring lines

The mooring lines, if becoming submerged at some point during the tests, would induce non-quantifiable added inertia on the system. The mooring lines were observed during the largest waves and at the heave and pitch resonance periods, and were found to not being submerged during the tests.

Leakage behind the wavemaker

Leakage behind the wavemaker was noticed from the start of the experiments. The reason was that the wavemaker was newly installed, and the gaskets between the wavemaker and the tank walls did not work optimally. The lab staff believed, based on experience, that the Teflon railing between the wavemaker and the tank walls/bottom would degrade and further seal around the wavemaker. The experiments did not go on long enough to reveal if this was in fact the case.

To counteract the leakage, three pumps were installed, running in a cycle of two-on-one-off, based on the water level behind the wavemaker, leading to a non-uniform flow of water back to the tank, especially during wavemaker operation. A water depth between 0.79 m and 0.82 m was experienced.

Signal faults

A ”spike”, a large non-physical value, in the time series for various responses were sometime encountered, but never became an issue in the post-processing. One should nevertheless be aware of this, as it could provide non-physical results in the post-processing.

Wire routing of the wave probe wiring

As shown in Figure 5.5, the routing of the wave probe wiring needed to be carefully done. A concern was that it would induce a roll motion of the model. The roll motion was, by observing the Oqus output during the runs, small relative to for example pitch. Even though, the small roll amplitude could also arise from the model not being perfectly run in head sea.

Wave probe fastening

Figure 5.7 present a close-up photo of the terminal clamp used too fasten the wave probes to the body-fixed bracket. If fastened to tightly, the clamp may deform and alter the relative position of the two wave probe conductive cylinders and corrupt the results. As the wave probes were removed and calibrated each day, it was ensured that the screws were not overly tightened.

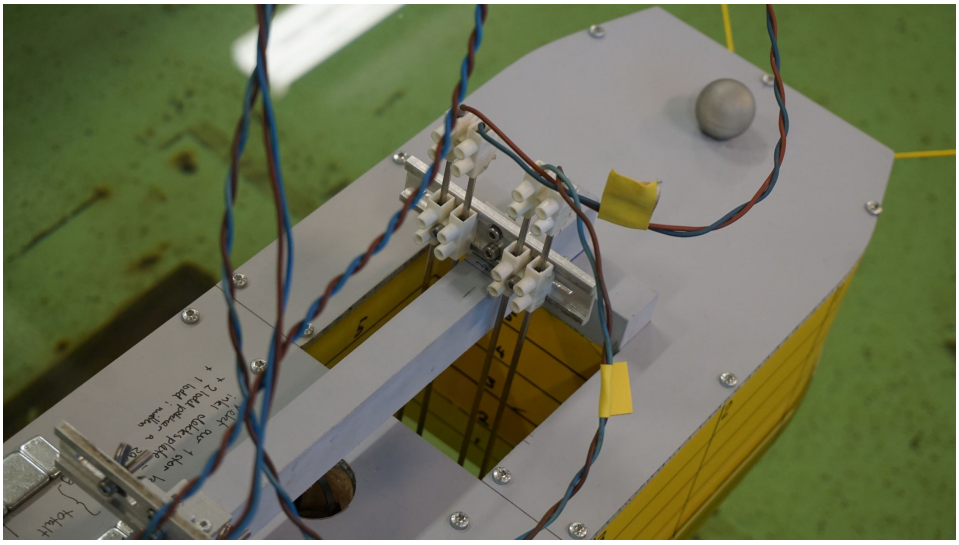

Figure 5.7: Close-up of the wave probe fastening by the use of an terminal clamp. The upper clamp connects the wiring to the conductive wave probe cylinders, while the lower connects the wave probe to the model.

5.2 Preparation and Analysis

5.2.1 Experiment Design

Before carrying out experiments, they have to be designed in a way that we are able to capture the wanted phenomena. In this case, we are interested in the piston and sloshing modes in the moonpools. For example, cf. Molin et al. (2018), the piston mode for a moonpool the same size as the moonpools in M2 and M3, the natural period is at $T = 0.59$ s, and the first sloshing mode for M1 is at $T = 0.58$ s. Thus, the periods $T = 0.40$ s to $T = 1.0$ s were chosen to run, which is in concordance with the periods used by Ravinthrakumar et al. (2020).

One test are made up of several runs, each run being regular waves of a given steepness and periods. To refine wanted sections, and to easier being able to throw away corrupted results, each test are split into three sub-tests, see Table 5.1.

Table 5.1: Overview of the tested periods. In total, each test consist of 45 runs with different period and same wave steepness, where there is an overlap at $T = 0.60$ s and $T = 0.70$ s. ΔT is the increment in wave period between each run.

	T_{min} [s]	T_{max} [s]	ΔT [s]
Sub-test 1	0.4	0.6	0.010
Sub-test 2	0.6	0.7	0.010
Sub-test 3	0.7	1.0	0.025

Three wave steepnesses are tested, see Section 2.3, chosen to be $H/\lambda = 1/100, 1/60$ and $1/30$. This results in 27 distinct runs, as there are 3 different moonpool configurations, and each test is split into three.

Through pre-testing, it was found that a waiting time between runs for sub-tests 1 and 3 of 180 s was sufficient, while it was extended to 300 s for sub-test 2. In each run, 150 waves are created for sub-tests 1 and 2, while 100 are created for sub-test 3. In order to have reference measurements for the surge, sway and heave response, each test was run for 10 s before the wavemaker started to oscillate.

5.2.2 Wave Maker Calibration

As the wavemaker was newly installed, it needed to be calibrated. The wavemaker oscillates in a piston-motion with a prescribed amplitude and period (equal to the prescribed wave period). The wavemaker stroke-to-wave amplitude ratio is found from a mechanical transfer function subject to the relative water depth kh, k the wave number (and inherently the prescribed wave period) and h the water depth. Please refer to Hughes (1993) for further information.

Using the mechanical transfer function, readings of the wavemaker oscillation amplitude showed it's amplitude to be lower than the prescribed. This is partly due to 3D- and inertia effects: that the wave maker is accelerating water, both in the tank and the leaked water behind it.

Thus, a second mechanical transfer function was made, to ensure correct wavemaker amplitude. This was done by iteration: prescribe a set of wave amplitudes and periods, measure the wavemaker amplitude and compare it with the prescribed (theoretical) amplitude, until the results converged between successive iterations.

With the wavemaker now having correct amplitude, we turn towards the waves it generate. Wave measurements at the mean model position (15.11 m from the wavemaker, cf. Figure 5.3) showed discrepancies in the experienced wave amplitudes compared to the theoretical. This is believed to be mostly tank-wall effects. A third mechanical transfer function was then constructed, to further alter the wavemaker amplitude, so that the wave amplitudes in the mean model position were according to the prescribed.

The procedure above was carried out for all steepnesses, and the transfer functions for $H/\lambda = 1/60$ is presented in Figure 5.8

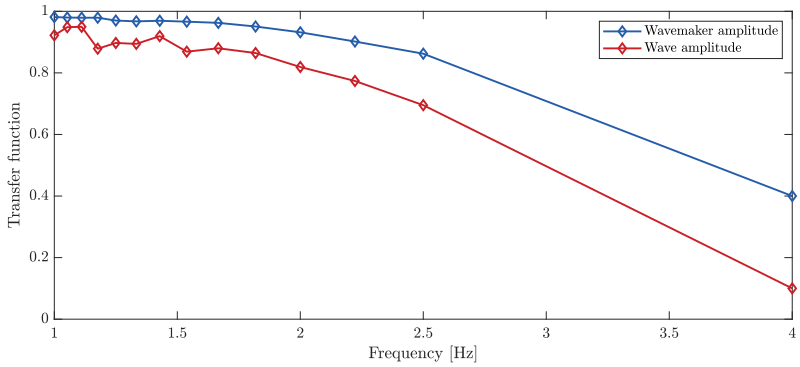

Figure 5.8: Mechanical transfer functions as a function of the wavemaker frequency for $H/\lambda = 1/60$. The legend denotes the transfer functions for the wavemaker and wave amplitude, which further increase the wavemaker amplitude.

5.2.3 Filtering

During the experiments, signals were sampled at 200 Hz and passed through a 20 Hz Butterworth-filter, which is designed to give as flat frequency response in the passband as possible, thus minimizing it's effect on the signals in the passband.

5.2.4 Decay Test

During the experiments, decay tests for all six DOFs were performed. The motivation to perform the decay tests was to find the natural period in the given DOF and configuration. The damping coefficients can also be found, following the procedure of e.g. Faltinsen (1990), and used as input in WAMIT, but this is not done.

A single DOF were isolated, e.g. in heave the model was forced to a larger draft and then released. This was repeated for three or four times for each configuration and DOF. The natural period are found by taking the time between successive peaks (or troughs) in the time signal after the model is released. Time series for the decay tests are provided in Appendix C.1.4, and the results for all six DOFs are presented in Table 7.3.

5.3 Post-processing

Most of the post-processing was spent to obtain response amplitudes, with the following methodology:

1. Reset the surge, sway and heave position using the measured 10 s window run at the start each test by subtracting the mean.

2. Measure the waves using WP7 and WP8 and use the mean of these as the incident wave amplitude, in case of any discrepancies, in later processing. Waves are measured from when steady-state waves are present at WP7 and WP8 until reflected

waves from the model are expected to interfere with the wave probes. Measured waves during the M3 tests are presented in Figure 5.10 and in Figures C.14 and C.15 for M1 and M2, respectively.

3. For each run, obtain the whole signal, i.e. the response from the 100 or 150 waves, as well as half the waiting time between runs on either side. The signal, ranging from either 90 or 150 s before the waves reach the model and until 90 or 150 seconds after the last wave reached the model, is then band-passed with cut-off frequencies $\pm 20\%$ of it's first harmonic, being the incident wave frequency. The "padding" on either side of the response signal ensure that the band-pass functions optimally.

4. Each run is then plotted, as well as a vertical line indicating where reflections may occur. An interval to calculate the response amplitude is then manually chosen, see Figure 5.9. Figures C.12 and C.13 are examples of time series which haven't reached steady-state conditions, and the interval had to be qualitatively chosen.

    - As WAMIT obtain the rigid body motions at the origin of it's global coordinate system, being at the mean free-surface, and experimental results are obtained at the COG of M1, corrections are made following the procedure in Section 5.3.1.

5. Using the chosen interval, each peak and through is found, and the response amplitude is found from averaging half the distance between successive peaks and troughs.

    - It was considered to use a Fast Fourier transform (FFT) on this interval, but this was not done, as the uniformity in the signal, e.g. comparing Figure 5.9 and Figures C.12 and C.13, largely will influence the output of the FFT.

6. Having both the response amplitude and the incident wave amplitude, the RAO is then found, see Section 5.3.2.

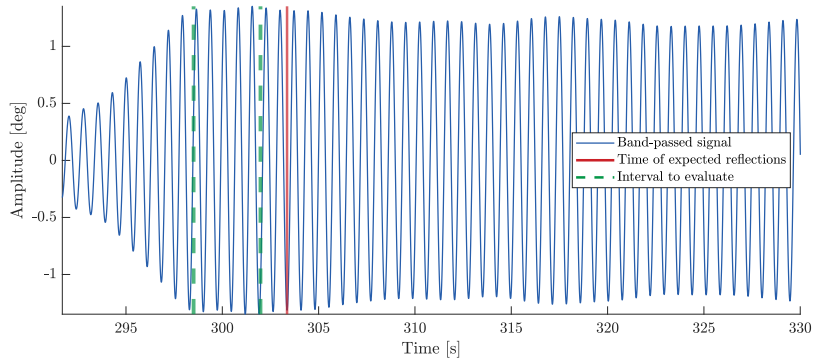

Figure 5.9: Time series of the pitch response of M3 for $T = 0.725$ s. The line indicating expected reflections are calculated using the incident wave group speed, and taken from when the first fully built-up wave (the wavemaker's stroke length are linearly ramped for five wave periods) hit the model and until the reflected wave (of the same group speed) hit the tank wall and returned back to the model. Assuming the origin of this wave to be at the model COG, this wave has travelled 2.5 m (the tank width), cf. Figure 5.3.

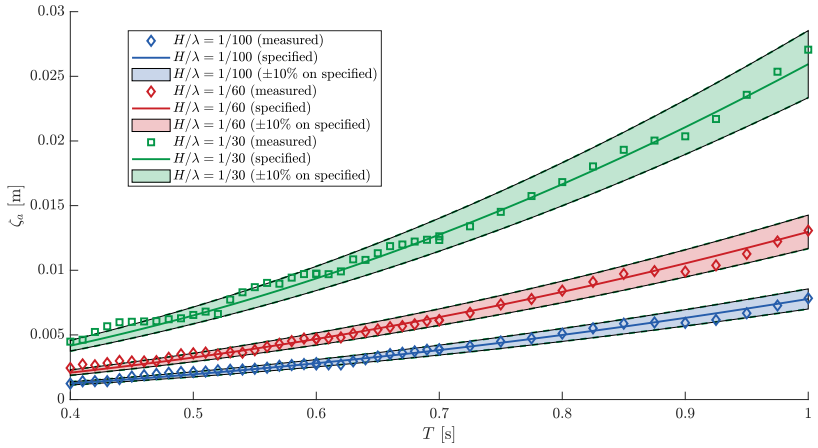

Figure 5.10: Measured and theoretical wave amplitudes at each wave period during the M3 tests. A interval of $\pm 10\%$ to the specified wave amplitude is shown. In general, most waves are inside this interval.

5.3.1 Coordinate System

The experimental wave probe signals are measured relative to a body-fixed coordinate system, meaning the free-surface elevation an observer standing at the moonpool will observe. These signals inherently contain the local heave motion of the model, $s_{3,local}$, given by

$$s_{3,local} = \eta_3 + y\eta_4 + x\eta_5 \tag{5.7}$$

where x and y is the position of the wave probe and η_3, η_4 and η_5 is the heave, roll and pitch motion of the model, cf. the coordinate system in Figure 5.3 and probe layout in Figure C.1. The earth-fixed wave probe signal $\zeta_{wp,EF}$ can then be found from

$$\zeta_{wp,EF} = \zeta_{wp,BF} - s_{3,local} \tag{5.8}$$

where the subscripts EF and BF denote earth-fixed and body-fixed surface elevation at the wave probe, respectively.

Corrections to match experimental and numerical results (according to WAMIT's coordinate system) is, exemplified in surge, to find the local contribution in surge due to pitch,

$$\eta_{1,local} = z\eta_5 \tag{5.9}$$

where z is equal to VCG of M1 and subtract this from the surge time series.

5.3.2 RAO Calculation

When the incident wave and response amplitude is obtained, the Response Amplitude Operator (RAO) can be calculated. The RAO describes a linear relation between the response amplitude and the incident wave amplitude, and is commonly denoted $H(\omega)$, where ω is the angular frequency of the incident wave. In general, the RAO for a given response amplitude $\eta_{j,a}$ and incident wave amplitude ζ_a is given by

$$H_j(\omega) = \frac{\eta_{j,a}}{\zeta_a} \tag{5.10}$$

The pitch amplitude, experimentally given in degrees, are converted to radians and non-dimensionalised with the wave number k,

$$H_5(\omega) = \frac{\eta_{5,a}}{k\zeta_a} \tag{5.11}$$

The remaining responses follow Equation (5.10), i.e.

$$H_{wp,EF}(\omega) = \frac{\zeta_{wp,EF,a}}{\zeta_a} \tag{5.12a}$$

$$H_{wp,BF}(\omega) = \frac{\zeta_{wp,BF,a}}{\zeta_a} \tag{5.12b}$$

$$H_1(\omega) = \frac{\eta_{1,a}}{\zeta_a} \tag{5.12c}$$

$$H_3(\omega) = \frac{\eta_{3,a}}{\zeta_a} \tag{5.12d}$$

for the earth-fixed moonpool free-surface elevation, body-fixed moonpool free-surface elevation, surge response and heave response. As the wave probes are transversely coupled

two-by-two (WP1-WP2, WP3-WP4 and WP5-WP6), it is expected that the free-surface elevation will be approximately the same, given that their spacing is 0.033 m (Figure C.1), and it is assumed that no transverse sloshing is present. This is presented in Figure 5.11.

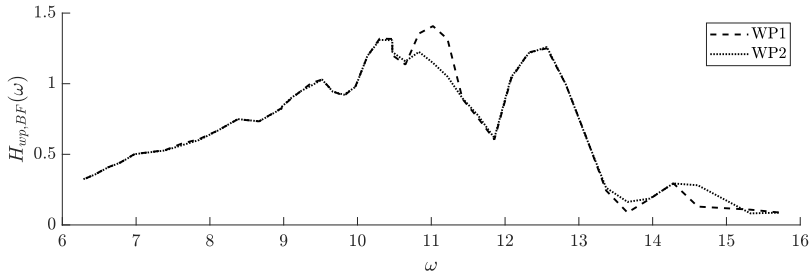

Figure 5.11: RAOs for WP1 and WP2 for M1 in incident waves of steepness $H/\lambda = 1/30$. A discrepancy can be seen around $\omega = 11$ rad/s (given in model scale), as well as for large ω, assumed to arise from problems similar to Figures C.12 and C.13.

Chapter 6

Parametric Study

This chapter describes the methodology of the parametric study that is carried out. The motivation for the study is to study the effect of the moonpool width-to-vessel beam ratio in operational conditions, in terms of the response. Six moonpool width-to-vessel beam ratios are tested.

6.1 Assumptions and Limitations

The parametric study is carried out assuming freely-floating conditions and finite water depth, similar to the experimental water depth. In an attempt to compare the experimental results with the ones obtained in this study, a quasi-experimental RAO is constructed, consisting of the experimental RAO and extended with the RAO from the parametric study at low frequencies. The reason is to be able to include the selected range of sea states. A change is thus made from moored to freely-floating conditions, and it is thus assumed that the vessel will follow the surface elevation at small wave frequencies if we neglect the effect from the mooring.

We are extending the study to full-scale, assuming a scale of 1:138. The dimensions of the vessel is thus a length of 138 meters, beam of 27.6 meters, and the water depth is 110.4 meters, cf. Table C.1.

6.2 Geometry

The setup are as in terms of moonpool width b to vessel beam B ratio,

$$\frac{b}{B} = 0.250,\ 0.375,\ 0.500,\ 0.625,\ 0.750,\ \text{or}\ 0.875$$

For M1, the moonpool length is kept constant. For M2 and M3, the moonpools are kept square. The geometries for M1 and M3 can be seen in Figures 6.1 and 6.2, respectively. The mesh size are kept similar to the mesh size found from the mesh convergence study in Section 4.3.

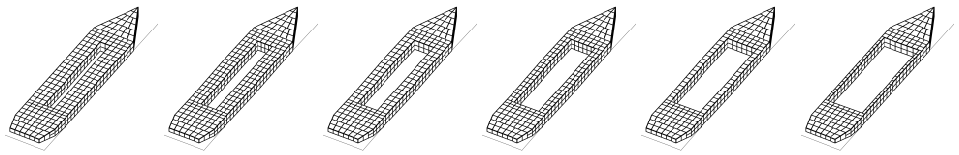

Figure 6.1: M1 parametric setups

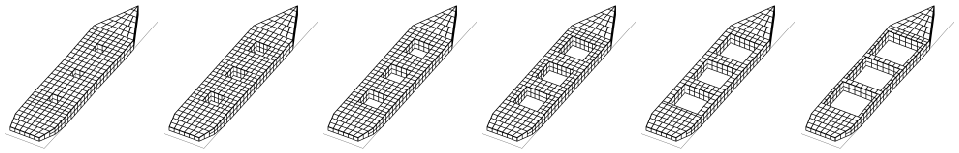

Figure 6.2: M3 parametric setups

6.3 Sea States

The applied sea states are chosen based on representative data of the joint significant wave height, H_S, and spectral peak period, T_p, in the northern North Sea from Faltinsen (1990), reproduced in Table D.1. The methodology for choosing the sea states was to choose the most probable H_S based on the selected peak periods. The selected sea states are meant to cover a wide range of operational conditions one can encounter in the northern North Sea. The sea states can be seen in Table 6.1.

Table 6.1: Sea states with most probable significant wave height H_s at the given spectral peak periods, T_p.

Sea state no.	1	2	3	4
H_s	2 m	2 m	3 m	3 m
T_p	6 s	8 s	10 s	12 s

The sea states in Table 6.1, obtained from the northern North Sea, are thus subject to to JONSWAP (Joint North Sea Wave Project) wave spectrum (DNV GL, 2018), given by

$$S_\zeta(\omega) = A_\gamma S_{PM}(\omega)\gamma^{\exp\left(-0.5\left(\frac{\omega-\omega_p}{\sigma\omega_p}\right)^2\right)} \tag{6.1}$$

where

$$\begin{aligned} S_{PM}(\omega) =& \frac{5}{16}\cdot H_S^2\omega_p^4\cdot\omega^{-5}\exp\left(-\frac{5}{4}\left(\frac{\omega}{\omega_p}\right)^{-4}\right) \\ \sigma =& \begin{cases} 0.07, & \text{if } \omega \le \omega_p \\ 0.09, & \text{if } \omega > \omega_p \end{cases} \\ A_\gamma =& 1 - 0.287\ln\gamma, \end{aligned}$$

where S_{PM} denotes the well-known Pierson–Moskowitz wave spectrum. $\omega_p = 2\pi/T_p$ is the peak frequency, γ is the peak shape parameter and A_γ is a normalizing factor. An average value for data obtained on JONSWAP-described waves can be taken as $\gamma = 3.3$ (DNV GL, 2018). Note that with $\gamma = 1$, the JONSWAP spectrum is equivalent with the Pierson–Moskowitz spectrum. The spectra is presented in Figure 6.3.

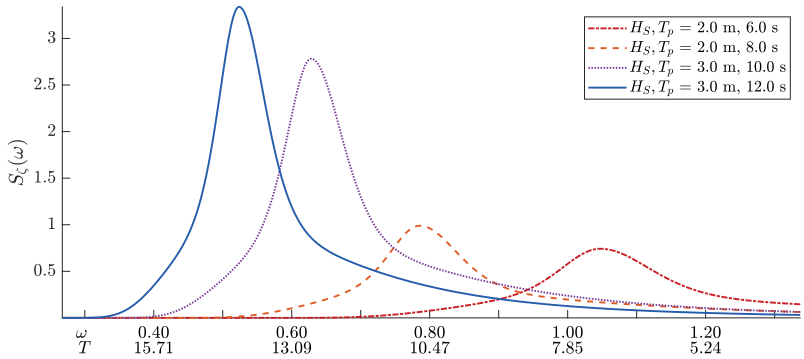

Figure 6.3: JONSWAP spectra for the selected sea states. The peak shape parameter $\gamma = 3.3$. Axes values are for the full-scale representation.

6.4 Response Calculation

The relation between an arbitrary wave spectrum $S_\zeta(\omega)$ and the resulting wave amplitude ζ_{ai} at the frequency ω_i is given by

$$S_\zeta(\omega_i)\Delta\omega = \frac{1}{2}\zeta_{ai}^2 \tag{6.2}$$

where $\Delta\omega$ is the difference between successive frequencies ω_i.
Assuming a linear system, an arbitrary response amplitude $\eta_{ai}(\omega_i)$ can be found from

$$\eta_{ai}(\omega_i) = H_\eta(\omega_i)\zeta_{ai}(\omega_i) \tag{6.3}$$

where $H_\eta(\omega_i)$ is the linear transfer function between the wave amplitudes ζ_a and response η_a. Now, as all terms in Equation (6.3) are real and positive, they can be squared, and if multiplied by $\frac{1}{2}$, we get

$$\frac{1}{2}\eta_{ai}^2\left(\omega_i\right) = H_\eta^2\left(\omega_i\right) \cdot \frac{1}{2}\zeta_{ai}^2\left(\omega_i\right) = H_\eta^2\left(\omega_i\right) \cdot S_\zeta\left(\omega_i\right)\Delta\omega \tag{6.4}$$

Using the same analogy as for the wave spectrum, the *response spectrum* can be defined as $S_\eta(\omega_i)\Delta\omega = \frac{1}{2}\eta_{ai}^2$, and thus the relation between the wave spectrum and response spectrum is obtained as

$$S_\eta(\omega) = H_\eta^2(\omega)S_\zeta(\omega) \tag{6.5}$$

where the transfer function for the response η is the RAO for the same η. Thus, we are able to calculate the response spectrum for in a given sea state for a given response.

The standard deviation of the response, σ_η, is given from

$$\sigma_\eta^2 = \int_0^\infty S_\eta(\omega)\mathrm{d}\omega \tag{6.6}$$

An example of the relation in Equation (6.5) can be seen in Figure 6.4 for the pitch response of M1. Differing from the presented pitch RAOs in this thesis, the units are herein given as degrees per incident wave amplitude, in order to obtain the standard deviation in degrees. For the body and moonpool responses, the units are still response amplitude per incident wave amplitude.

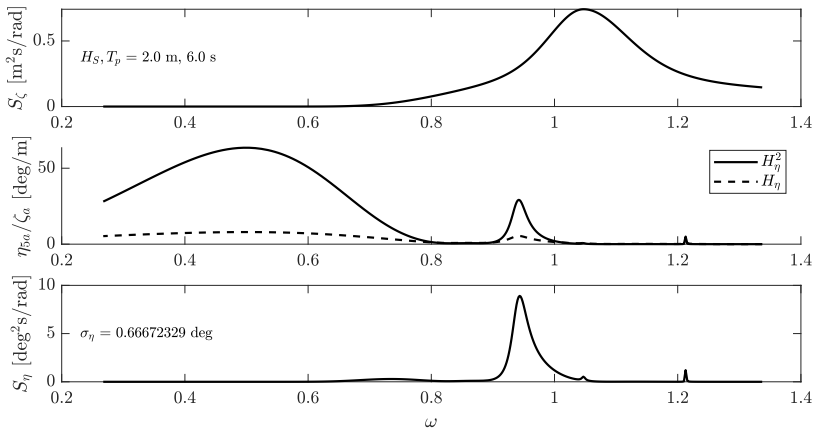

Figure 6.4: Example of response spectrum calculation for M1 and the pitch motion. The JONSWAP wave spectrum (upper) is multiplied with the square of the RAO (solid line in the middle) to obtain the response spectrum (lower). Note that the large pitch motions at small frequencies, due to the vessel "following" the wave, are not present in the response spectrum, as the wave spectrum have practically zero energy at these frequencies. The prominent responses are around $\omega \cong 0.94$ rad/s, where the pitch resonance frequency and the wave spectrum partly coincides.

For wave spectra, a well-known and used approximation (Faltinsen, 1990) is

$$H_{1/3} = 4\sqrt{\sigma_\zeta^2} \tag{6.7}$$

where $H_{1/3} \equiv H_S$ is the mean of the one third highest waves. In the literature, $H_{1/3}$ often refers to the mathematical relation while H_S refers to measurements, though they often are used interchangeably. σ_ζ^2 is commonly denoted m_0; the zeroth moment of the wave spectra.

Similarly as outlined in Equation (6.7), the variance σ_η^2 of a given response η, following the procedure in Figure 6.4, may be used to obtain the *significant response*,

$$\eta_S = 4\sqrt{\sigma_\eta^2} = 4\sigma_\eta, \tag{6.8}$$

thus relating the standard deviation of the response to a quantifiable order.

6.5 Scaling of the Experimental RAOs

As the experimental RAOs are based on regular, constant-steepness waves, they are not directly comparable with the waves of an irregular, in our case JONSWAP, wave spectrum. In an attempt to match these, we can calculate the mean wave steepness in a sea state, given the spectral peak period and the mean H_S, denoted $\bar{H_S}$, both given in and calculated from the scatter diagram in Table D.1, respectively.

The spectral peak period is used to find the wave length λ_p of its corresponding wave through

$$\lambda_p = \frac{g}{2\pi} T_p^2 \tanh \frac{2\pi}{\lambda_p} h, \tag{6.9}$$

where g is the gravitational acceleration and h is the finite water depth. The *significant wave steepness* is then simply found from $\bar{H_S}/\lambda_p$. The significant wave steepnesses are tabulated in Table D.2. In-between our peak periods of interest, from 6 to 12 seconds, the significant wave steepness is approximately a linear function of the peak period, see Figure D.1.

Thus, in order to match the experimental RAO to the given wave spectrum, we choose the experimental peak period, $T_{p,exp}$, as the point of interpolation. The "new" value of the RAO is then found based on the significant wave steepness for the spectrum, see Figure 6.5.

It is chosen to use a linear interpolation, even though the decay in RAO as a function of increasing steepness is expected to be a follow the trend of $1/x$, as the damping is quadratic as a function of the wave amplitude. Thus, the RAO is expected to have this behaviour, but the sparse amount of data points (3) and the fact that we are interpolating (and not extrapolating) made linear interpolation the best option. The trend is seen in Figure 6.5, but was not always the case for other RAOs.

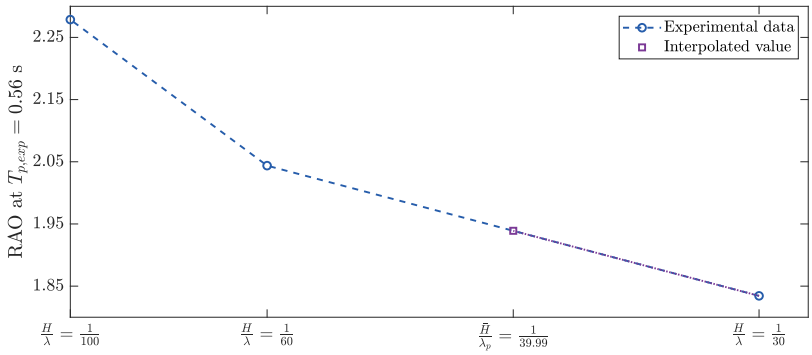

Figure 6.5: Interpolated RAO for the pitch motion of M1, assuming linear relation between the RAO and wave steepness at the peak period, cf. Figure D.1. Note that the unit of the RAO at the experimental peak period of $T_{p,exp} = 0.56$ s, is in degrees per incident wave amplitude, while the units are non-dimensionalised for the RAO presented in this thesis, see Figure 7.13(a). The experimental peak period corresponds to non-dimensional experimental frequency $\omega^* = 1.6$.

We then take the interpolated value of the RAO (at $T_{p,exp} = 0.56$ s) given in Figure 6.5 and scale down the experimental RAO of steepness $H/\lambda = 1/60$. Note that the scaled RAO, which now relates to the given JONSWAP wave spectrum, always is scaled down, as the smallest significant wave steepness in our sea states is $\bar{H}_S/\lambda_p = 1/56.30$ (Table D.2). The experimental RAO is scaled down based on the ratio of the interpolated value and the value of the RAO of $H/\lambda = 1/60$. This is illustrated in Figure 6.6.

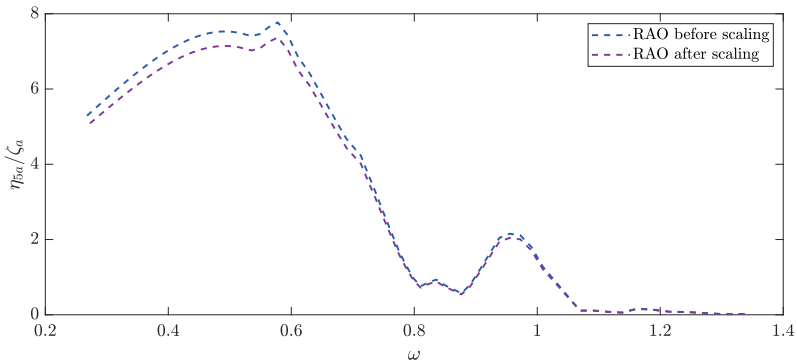

Figure 6.6: Scaled RAO for the pitch motion of M1. Vertical axis units are degrees-per-incident wave amplitude. Full-scale values for the wave frequency ω is provided. The scaling is based on the ratio at $\omega = 0.94$ rad/s, cf. Figure 6.5. ($T_{p,exp} = 0.56$ s therein).

The experimental RAOs are only obtained for full-scale wave frequencies of $0.53 \leq \omega \leq 1.34$ rad/s. Figure 6.3, the sea state spectra, demands the RAO to be extended down to $\omega = 0.27$ rad/s. The experimental RAO is then joined with the RAO obtained from

WAMIT for $\omega < 0.53$ rad/s for all modes except surge, where the WAMIT RAO is taken from $\omega < 0.71$ rad/s for M1 and $\omega < 0.67$ rad/s for M2 and M3. This is to remove the effect of the mooring lines, as seen from Figure C.2 to yield resonance periods when moored. All adapted RAOs can be seen in Appendix D.1.2.

Chapter 7

Results

This chapter present the findings and results of this thesis. A summarising conclusion and recommendation for further work are found in Chapter 8.

Non-dimensional RAOs

Throughout this chapter, RAOs are given on the non-dimensional form

$$\omega^* = \omega\sqrt{\frac{B}{g}} \text{ [-]} \tag{7.1}$$

where B is the beam of the vessel, cf. Table C.1 and g is the gravitational acceleration. Throughout this chapter, when reading the RAO figures, Table 7.1 can be used to quickly convert to incident wave period or full-scale angular frequency. The reason is that snapshots of the moonpool response are described using the incident wave period. Throughout this chapter, the non-dimensional frequency and wave period are simultaneously given if the latter is given. Table 7.1 may then work as a tool for the reader to study non-mentioned phenomena in another time-frame than the provided.

Table 7.1: Conversion from selected model wave periods T to non-dimensional frequencies ω^* and full-scale angular frequencies ω_{FS}. A scale of 1:138 is imagined.

T [s]	0.50	0.51	0.52	0.53	0.54	0.55	0.56	0.57	0.58	0.59	0.60	0.61	0.62	0.63	0.64	0.65
ω^* [-]	1.79	1.76	1.73	1.69	1.66	1.63	1.60	1.57	1.55	1.52	1.50	1.47	1.45	1.42	1.40	1.38
ω_{FS} [-]	1.07	1.05	1.03	1.01	0.99	0.97	0.96	0.94	0.92	0.91	0.89	0.88	0.86	0.85	0.84	0.82

7.1 Piston and Sloshing Modes for the Present Geometry

Table 7.2 present the piston and first to third sloshing mode for the present geometry, cf. Table C.1. The modes are according to the theory of Molin et al. (2018) in finite water depth of 0.8 m.

Table 7.2: Piston and first to third sloshing mode for the present geometry, cf. Table C.1. The modes are according to the theory of Molin et al. (2018).

	Model scale period, T		Non-dimensional frequency, ω^*	
	M1	M2,M3	M1	M2,M3
Piston mode	0.6344 s	0.5881 s	1.4140	1.5255
1st sloshing mode	0.5845 s	0.3540 s	1.5348	2.5341
2nd sloshing mode	0.5122 s	0.2530 s	1.7515	3.5457
3rd sloshing mode	0.4458 s	0.2066 s	2.0125	4.3416

7.2 Decay Test

Table 7.3 present the results from the decay tests for all six rigid-body motions for M1, M2 and M3. Appendix C.1.4 present all non-filtered time series used to determine the natural periods.

Table 7.3: Result from decay test, given in model scale period T and non-dimensional frequency ω^*.

	Model scale period, T						Non-dimensional frequency, ω^*					
Mode	Surge	Sway	Heave	Roll	Pitch	Yaw	Surge	Sway	Heave	Roll	Pitch	Yaw
M1	2.27 s	4.21 s	0.62 s	1.32 s	0.64 s	1.28 s	0.40	0.21	1.45	0.68	1.41	0.70
M2	2.55 s	4.17 s	0.72 s	1.07 s	0.70 s	1.85 s	0.35	0.22	1.25	0.84	1.28	0.48
M3	2.48 s	4.69 s	0.67 s	1.09 s	0.68 s	1.33 s	0.36	0.19	1.35	0.83	1.33	0.68

I general, both decay tests for heave and pitch seems to give a larger natural period than experiments and numerical simulations. For example, Figure 7.13, the pitch RAOs for M1 and M2, predicts natural periods of $\omega^* \cong 1.60$ and $\omega^* \cong 1.57$, respectively. The decay tests yield thus a 11.88% and 18.47% lower frequency ω^* for M1 and M2, respectively, compared to numerical and experimental results.

The reason seems to be coupling between the rigid-body motions during the decay tests. Appendix C.1.5 presents the decay tests of M1 in surge, heave and pitch and remaining signals of the five other rigid-body motions. It is found that coupling between rigid-body motions during the decay tests is a main candidate to explain these discrepancies.

7.3 Experimental Results

7.3.1 Earth-fixed Moonpool Response

The presentation of body-fixed and Earth-fixed moonpool response RAOs is herein discussed. The difference is that the body-fixed representation is relative to a coordinate system following the rigid body motion(s), and is what an observer would experience if present at the moonpool, while the Earth-fixed representation is relative to a coordinate system at rest.

Figures 7.1 and 7.2 present body-fixed and Earth-fixed moonpool response RAOs at the fore and middle wave probes, respectively.

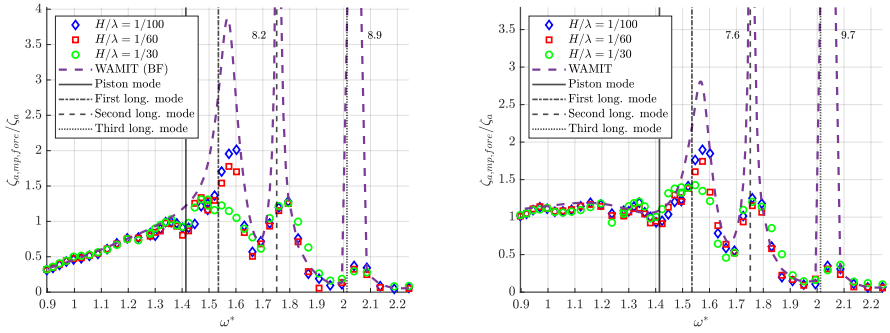

(a) Body-fixed **(b)** Earth-fixed

Figure 7.1: Body- and Earth-fixed RAO for fore wave probes in M1.

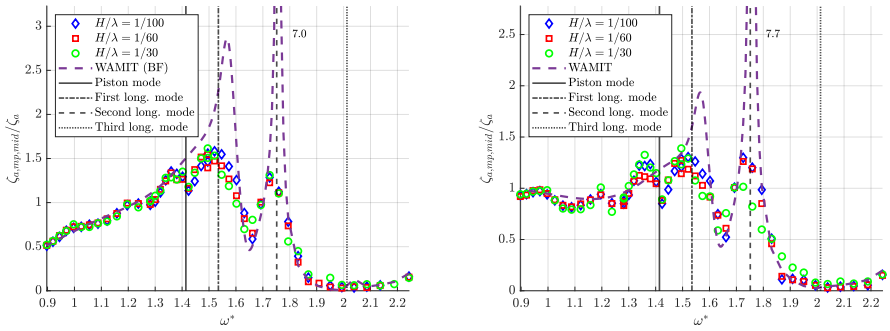

(a) Body-fixed **(b)** Earth-fixed

Figure 7.2: Body- and Earth-fixed RAO for middle wave probes in M1.

Relative differences between wave steepnesses around $\omega^* = 1.55$ at the fore wave probes, Figure 7.1, are assumed to be caused by non uniform time series, discussed in Figures 5.9, C.12 and C.13. Due to the post-processing methodology, the time intervals

for the body- and Earth-fixed over which the given response amplitude is found are not equal, and the results around $\omega^* = 1.55$ can't be directly compared.

Both the body-fixed and Earth-fixed representations successfully captures the piston mode and first to third sloshing modes. It is unclear whether the piston and first sloshing mode appear as a joint coupled mode; as is what WAMIT predicts, given by the peak at $\omega^* \cong 1.57$ (Figures 7.1 and 7.2). It is further unclear whether the experimental results at the vertical line denoting the piston mode frequency are cancellations or wall effects.

As expected, the middle wave probes fail to detect the third sloshing mode as the mode has a node in the middle of the moonpool.

As Figures 7.1 and 7.2 shows, both body-fixed and Earth-fixed representations successfully captures the predicted modes. It is therefore concluded to present remaining moonpool response results using body-fixed representations, as this provides a more intuitive and physical representation of the moonpool resonance problem in terms of marine operations. This is shown by the denotation BF in relevant legend entries.

7.3.2 Post-processing After the Occurence of Reflections

Results from processing response time series are herein presented. Two methods is used: obtaining the response amplitude before or after one expect reflected waves from the model to reach the model and thus interfere with the rigid-body motions. Figures 7.3 and 7.4 present comparisons of the two methods for M1 in heave and pitch, respectively. Figure 7.5 present RAOs obtained by processing moonpool responses for M1 after reflected waves have reached the model.

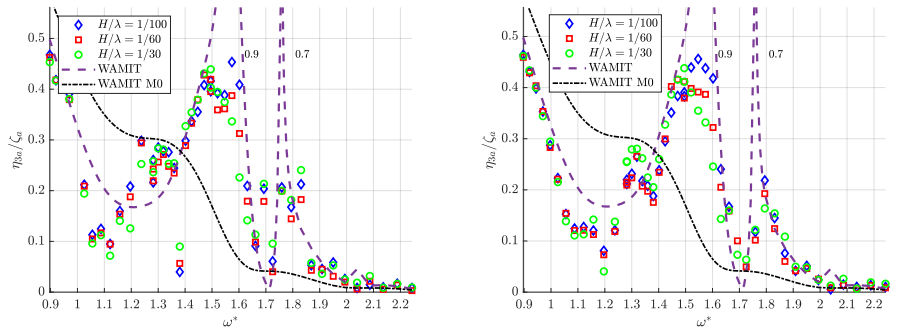

(a) Deep into time series

(b) Before reflections

Figure 7.3: Comparison of the heave RAO for M1; processing of results before (b) or after (a) reflected waves have reached the model.

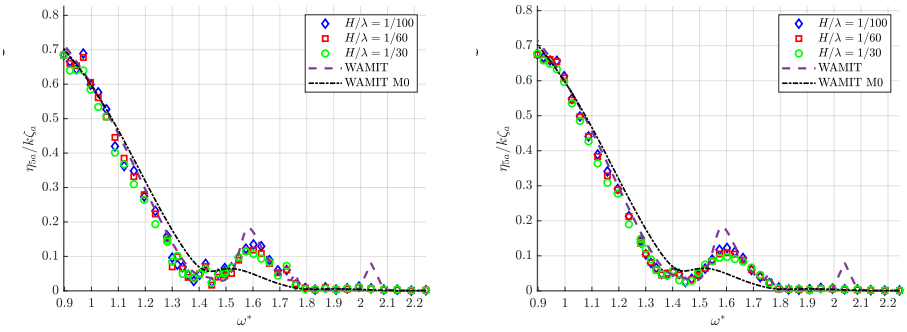

(a) Deep into time series

(b) Before reflections

Figure 7.4: Comparison of the pitch RAO for M1; processing of results before (b) or after (a) reflected waves have reached the model.

The heave response, Figure 7.3, is clearly influenced by reflected waves at small ω^*. There is also not a distinct peak in the natural frequency around $\omega^* \cong 1.55$ when processing after reflections, Figure 7.3(a), which indicate that the heave response is damped by the reflective waves. Comparing the sub-figures at $\omega^* \cong 1.70$, the WAMIT-predicted cancellation is captured only when processing before reflective waves reach the model.

In pitch, Figure 7.4, there is good agreement between the methods at large ω^*, but the effect of reflective waves become more apparent at small ω^*.

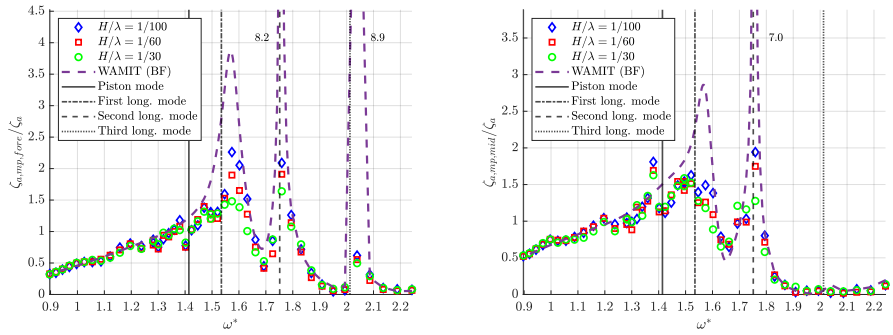

(a) Fore wave probes, deep in time series

(b) Middle wave probes, deep in time series

Figure 7.5: Moonpool RAO for M1 for fore and middle wave probes. Aft is given in Figure E.1, and is similar to the fore wave probes.

The moonpool responses processed after reflections, Figure 7.5, differ from the rigid body motions. By comparing Figure 7.5 with Figure 7.8 (aft and middle moonpool RAO for M1 processed before reflections) , we obtain more distinct peaks at the combined peak and first sloshing mode, second sloshing mode and third sloshing mode, when processing the results after reflected waves interferes with the model. This is clearly seen at the second sloshing mode comparing Figures 7.5(a) and 7.8(a), which represent better agreement

between WAMIT (and as theoretically predicted by Molin et al. (2018), Table 7.2) and experimental results when the response is obtained after reflections are present.

A reason for this may be, even though the rigid body motions are affected by reflective waves, that the moonpool response have reached steady-state behaviour, cf. Figure C.13. However, we must be careful when using this. Even if this method agrees better with the numerically obtained natural frequency, the reflective waves' phase, in the mentioned example at the second sloshing mode, seems to be (partly) in-phase with the moonpool response, which is seen from the larger value of the RAO between Figures 7.5 and 7.8 and the larger response amplitude in Figure C.13.

7.3.3 M1

Results from M1 is herein presented, starting with results from accessible literature on a geometry equal to M1 that is briefly compared with the present work. Sloshing modes and surge response are then further discussed. Secondary resonance is mentioned, but not investigated.

Results from Ravinthrakumar et al. (2020)

Ravinthrakumar et al. (2020) and Ravinthrakumar (2020) (the latter is a PhD thesis, the former is work included in this), carried out numerical and experimental simulations on a vessel of equal geometry to M1. The scale to the present geometry is 4:1, i.e. the present geometry is $^1/_4{}^{\text{th}}$ the spatial dimensions and the mass is $^1/_{64}{}^{\text{th}}$ the mass of the comparable vessel, by the use of Froude scaling.

Figures 7.6 and 7.7 present the comparison between the results of Ravinthrakumar et al. (2020) and the presently obtained results in heave and pitch, respectively.

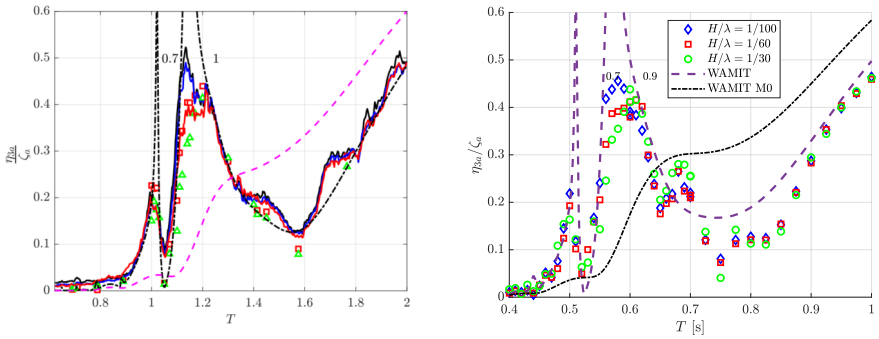

(a) Comparable vessel

(b) Present vessel

Figure 7.6: Comparison of heave RAOs for M1, given by the incident wave period T. Periods from Ravinthrakumar et al. (2020) are directly scalable by a factor $^1/_2$, due to the fact that the scale is 4:1 and Froude scaling is used. The legend of sub-figure (a) is seen in Figure 7.7.

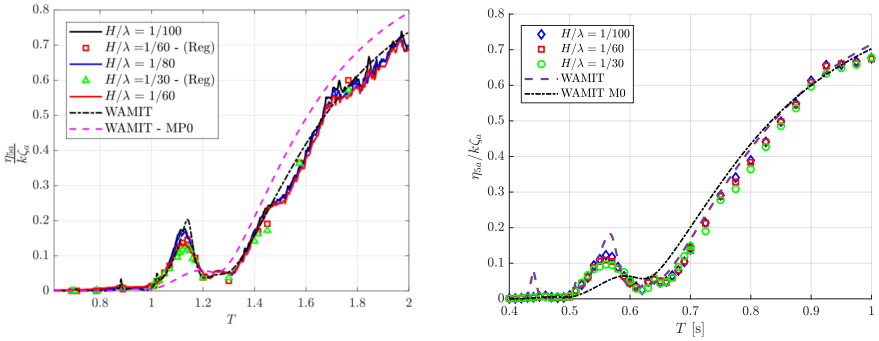

(a) Comparable vessel

(b) Present vessel

Figure 7.7: Comparison of pitch RAOs for M1, given by the incident wave period T. Periods from Ravinthrakumar et al. (2020) are directly scalable by a factor $1/2$, due to the fact that the scale is 4:1 and Froude scaling is used. Solid lines in sub-figure (a) denotes a therein-developed spectra based on constant-steepness regular waves, markers are regular waves similar to the presently-used regular waves.

From comparison of heave RAOs, Figure 7.6, good agreement is found for $T < 0.65$ s (in the scale of the present study) in terms of agreement between experimental results and WAMIT simulations. Discrepancies is found for $0.65 < T < 0.9$ s, which is believed to be caused by a non-steady state signal (as we process data before reflective waves reach the model), e.g. similar to Figure C.13.

Figure 7.7, the pitch RAOs, shows good agreement for all periods in terms of RAO value and comparison to numerical results. A difference is the natural pitch period at $T \cong 0.57$ s (for the present study) compared to the one of Ravinthrakumar et al. (2020). The reason is that they used the same mooring layout as in the present study with springs of stiffness 90 Nm^{-1}. By the use of Froude scaling, this yields 5.63 Nm^{-1} for the present study (dimensional study of scaling factor $\lambda = 4$: $[\frac{\text{N}}{\text{m}}] = [\frac{\text{kg}}{\text{s}^2}] = \frac{\lambda^3}{\lambda} = \lambda^2$), while the mooring springs in the present study have a stiffness of 29.19 Nm^{-1}. This affect mostly the pitch peak period and the simulations of M0 (MP0 for the comparable vessel) when comparing Figures 7.7(a) and 7.7(b).

Sloshing Modes

The moonpool response for M1 is herein further discussed. The appearance of the combined piston and first sloshing mode, which also is discovered by Ravinthrakumar et al. (2020), and the second and third sloshing mode is already mentioned in Sections 7.3.1 and 7.3.2. Figure 7.8 present the moonpool response for M1 at the fore and middle wave probes.

Figures 7.9 to 7.11 present snapshots of the first, second and third sloshing mode of M1, respectively.

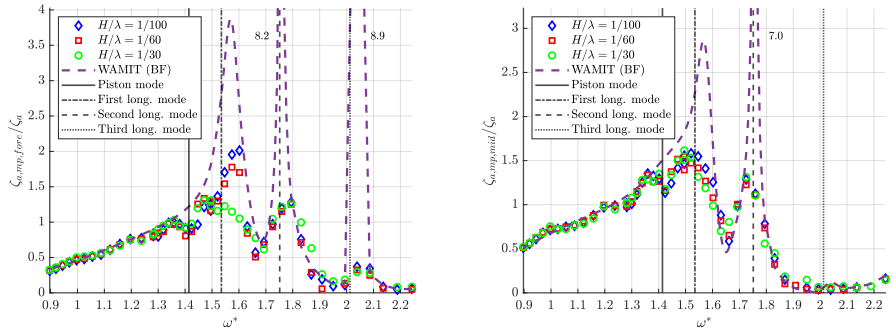

(a) Fore wave probes

(b) Middle wave probes

Figure 7.8: Moonpool RAO for M1 for fore and middle wave probes. Aft is given in Figure E.1, and is similar to the fore wave probes.

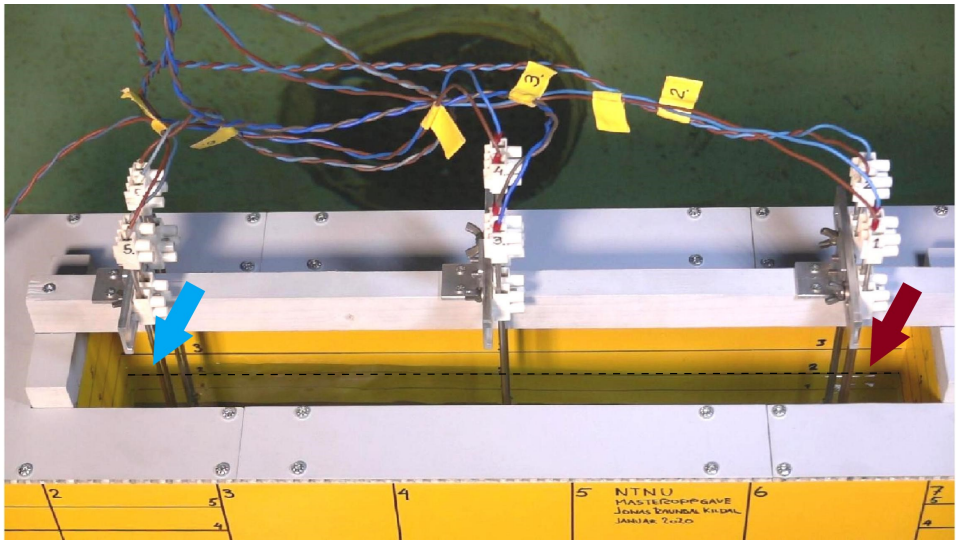

Figure 7.9: Snapshot for the first sloshing mode in M1 at $T = 0.57$ s ($\omega^* = 1.57$). The peak is shown with the blue arrow, the trough with burgundy, and the mean free-surface as the dashed black line. The vertical distance between the horizontal markings on the hull is 0.025 m.

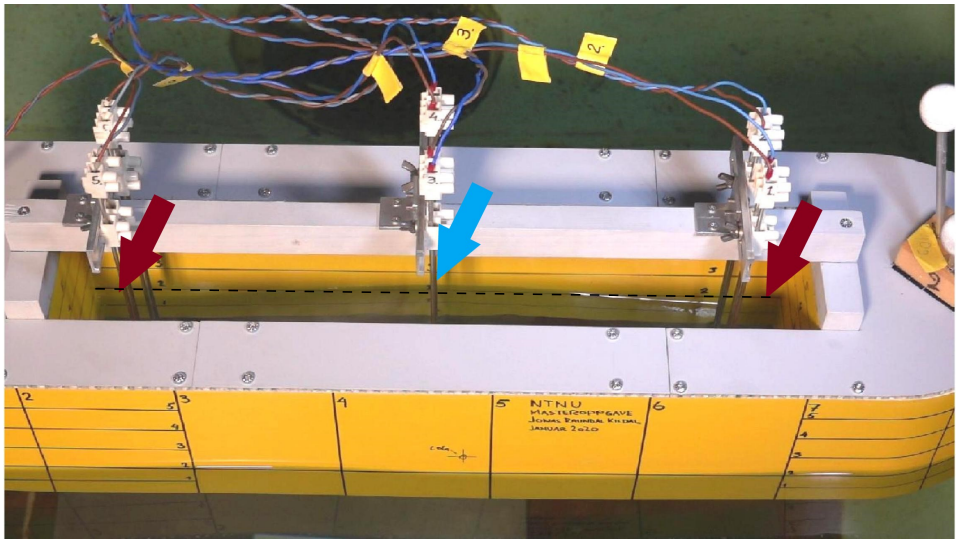

Figure 7.10: Snapshot for the second sloshing mode in M1 at $T = 0.51$ s ($\omega^* = 1.76$). The peak is shown with a blue arrow, troughs in burgundy, and the mean free-surface as the dashed black line. The vertical distance between the horizontal markings on the hull is 0.025 m.

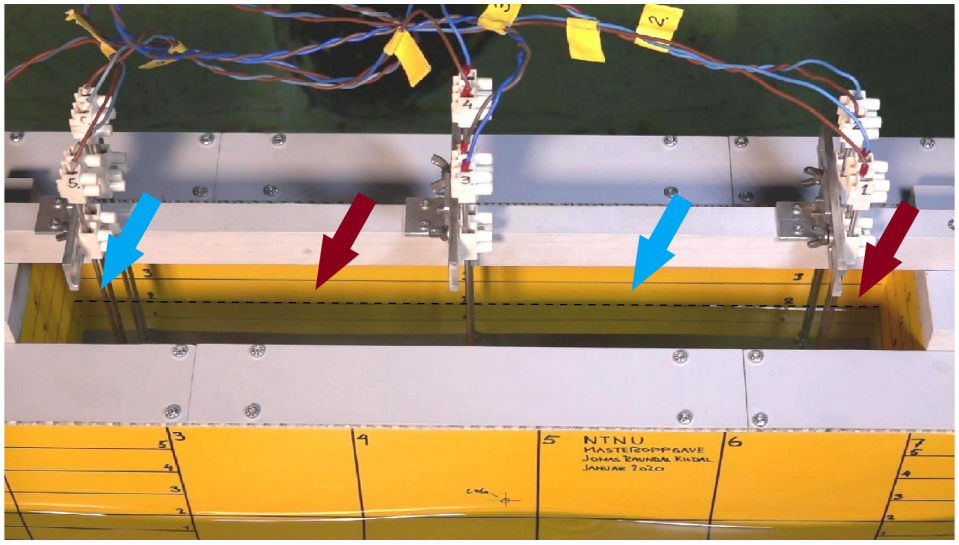

Figure 7.11: Snapshot for the third sloshing mode in M1 at $T = 0.44$ s ($\omega^* = 2.04$). Peaks are shown with blue arrows, troughs in burgundy, and the mean free-surface as the dashed black line. The vertical distance between the horizontal markings on the hull is 0.025 m.

As Figure 7.8 present, especially the combined piston and first sloshing mode and third sloshing mode natural frequencies are somewhat shifted when comparing experimen-

tal/numerical to theoretical (cf. Table 7.2) natural frequencies. This is due to the *hydrodynamic interaction*. In reality, hydrodynamic interaction depicts the pressure an arbitrary floating object A "feels" through the fluid from floating object B when B is for instance accelerated. The term is adapted to the present case when talking about the coupled vessel and moonpool response. Theoretical models, like the one of Molin et al. (2018), does not account for this interaction.

Secondary Resonance

For the present study, secondary resonance is not investigated. This could be done by processing the moonpool response around it's higher-order harmonics and following the procedure described in Section 5.3.

Secondary resonance is observed in the M1-equivalent model in Ravinthrakumar et al. (2020), and is expected to be observed at the present study as well.

7.3.4 Surge Response

The effect of the sloshing modes on the surge response of the vessel is herein presented. The surge response RAO for M1 and M2 are presented in Figure 7.12. The presence of sloshing modes in M1 and the presence of only the piston mode in M2 is already described, and won't be repeated here.

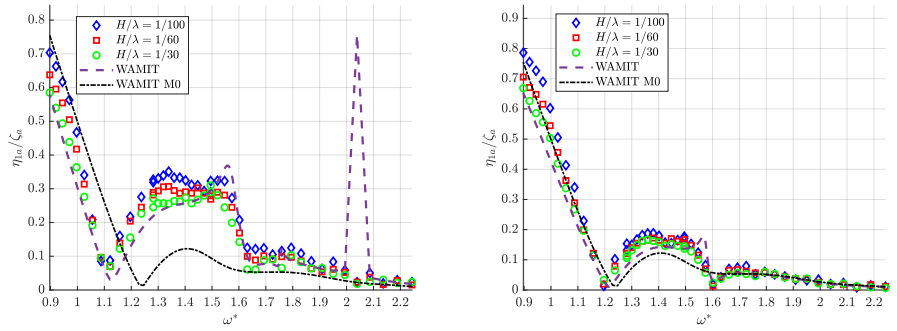

(a) M1 **(b)** M2

Figure 7.12: Surge RAO for M1 and M2. M3 is given in Figure E.6, and is similar to M2.

Comparing Figures 7.12(a) and 7.12(b), the surge response of M2 is approximately twice as low compared to M1 at $1.20 \lesssim \omega^* \lesssim 1.55$. This interval coincides partly with the joint piston mode and first sloshing mode frequency apparent in M1, see Figure 7.1(a). Thus, the appearance of sloshing, especially the first mode, seems to influence the surge response of the vessel. This is seen for M2, Figure 7.12(b), where no sloshing is apparent, that the surge response is lower than for M1 in the same interval. M2 (and M3) is in fact close to M0, the vessel with no moonpools.

The large peak in numerical simulations (at $\omega^* \cong 2.05$) in Figure 7.12(a) coincides with the third sloshing mode (see Figure 7.1(a)), and is largely over-predicted as the wave radiation damping is small.

7.3.5 Pitch Response

The pitch response RAOs for M1 and M2 are presented in Figure 7.13.

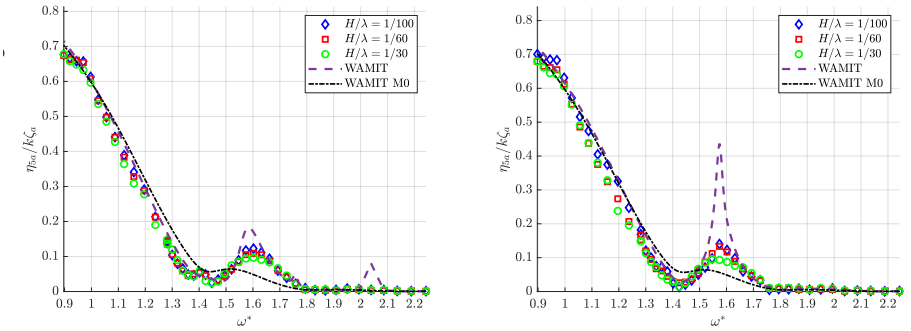

(a) M1 **(b)** M2

Figure 7.13: Pitch RAO for M1 and M2. M3 is given in Figure E.5, and is similar to M2.

Figure 7.13(a) show better accordance between experimental and numerical results, compared to Figure 7.13(b).

According to Section 3.7.1, the two moonpools in M2 (Figure 7.13(b)) are 180 degrees out-of-phase in the forced pitch motion at the natural piston mode period. Though, having freely-floating conditions, hydrodynamic interaction and an assumed moonpool and outer fluid-domain coupling during the experiments, we can't draw the conclusion that the moonpools are *exactly* 180 degrees out-of-phase, but it seems fair to assume that they are to some extent out-of-phase. This then explains the large peak in numerical simulations at the pitch natural frequency, $\omega^* \cong 1.57$ in Figure 7.13(b). The difference in experimental results and numerical simulations around the pitch peak frequency is thus explained by flow separation at the moonpool inlets, an effect not captured by WAMIT. Though, in pitch for M2, flow separation originating from the moonpool piston modes is thus seen as a larger dampening mechanism than wave radiation.

Comparing Figures 7.13(a) and 7.13(b), the flow separation at the moonpool inlets seem to account for a larger part of the damping in pitch for M2 compared to M1, as argued above.

WAMIT predict a smaller peak in numerical simulations at the pitch natural frequency for M3, Figure E.5, compared to M2, Figure 7.13(b). The reason may be a larger extent of coupling of the three moonpools in M3, hydrodynamic interaction and an assumed moonpool and outer fluid-domain coupling, as the numerical simulations are run in freely-floating conditions (replicating the experiments).

7.3.6 Moonpool Response Cancellation for M3

An observed cancellation in moonpool response for the aft moonpool for M3 is herein presented. The moonpool response RAOs for all three moonpools in M3 are presented in Figures 7.14 to 7.16. Figures 7.17 and 7.18 present photos during the experiments capturing the mentioned cancellation. The photos are taken in waves of steepness $H/\lambda = 1/30$.

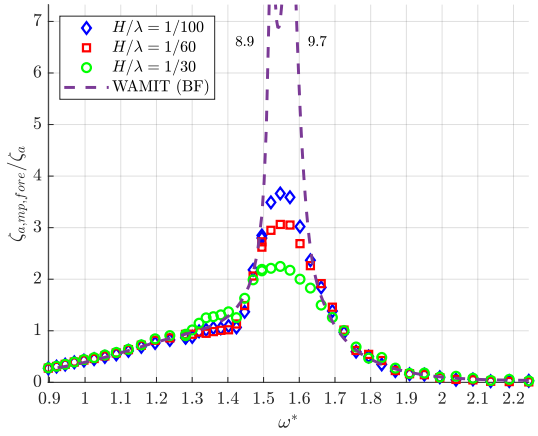

Figure 7.14: Fore moonpool RAO for M3.

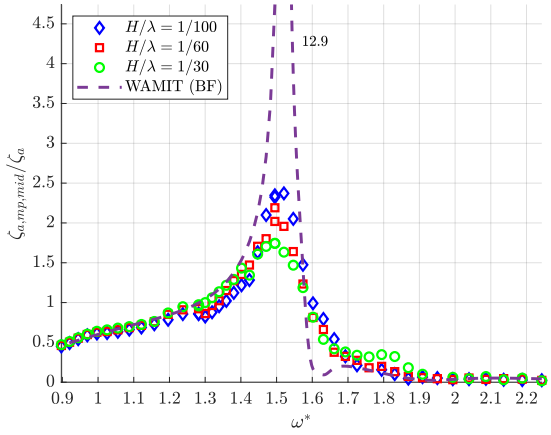

Figure 7.15: Middle moonpoool RAO for M3.

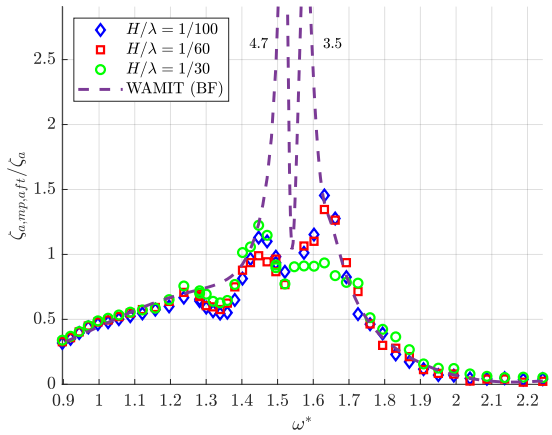

Figure 7.16: Aft moonpool RAO for M3.

Figures 7.14 to 7.16 indicate a cancellation effect in the aft moonpool at $T = 0.59$ s ($\omega^* = 1.52$). At $T = 0.60$ s ($\omega^* = 1.50$), there is less indication of cancellation, as seen by comparing the RAO values(Figure 7.16): approximately 0.75 at $T = 0.59$ s and approximately 1.0 at $T = 0.60$ s.

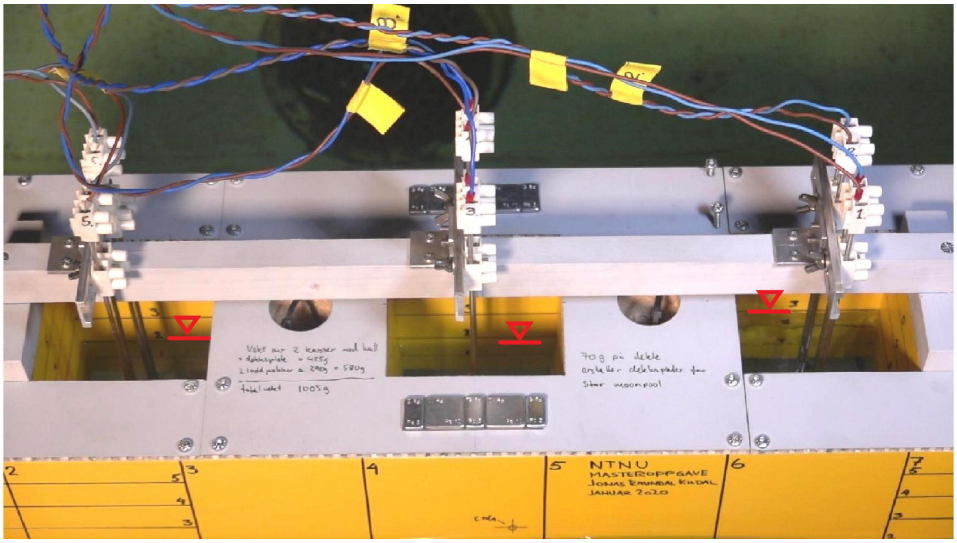

(a) $t = 7.61$ s

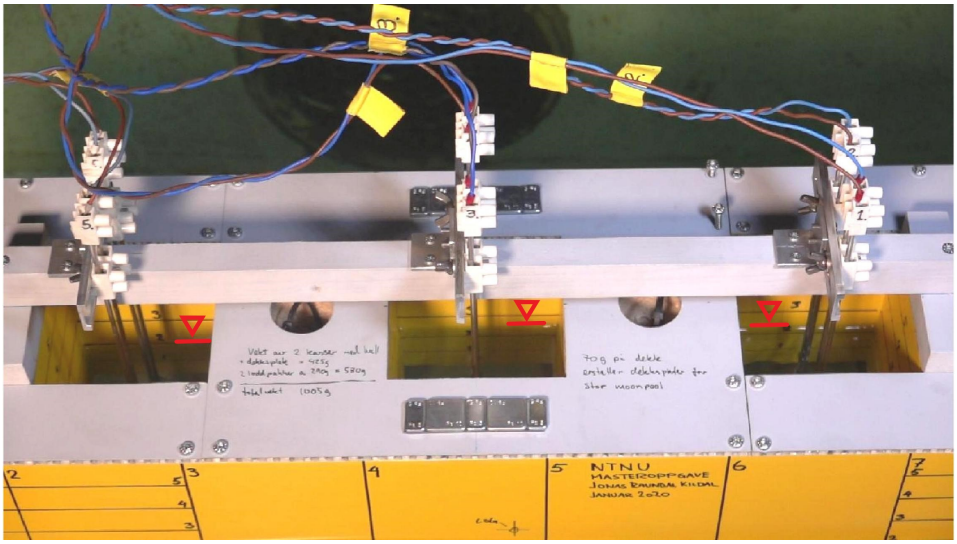

(b) $t = 7.61 + \frac{1}{4}T$ s

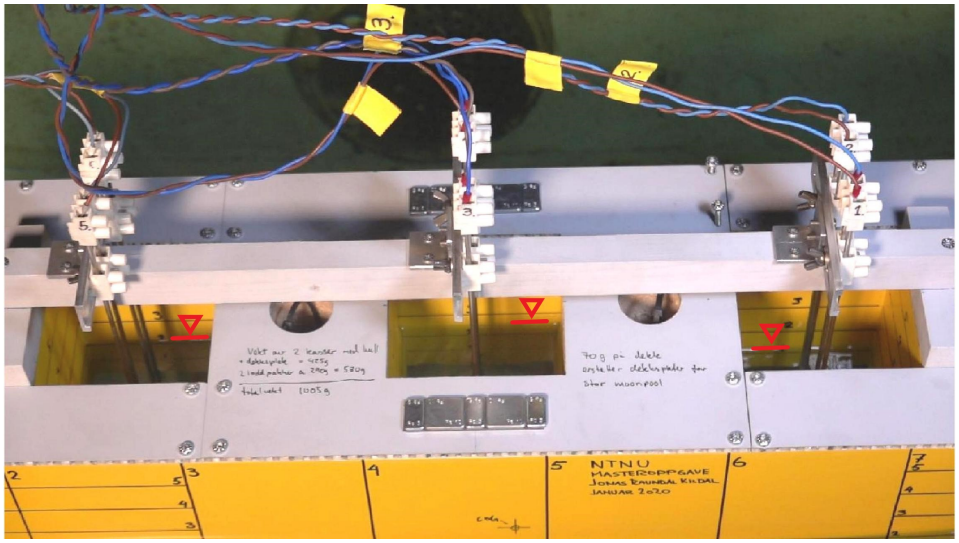

(c) $t = 7.61 + \frac{2}{4}T$

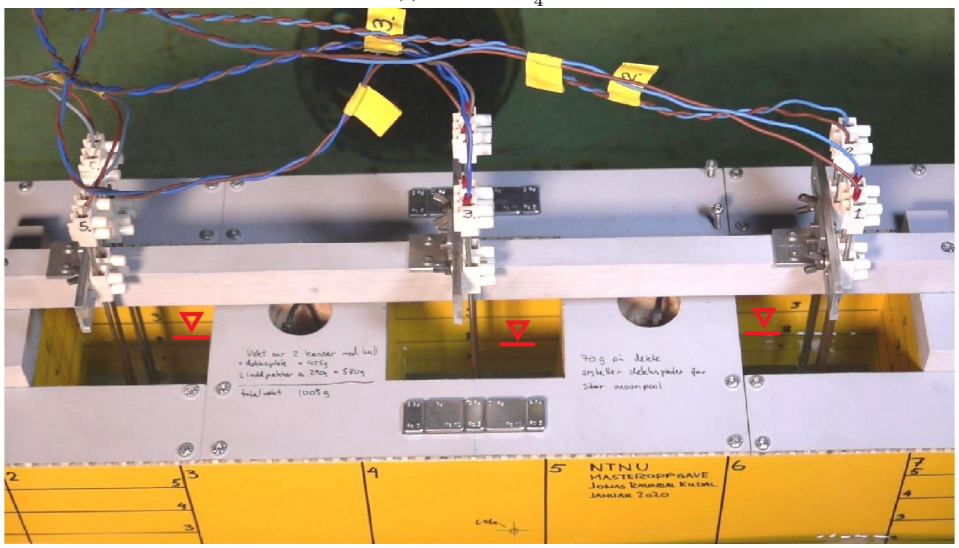

(d) $t = 7.61 + \frac{3}{4}T$ s

Figure 7.17: Video snapshots taken from starboard side during experiments for M3 at $T = 0.59$ s ($\omega^* = 1.52$) in waves of steepness $H/\lambda = 1/30$. The drawn red triangles and lines show the instantaneous moonpool free-surface elevation. The wave period T is used in the instantaneous time at each snapshot to show the harmonic motion of the moonpool free-surface. The vertical distance between the horizontal markings on the hull is 0.025 m.

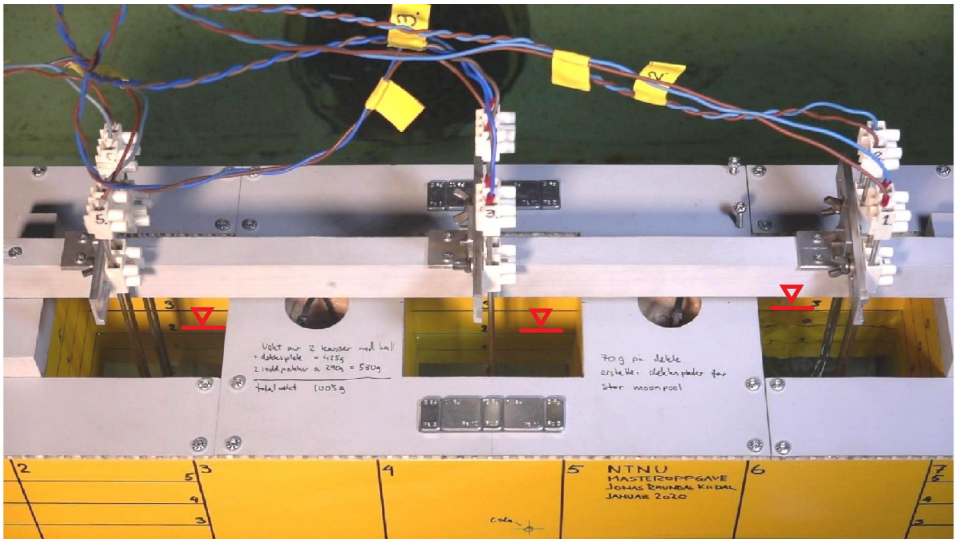

(a) $t = 11.54$ s

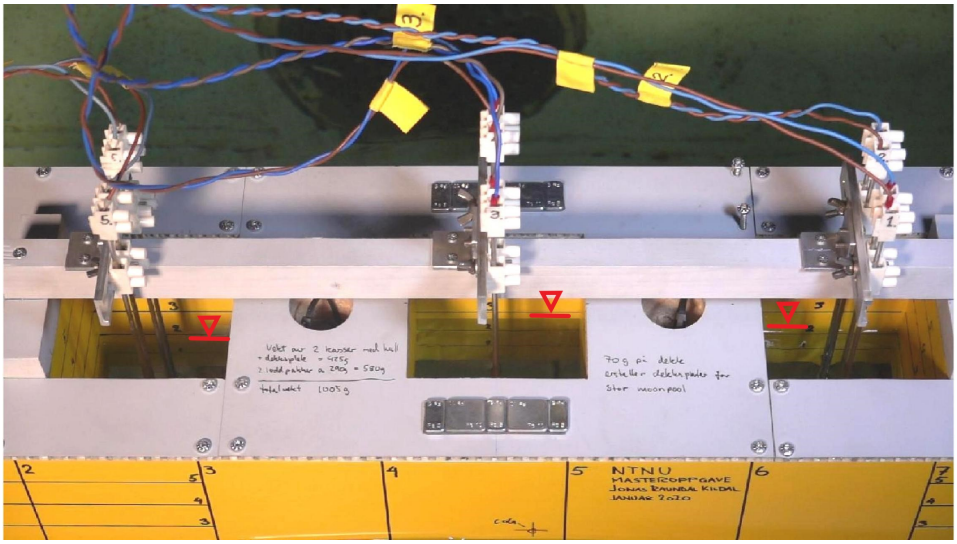

(b) $t = 11.54 + \frac{1}{4}T$ s

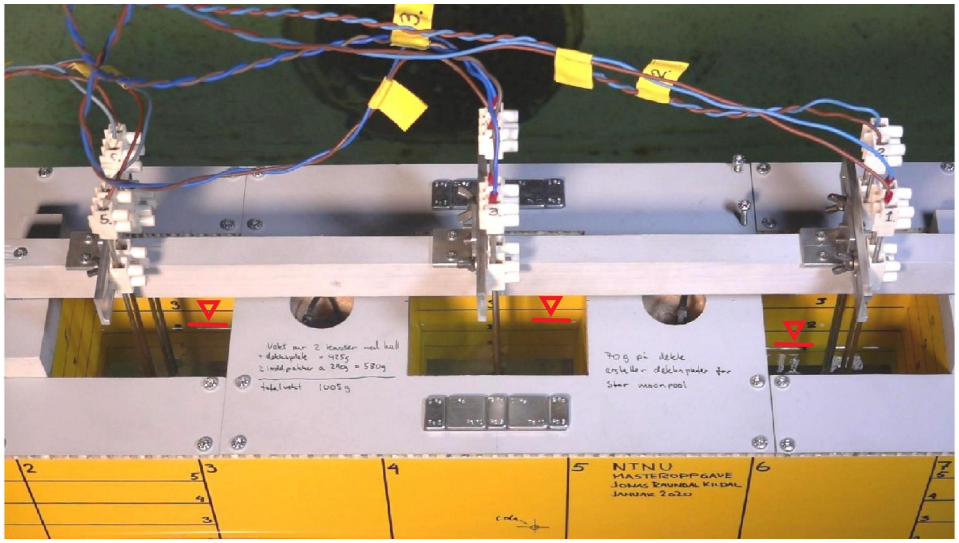

(c) $t = 11.54 + \frac{2}{4}T$

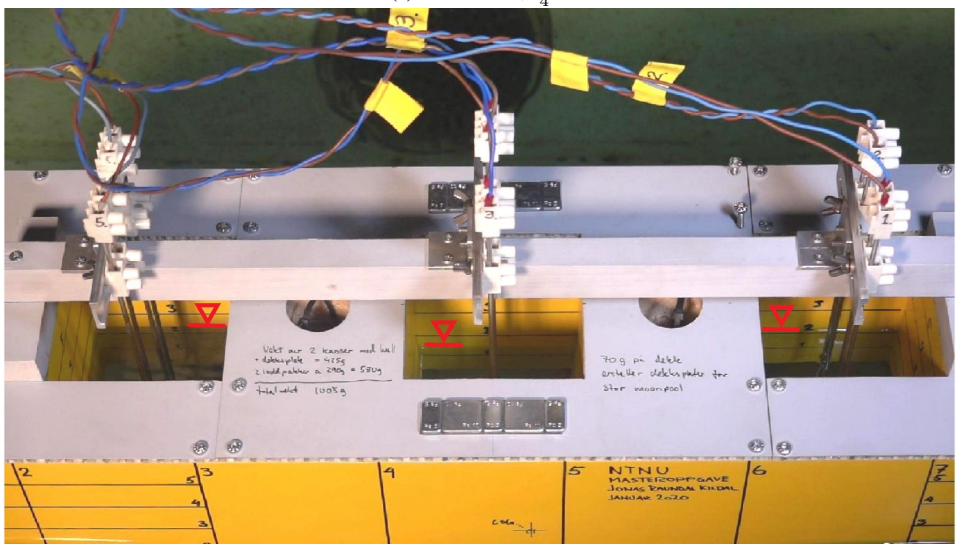

(d) $t = 11.54 + \frac{3}{4}T$ s

Figure 7.18: Video snapshots taken from starboard side during experiments for M3 at $T = 0.60$ s ($\omega^* = 1.50$) in waves of steepness $H/\lambda = 1/30$. The drawn red triangles and lines show the instantaneous moonpool free-surface elevation. The wave period T is used in the instantaneous time at each snapshot to show the harmonic motion of the moonpool free-surface. The vertical distance between the horizontal markings on the hull is 0.025 m.

Figures 7.17 and 7.18 prove that there indeed is cancellation, as shown through the comparison of the aft moonpool response in the two figures. Table 7.4 present the direction of the free-surface elevation between time instants in Figure 7.18.

Table 7.4: Instantaneous moonpool free-surface elevation in Figure 7.18. The arrows depict the free-surface's movement along the positively upwards z-axis from each time instant to the next. The relation (d)→(a) follows because the snapshots are divided in four time-instants by $^1/_4{}^{th}$ the wave period T.

Time instant	Aft	Middle	Fore
(a)→(b)	↓	↑	↓
(b)→(c)	↑	↓	↓
(c)→(d)	↑	↓	↑
(d)→(a)	↓	↑	↑

We are in proximity to the piston mode natural frequency, see Table 7.2, which excites large moonpool responses. The reason for the cancellation is mainly that the moonpools are out-of-phase, especially the middle and aft, as seen in Table 7.4, where the two free-surfaces always are moving in the opposite direction, indicating a 180 degrees relative phase difference.

The fore and middle moonpool seem to be somewhat in-phase, see Table 7.4. They are in-phase at time instants (b)→(c) and (d)→(a), indicating a 90 degrees relative phase difference.

There is also indication on cancellation in M2, cf. the fore and aft moonpool response in Figures E.3 and E.4, but there is not taken video of this.

7.3.7 Coupled Moonpool and Vessel Responses

The coupled moonpool and vessel responses in terms of the heave response of the vessel is herein presented and discussed.

In Section 7.3.3, hydrodynamic interaction is argued as a reason for the shift in moonpool response resonance frequency for M1.

For the configurations M2 and M3, similar effects, though not as strong, is observed. Molin et al. (2018), not accounting for the hydrodynamic interaction or cross-moonpool interactions, predicts a natural non-dimensional frequency of $\omega^* = 1.5255$ (cf. Table 7.2) for the piston mode in each of the moonpools of M2 and M3. Figures E.3 and E.4, the moonpool response RAOs for M2, predict a somewhat larger natural frequency. It is assumed that the irregularities around $\omega^* \cong 1.3$ and $\omega^* \cong 1.5$ in Figure E.4 is due to cancellations or non-steady state behaviour in the time series.

Heave Cancellation

Figure 7.19 presents the heave RAOs for M1 and M3.

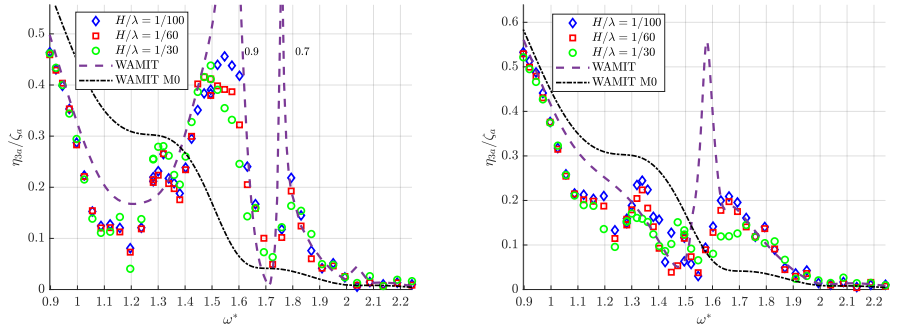

(a) M1 **(b)** M3

Figure 7.19: Heave RAO for M1 and M3. M2 is given in Figure E.2, and is similar to M3. The discrepancies for $H/\lambda = 1/30$ for M3 at $\omega^* \cong 1.65$ is believed to be caused by non-uniform time series.

Figure 7.19 indicates a clear difference in the heave RAO between M1 and M3 at $\omega^* = 1.5255$; in proximity of the theoretical piston mode frequency for M2 and M3. The main difference between the M1 moonpool response and the one of M2/M3 is that the M1 moonpool response is a combination of the piston mode and first sloshing mode, while the response of M2/M3 is originating from the piston mode, see Figure 7.8(a) and Figures 7.14 to 7.16.

The reason is believed partly to be the different dynamics of the moonpool responses. As argued in Section 7.3.5, flow separation at the moonpool inlets is an important dampening mechanism for M2 (and herein also M3), which will act as an ”effective” tool to remove energy from the system, thus dampening the heave motion (in this example).

Flow separation is also an important dampening mechanism for M1, but due to the larger moonpool volume (as may be described by the moonpool volume-to vessel volume), the moonpool response couples easily with the outer fluid domain, which is then described by wave radiation.

Though hard to quantify and describe the difference in heave cancellation between M1 and M3 in Figure 7.19, we believe that the extent of flow separation and relative moonpool phases as described in Section 7.3.6 may be main candidates to explain these phenomena.

7.4 Parametric Study

Results from the parametric study outlined in Chapter 6 are herein presented.

As argued in Chapter 6, the motivation to perform the parametric study was to study the effect of the moonpool width-to-vessel beam ratio, b/B, in various operational sea states. This is quantified by the standard deviation of the given response amplitude, following the procedure in Section 6.4. As argued therein, the standard deviation is a measure of the response, and these will be used interchangeably throughout this section.

Results are presented using full-scale values, with the imagined scale 1:138. The spectral peak periods, T_p, of the wave spectra are referred to in seconds, while results the spectra are plotted over use the angular frequency ω. These are also to some extent used interchangeably and compared, but always in the presence of explanatory figures.

Results for the moonpool responses are given in a body-fixed coordinate system.

Results for M0 are also included in the results, but are not further discussed due to the focus being on the b/B-ratio.

Throughout this section, experimental response spectra are for relevant cases referred to and provided in the Appendix. Presented in the all result figures of the parametric study (e.g. Figure 7.20), the remaining non-referred experimental response spectra are provided in Appendix F.1.9. The quasi-experimental RAOs in Appendix D.1.2 are applied in all experimental response spectra.

7.4.1 Piston and Sloshing Natural Periods

Table 7.5 provides full-scale values of the piston mode and selected sloshing modes for the present b/B-ratios.

Table 7.5: Piston and selected sloshing mode periods for the imagined full-scale of the present parametric geometry. The modes are according to the theory of Molin et al. (2018) in finite depth corresponding to the experimental water depth of 0.8 m (110.4 m in full-scale).

	b/B	0.25	0.375	0.50	0.625	0.75	0.875
M1	Piston mode	6.91 s	7.24 s	7.45 s	7.58 s	7.63 s	7.59 s
	1st sloshing mode	6.49 s	6.72 s	6.87 s	6.95 s	6.99 s	6.96 s
	2nd sloshing mode	5.81 s	5.94 s	6.02 s	6.06 s	6.08 s	6.07 s
	3rd sloshing mode	5.14 s	5.20 s	5.24 s	5.26 s	5.26 s	5.26 s
M2/M3	Piston mode	6.27 s	6.63 s	6.91 s	7.11 s	7.24 s	7.29 s
	1st sloshing mode	2.97 s	3.63 s	4.16 s	4.60 s	4.98 s	5.29 s

According to Table 7.5, the piston mode and first and second sloshing mode for M1 and the piston mode for M2 and M3 is expected to be sensitive to the sea states of $T_p = 6$ s and $T_p = 8$ s, as these modes coincide with or are between the respective peak periods.

7.4.2 Surge Response

The sensitivity of the surge responses of M1 and M2 to different b/B-ratios and sea states are herein compared, with an emphasis on the effect of the sloshing in M1.

Figures 7.20 and 7.21 present the results of the parametric study in surge for M1 and M2, respectively. The results for M3 are similar to M2, and are presented in Figure F.5.

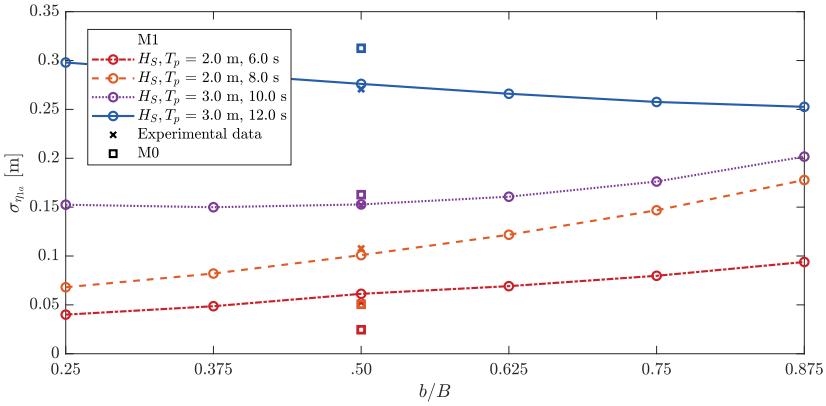

Figure 7.20: The standard deviation of the surge amplitude, $\sigma_{\eta_{1a}}$, of M1 for a set of moonpool width-to-vessel beam ratios and operational sea states. Experimental data and data for M0 is included for comparison.

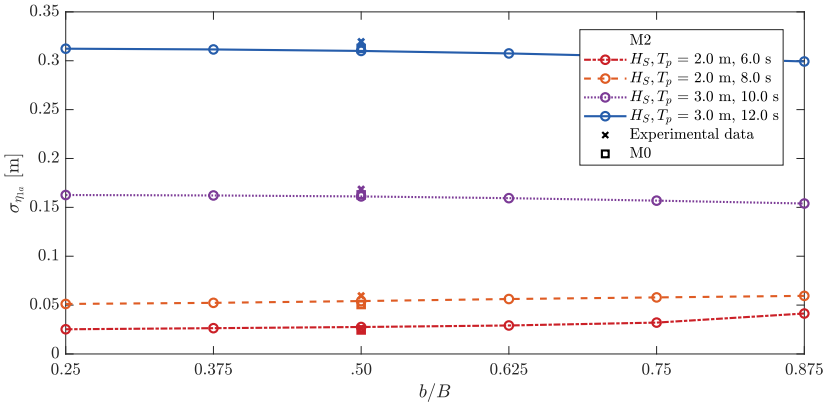

Figure 7.21: The standard deviation of the surge amplitude, $\sigma_{\eta_{1a}}$, of M2 for a set of moonpool width-to-vessel beam ratios and operational sea states. Experimental data and data for M0 is included for comparison.

Comparing Figures 7.20 and 7.21, the surge response in M1 is sensitive to both different sea states and b/B-ratios, increasing with increasing b/B-ratio for all sea states except

the largest ($H_S, T_p = 3$ m, 12 s), while M2 is unaffected by the b/B-ratio.

As argued in Section 7.3.4, the sloshing in M1 affect it's surge response, and as argued in Section 7.4.1, the sloshing modes are expected to have the largest impact during the sea states of peak periods $T_p = 6$ s and $T_p = 8$ s. This is what is seen in Figure 7.20.

Figure 7.22 present the M1 surge response spectra for $b/B = 0.25$ and $b/B = 0.875$, and shows that a larger b/B-ratio yields a larger transfer function (RAO), cf. the middle sub-figures. This explain the increase in the surge standard deviation with increasing b/B-ratio in Figure 7.20 for the sea state $H_S, T_p = 2$ m, 8 s, and expected to be similar for $H_S, T_p = 2$ m, 6 s.

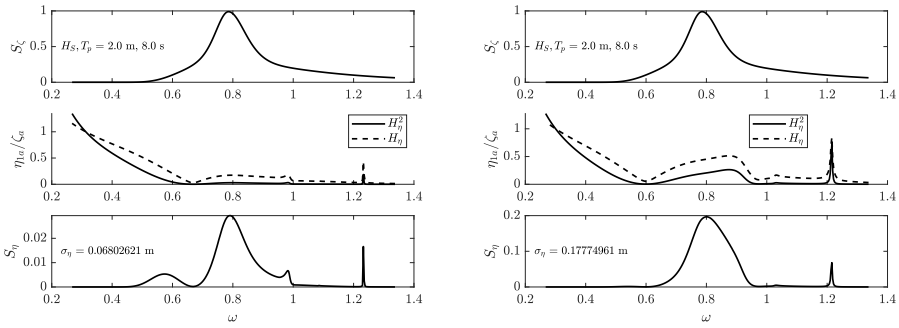

(a) $b/B = 0.25$ **(b)** $b/B = 0.875$

Figure 7.22: Response spectra for the surge response of M1 at $H_s, T_p = 2$ m, 8 s.

7.4.3 Heave Response

The sensitivity of the heave responses of M1 and M2 to different b/B-ratios and sea states is herein compared, with an emphasis on the sea state peak period and heave resonance period.

Figures 7.23 and 7.24 present the results of the parametric study in heave for M1 and M2, respectively. The results for M3 are similar to M2, and are presented in Figure F.6.

Figure 7.25 present the present wave spectra and transfer functions for selected b/B-ratios.

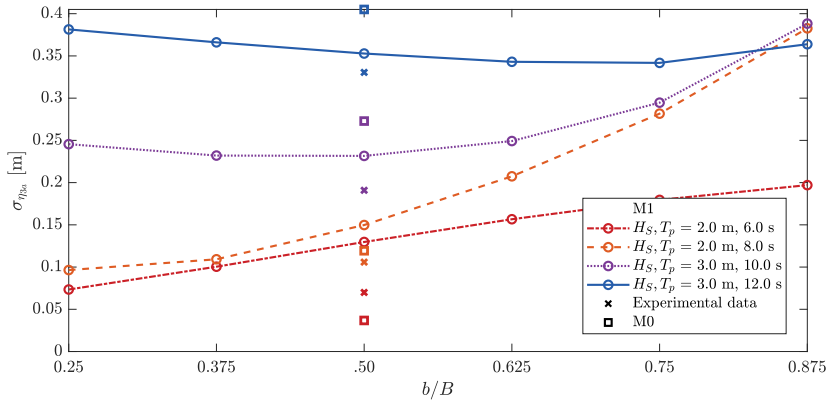

Figure 7.23: The standard deviation of the heave amplitude of M1 for a set of moonpool width-to-vessel beam ratios and operational sea states. Experimental data and data for M0 is included for comparison. The experimental response spectra are provided in Figure F.12.

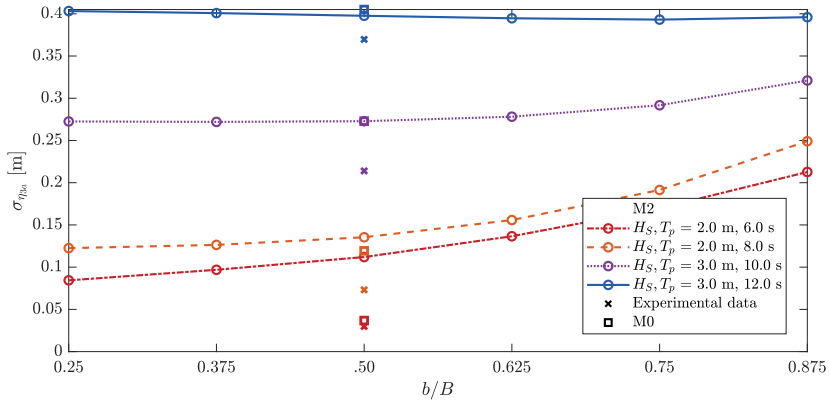

Figure 7.24: The standard deviation of the heave amplitude of M2 for a set of moonpool width-to-vessel beam ratios and operational sea states. Experimental data and data for M0 is included for comparison. The experimental response spectra are provided in Figure F.16.

As Figure 7.23 present, the heave response is especially sensitive to increasing b/B-ratio at $H_S, T_p = 2$ m, 8 s. This is evident in Figure 7.25(a), where an increase in b/B-ratio shifts (and increases) the heave resonance frequency towards lower ω, coinciding more with the peak period of the sea state $H_S, T_p = 2$ m, 8 s. This effect is to some extent also captured by the sea state $H_S, T_p = 2$ m, 6 s, hence the increase in heave response standard deviation with increasing b/B-ratio, Figure 7.23.

The increase in heave response standard deviation with increasing b/B-ratio, especially at the two sea states above, may also be described by the increase in moonpool volume-to-vessel volume. The increase in the b/B-ratio yields less vessel mass and a

smaller water-plane area (relevant for the restoring force in heave) and larger moonpool coupling with the outer fluid domain. The larger extent of coupling with the outer fluid domain yields more wave radiation and a more "disturbed" pressure field, which is integrated over the (mean) wetted surface of the vessel to obtain the forces acting on it. These factors together may thus also explain the trend (increase in heave) we see in Figures 7.23 and 7.24 for the two smallest sea states with increasing b/B-ratio.

Comparing Figures 7.25(a) and 7.25(b) , the shift in the heave resonance frequency is less for M2 than for M1 when increasing the b/B-ratio. There is still the same trend for both M1 and M2; with increasing b/B-ratio, the heave resonance period shifts towards lower ω and larger values of the transfer function (and also larger area under it's curve - suggesting a larger response). This is captured for M2 by the sea states $H_S, T_p = 2$ m, 6 s and 2 m, 8 s, as the heave standard deviation in Figure 7.24 is increasing with increasing b/B-ratio.

The behaviour of the standard deviation for the two larger sea states is largely based on the transfer functions at $\omega \leq 0.8$, as this is where the spectral peak periods are located (i.e. largest amount of energy), cf. Figure 7.25. This is why Figure 7.23 shows a large standard deviation for $H_S, T_p = 3$ m, 10 s and $b/B = 0.875$; Figure 7.25(a) shows that the wave spectrum and heave resonance frequency partly coincides. In general, all transfer functions for the different b/B-ratios coincides at low ω, thus making the response almost b/B-independent, as seen for $H_S, T_p = 3$ m, 12 s in Figures 7.23 and 7.24 .

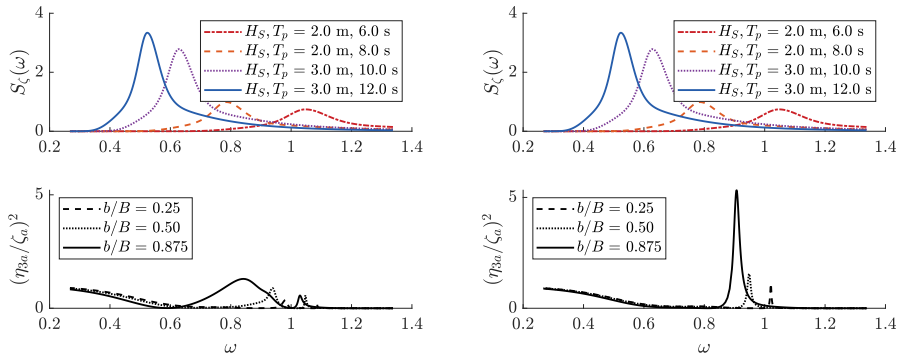

(a) M1 **(b)** M2

Figure 7.25: Wave spectra (upper) and transfer functions (the square of the RAOs) (lower) of the M1 and M2 heave response for b/B-ratios 0.25, 0.50 and 0.875. The results for M3 are similar to M2. Response spectra on the relevant sea states and b/B-ratios are provided in Appendices F.1.4 and F.1.5 for M1 and M2, respectively.

Figure 7.26 present the experimental and numerical response spectra of M1 for the heave response at the sea state $H_S, T_p = 2$ m, 8 s. The experimental transfer function, see Figure 7.26(a) is lower than the numerical, see Figure 7.26(b), which explain the difference in the heave response standard deviation in Figure 7.23 for this sea state.

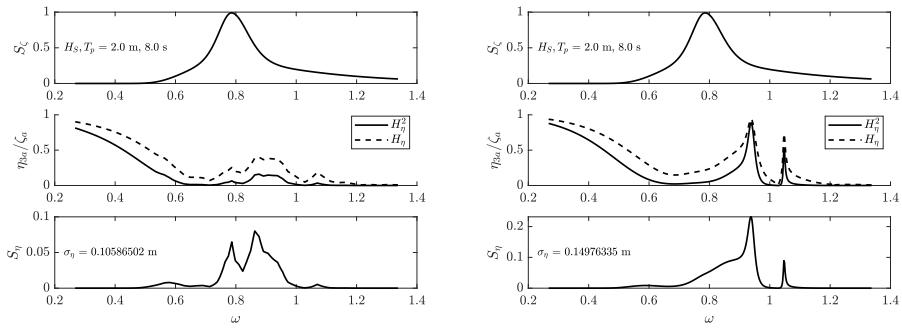

(a) Experimental

(b) Numerical

Figure 7.26: Experimental and parametric $b/B = 0.50$ for the heave response spectra for the same sea state. Experimental data present a smaller standard deviation compared to numerical simulations, partly due to flow separation experienced during experiments, a phenomenon the numerical simulations doesn't include.

7.4.4 Pitch Response

The sensitivity of the pitch response of M3 to different b/B-ratios and sea states is herein compared, with an emphasis on the sea state peak period and pitch resonance period.

Figure 7.27 present the results of the parametric study in pitch for M3. The results for M1 and M2 are similar to M3, and are presented in Figures F.1 and F.3, respectively

Figure 7.28 present the present wave spectra and transfer functions for selected b/B-ratios.

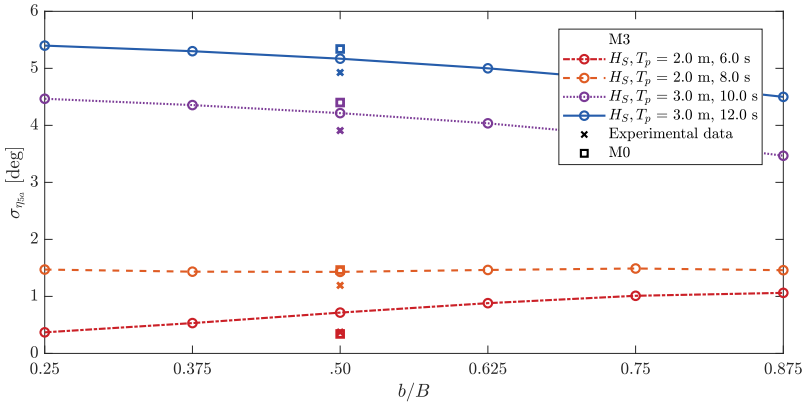

Figure 7.27: The standard deviation of the pitch amplitude, $\sigma_{\eta_{5a}}$, of M3 for a set of moonpool width-to-vessel beam ratios and operational sea states. Experimental data and data for M0 is included for comparison. The experimental response spectra are provided in Figure F.20.

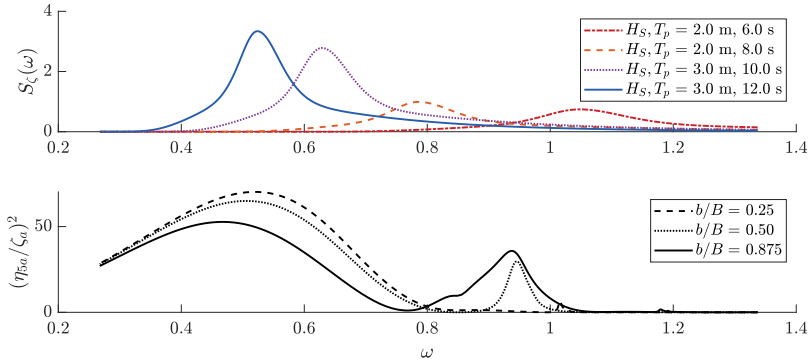

Figure 7.28: Wave spectra (upper) and transfer functions (the square of the RAOs) (lower) of the M3 pitch response for b/B-ratios 0.25, 0.50 and 0.875. Response spectra on the relevant sea states and b/B-ratios are provided in Appendix F.1.6.

As Figure 7.27 presents, the results most sensitive to increasing b/B-ratio are for the sea states H_S, T_p = 3 m, 10 s and 3 m, 12 s. This is due to their spectral peaks coinciding with the interval $\omega \leq 0.8$, where the value of the transfer functions decrease with increasing b/B-ratio, see Figure 7.28.

The shift in peak frequency towards lower ω in Figure 7.28 (for pitch) is not as prominent as in Figure 7.25 (for heave), which explain the relatively low sensitivity of pitch response with increasing b/B-ratio of the lowest two sea states in Figure 7.27. Both their spectral peak periods seems to not capture the pitch resonant behaviour at $0.8 \leq \omega \leq 1.0$. Hence, the two smallest sea states are relatively unaffected by the increasing b/B-ratio.

7.4.5 Moonpool Response

The sensitivity of the moonpool responses of M1 and M2 to different b/B-ratios and sea states is herein compared, with an emphasis on the sea state peak period and moonpool resonance periods.

M1

Figures 7.29 and 7.30 present results of the parametric study of M1 for the fore and middle moonpool response, respectively.

Figure 7.31 present the present wave spectra and transfer functions for selected b/B-ratios for the fore and middle moonpool responses.

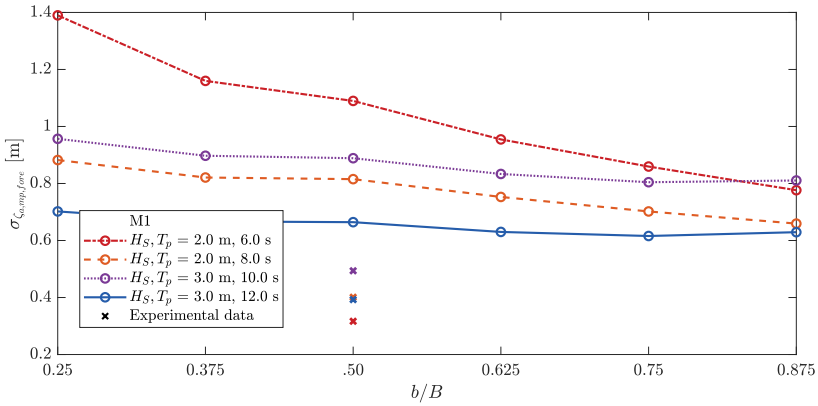

Figure 7.29: The standard deviation of the moonpool response amplitude at the fore part of the moonpool, $\sigma_{\zeta_{a,mp,fore}}$, of M1 for a set of moonpool width-to-vessel beam ratios and operational sea states. Experimental data is included for comparison. The results are similar for the aft part of the moonpool, presented in Figure F.2. The experimental response spectra are provided in Figure F.24.

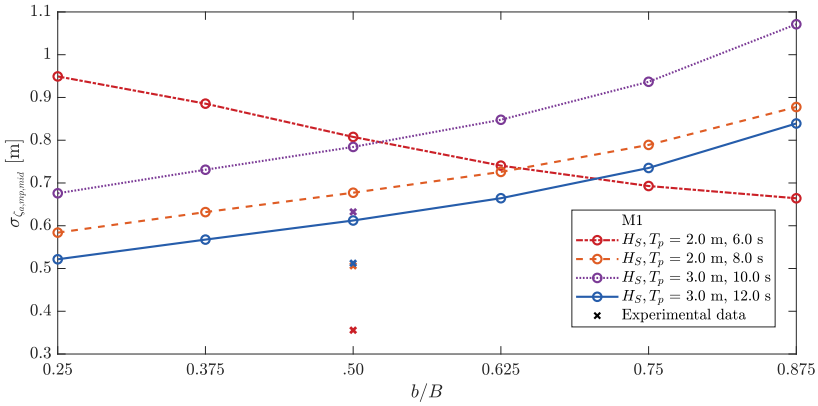

Figure 7.30: The standard deviation of the moonpool response amplitude at the middle of the moonpool, $\sigma_{\zeta_{a,mp,mid}}$, of M1 for a set of moonpool width-to-vessel beam ratios and operational sea states. Experimental data is included for comparison. The experimental response spectra are provided in Figure F.28.

In the fore part of the moonpool, Figure 7.29, the results in sea state $H_S, T_p = 2$ m, 6 s are decreasing the most with increasing b/B-ratio. Figure 7.31(a) shows a decrease in the response peak frequency (and also the area under the curve) for increasing b/B-ratio, coinciding with the spectral period for this sea state. At low ω, the transfer functions for the two b/B-ratios are approximately the same, and the response for the three largest sea states are thus dominated by the decrease in the response peak frequency at $0.9 \lesssim \omega \lesssim 1.25$, explaining why these results also decrease in Figure 7.29.

In the middle of the moonpool, Figure 7.30, the trend for $H_S, T_p = 2$ m, 6 s is similar to as argued above; the result is dominated by the decrease in response peak frequency. Figure 7.31(b) shows a larger increase in the transfer function with increasing b/B-ratio for $\omega \lesssim 0.9$. Since this increase is more prominent than what is seen in Figure 7.31(a), the results at the three largest sea states all increase with increasing b/B-ratio, as their spectral peak periods "capture" the increase in the transfer functions at $\omega \lesssim 0.9$.

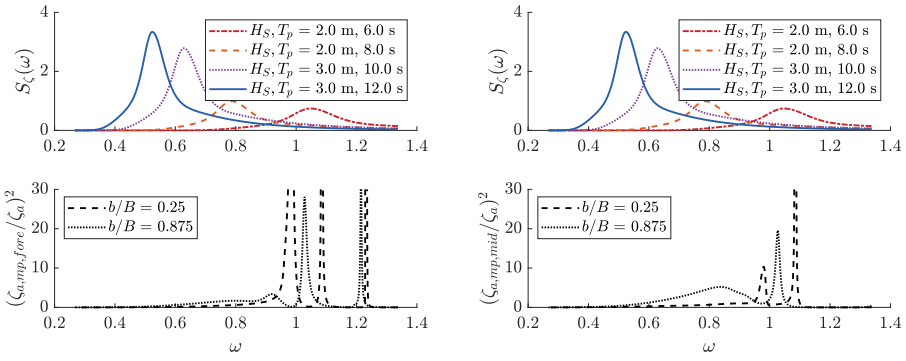

(a) Fore **(b)** Middle

Figure 7.31: Wave spectra (upper) and transfer functions (the square of the RAOs) (lower) at the fore and in the middle of the moonpool for M1 for b/B-ratios 0.25 and 0.875. Response spectra on the relevant sea states and b/B-ratios are provided in Appendices F.1.7 and F.1.8 for the fore and middle part of the moonpool, respectively.

M2

Figure 7.32 present results of the parametric study of M2 for the fore moonpool response, respectively. The result in the aft moonpool is similar, and is presented in Figure F.4.

Figure 7.33 present the response spectra of the fore moonpool for selected b/B-ratios in the sea state $H_S, T_p = 2$ m, 6 s.

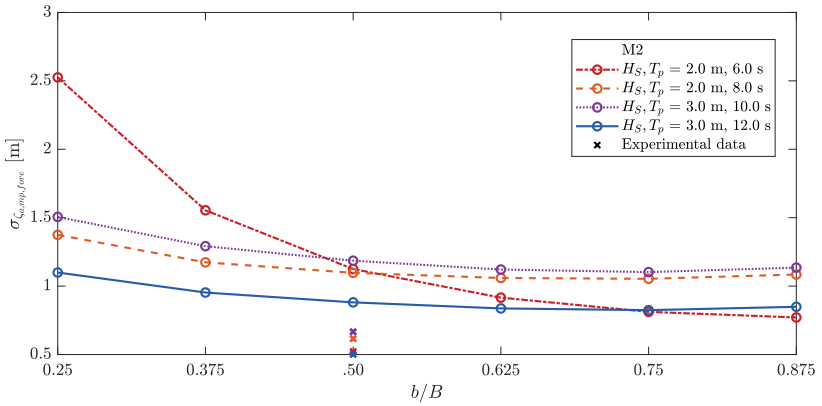

Figure 7.32: The standard deviation of the moonpool response amplitude at the fore moonpool, $\sigma_{\zeta_{a,mp,fore}}$, of M2 for a set of moonpool width-to-vessel beam ratios and operational sea states. Experimental data is included for comparison.

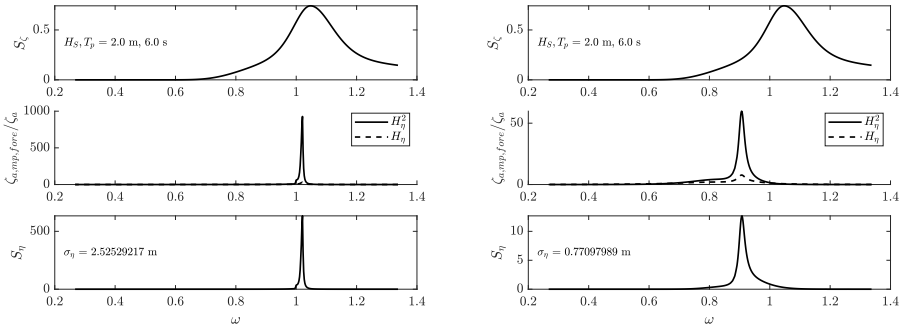

(a) $b/B = 0.25$ **(b)** $b/B = 0.87$

Figure 7.33: Response spectra for the fore moonpool response of M2 at H_s, T_p =2 m, 6 s.

From Figure 7.32, the sea state $H_S, T_p = 2$ m, 6 s is the sea state which affect the moonpool response the most, argued in Section 7.4.1, as this is the spectral peak period closest to the piston mode natural frequencies. Both Table 7.5 and Figure 7.33 indicate a decrease in the piston mode natural frequency with increasing b/B-ratio, thus a shift of the peak frequency towards lower ω. Also, the value (and area under the curve) of the transfer functions in Figure 7.33 decrease with increasing b/B-ratio, indicating a lower response in the fore moonpool, which is confirmed by Figure 7.32.

The increase in the b/B-ratio means that the moonpool opening is closer to the outer fluid domain, and thus coupling between the moonpool response and the outer fluid domain may be a reason to why we see the decrease in the fore moonpool response for $H_S, T_p =$ 2 m, 6 s. The larger extent of the coupling with the outer fluid domain for increasing b/B-ratios makes wave radiation more prominent; working as a dampening mechanism on the

moonpool response, explaining the decrease we see of the moonpool response in this sea state for increasing b/B-ratio.

In Figure 7.32, there is a large difference between the numerical and experimental results, mainly caused by the flow separation at the moonpool inlet as argued in Section 7.4.4. Figure 7.34 present the experimental and numerical response spectra at $b/B = 0.50$ for $H_S, T_p = 2$ m, 8 s. Comparing the values of the transfer functions, we can conclude that flow separation is indeed an important contributor on the dampening mechanism for the moonpool piston modes, in this case for the fore moonpool in M2.

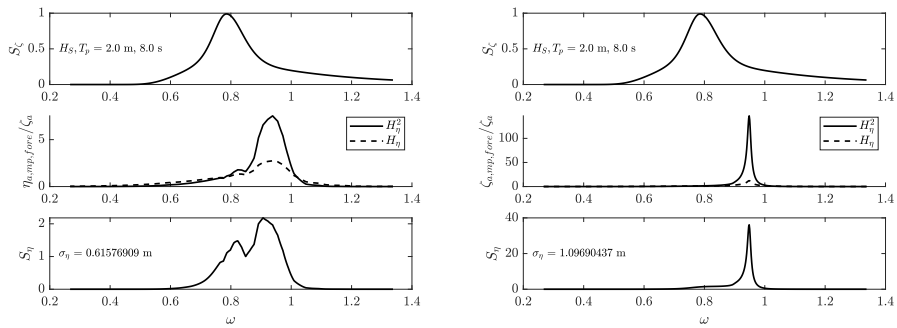

(a) Experimental **(b)** Numerical

Figure 7.34: Experimental and numerical response spectra for the fore moonpool response of M2 at H_s, T_p =2 m, 8 s. Note the large difference in the transfer function (middle sub-figures) between the experimental and numerical results.

M3

The results of the fore moonpool for M3, presented in Figure F.7, are similar to the one of M2 covered above, and won't be covered here. We turn the attention towards the observed moonpool cancellation described in Section 7.3.6.

Figure 7.35 present results of the parametric study of the aft moonpool of M3. Similar results are obtained at the middle moonpool, which is presented in Figure F.8.

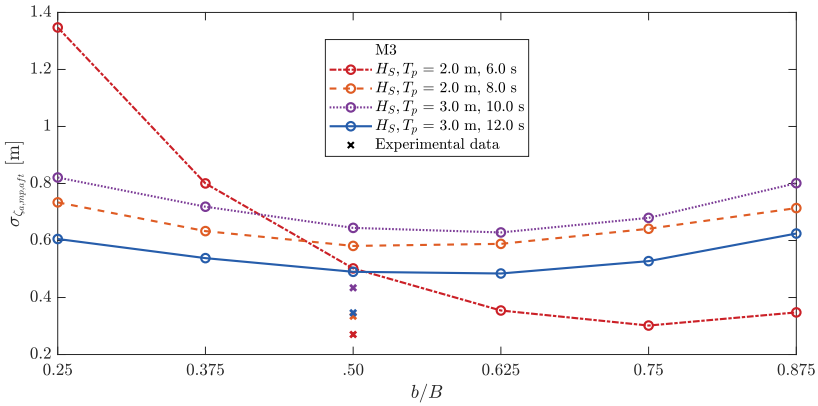

Figure 7.35: The standard deviation of the moonpool response amplitude at the aft moonpool, $\sigma_{\zeta_{a,mp,aft}}$, of M3 for a set of moonpool width-to-vessel beam ratios and operational sea states. Experimental data is included for comparison.

In Figure 7.35, similar mechanisms as described for the fore moonpool response of M2 apply: the sea state $H_S, T_p = 2$ m, 6 s is affecting the piston-mode-only described moonpool response in the aft moonpool of M3. With the observed cancellation present, the decrease in moonpool response is larger in Figure 7.35 (aft moonpool of M3) compared to Figure 7.35 (fore moonpool of M2) for the sea state $H_S, T_p = 2$ m, 6 s, which is the sea state exciting the piston mode the most (compared with the chosen sea states).

Chapter 8

Summarising Conclusion and Further Work

In the present work, the coupled moonpool and vessel responses are investigated by various means. A vessel of three different moonpool configurations is designed; one large moonpool and two and three smaller, in this thesis referred to as M1, M2 and M3. A relevant theoretical background is provided, and an analytical model to predict the piston-mode periods on the two- and three-moonpool configurations is developed. Experiments on all three configurations are carried out in head sea and freely-floating conditions. Numerical simulations assuming linearized potential flow theory are applied both on the analytical and the experimental results. A parametric study on the sensitivity of the rigid body motions and moonpool responses with varying moonpool width-to-vessel beam (b/B) ratio in operational conditions is conducted. The parametric study is done using numerical simulations and is coupled with experimental results, where applicable.

8.1 Summarising Conclusion

Overall, good satisfaction between experiments and numerical simulations are found. Discrepancies are mainly due to viscous effects and the tank width. The latter implies that some responses, for example the heave response of M3, have not reached steady-state conditions before reflective waves is expected to interfere with the model. Good concordance is also found with published literature on geometry similar to M1. Discrepancies, when compared with numerical and theoretical models, indicate that hydrodynamic interaction between the moonpool and vessel (herein coupled) responses are present and important.

Compared to M2 and M3, the presence of sloshing in M1 is a main contributor to a almost twice as large surge response in proximity of the sloshing mode natural periods, as no sloshing is observed in M2 and M3.

For M1, the piston mode and first longitudinal sloshing mode seem to appear as a joint mode. In M2 and M3, only the piston mode is found to be present, and observed relative phase differences between these moonpool responses seems to be a main candidate to explain an observed cancellation in heave for M2 and M3 around the piston mode period. This cancellation is not as prominent for M1, and the larger extent of wave radiation

damping, due to a larger moonpool-and-outer fluid domain coupling, is believed to be the reason.

The herein-developed analytical model provide fair agreement with numerical results, and work as a first verification, given it's assumptions. The model predict the moonpools to be in-phase and 180 degrees out-of-phase for the M2 forced heave and pitch motions, respectively. For M3, the model yields the same result in pitch, but the forced heave motion contain two distinct modes: one where all three moonpool are in-phase and one where the middle moonpool is 180 degrees out-of-phase with the outer two. This agree with the experimentally observed relative phase difference between moonpool responses in M3.

In the parametric study, findings show sensitivity of the M1 surge response with varying b/B-ratios in sea states that is expected to excite sloshing modes. M2 and M3 are practically unaffected, as no sloshing is present. The pitch response of all three configurations is relatively unaffected in all sea states.

The coupling with the outer fluid domain, more prominent with increasing b/B-ratio, is found to be important, due to increased wave radiation damping. For M1 in particular, the heave response is increased with increasing b/B-ratio in sea states whose peak period is in proximity of the heave resonance period. The increase in coupling between the moonpools and the outer fluid domain is also found important for M2 and M3, whose moonpool response decrease with increased coupling, even in sea states that are expected to excite the moonpool piston mode.

Comparison of results from the parametric study and experimental results indicate that viscous damping is important, both for rigid-body motions and moonpool response.

8.2 Further Work

In this thesis, a large amount of work is spent to investigate various aspects of coupled moonpool and vessel responses. Naturally not being able to investigate findings, found specifically interesting, in a more in-depth manner due to the extent of the work and time frame, proposals on further studies follows.

As mentioned, the tank width limited the obtainable results to some extent. Further work could consist of conducting experiments in an environment representing the open sea condition better, to further investigate interesting findings from this thesis, for example the moonpool response cancellation observed in M3.

Experiments should also be conducted on the b/B-ratio to further investigate the effect of the coupling with the outer fluid domain. The heave response would also be interesting to conduct an experimental parameter study upon.

The analytical model should be further developed to account for finite spatial dimension of both the barge and water depth. In this relation, forced heave and pitch experiments could be conducted to further verify the herein- or then-developed model.

The as-of-now newest version of WAMIT, version 7.3, include the possibility to analyse bodies where two parallel walls are present - a utility that could be useful wrt. the experiments carried out in the present thesis. WAMIT now also include the possibility to represent damping on the free-surface, a feature that should be investigated in any further work where WAMIT is used in relation to moonpools.

Bibliography

Albers, A. B. (1984). "The Water Motions In a Moonpool". In: *Ocean Engineering* 11.6, pp. 557–579.

DNV GL (2018). *DNVGL-CG-0130 Wave loads*. DNV GL. URL: https://rules.dnvgl.com/docs/pdf/DNVGL/CG/2018-01/DNVGL-CG-0130.pdf.

Faltinsen, O. M. (1990). *Sea loads On Ships and Offshore Structures*. Cambridge Ocean Technology Series. Cambridge: Cambridge University Press. ISBN: 0-521-37285-2.

— (2006). *Hydrodynamics of High-Speed Marine Vehicles*. Cambridge: Cambridge University Press. ISBN: 978-0-521-84568-7. DOI: 10.1017/CBO9780511546068. URL: https://www.cambridge.org/core/books/hydrodynamics-of-highspeed-marine-vehicles/EFAC95328551E361A7DD04464F296C41 (visited on 06/08/2020).

Faltinsen, O. M., O. F. Rognebakke, and A. N. Timokha (2007). "Two-dimensional resonant piston-like sloshing in a moonpool". In: *Journal of Fluid Mechanics* 575, pp. 359–397. ISSN: 0022-1120, 1469-7645. DOI: 10.1017/S002211200600440X. URL: https://www.cambridge.org/core/product/identifier/S002211200600440X/type/journal_article (visited on 09/18/2019).

Faltinsen, O. M. and A. N. Timokha (2009). *Sloshing*. Cambridge: University Press. xxvii+577. ISBN: 978-0-521-88111-1.

— (2015). "On damping of two-dimensional piston-mode sloshing in a rectangular moonpool under forced heave motions". In: *Journal of Fluid Mechanics* 772, R1. ISSN: 0022-1120, 1469-7645. DOI: 10.1017/jfm.2015.234. URL: https://www.cambridge.org/core/product/identifier/S0022112015002347/type/journal_article (visited on 12/17/2019).

Fredriksen, A. G., T. Kristiansen, and O. M. Faltinsen (2015). "Wave-induced response of a floating two-dimensional body with a moonpool". In: *Philosophical Transactions of the Royal Society A: Mathematical, Physical and Engineering Sciences* 373.2033, p. 20140109. ISSN: 1364-503X, 1471-2962. DOI: 10.1098/rsta.2014.0109. URL: https://royalsocietypublishing.org/doi/10.1098/rsta.2014.0109 (visited on 09/05/2019).

Hughes, S. A. (1993). *Physical Models and Laboratory Techniques in Coastal Engineering*. Vol. 7. 24 vols. Advanced Series on Ocean Engineering. Singapore: World Scientific Publishing Co. Pte. Ltd. ISBN: 981-02-1540-1.

Ikeda, Y., T. Fujiwara, and T. Katayama (1993). "Roll Damping of a Sharp-Cornered Barge And Roll Control By a New-Type Stabilizer". In: The Third International Offshore and Polar Engineering Conference. International Society of Offshore and Polar Engineers. URL: https://www.onepetro.org/conference-paper/ISOPE-I-93-305 (visited on 06/04/2020).

Kildal, J. Ravndal (2019). *Experimental and Numerical Investigation of Coupled Vessel and Moonpool Responses*. Pre-project. NTNU.

Lee, C. and J. N. Newman (2006). *WAMIT User Manual, Version 6.4*. Version: 6.41. URL: https://www.wamit.com/manual6.htm.

Miles, J. (2002). "On slow oscillations in coupled wells". In: *Journal of Fluid Mechanics* 455, pp. 283–287. ISSN: 0022-1120, 1469-7645. DOI: 10.1017/S0022112001007212. URL: https://www.cambridge.org/core/product/identifier/S0022112001007212/type/journal_article (visited on 01/08/2020).

Molin, B. (2001). "On the piston and sloshing modes in moonpools". In: *Journal of Fluid Mechanics* 430, pp. 27–50. ISSN: 00221120. DOI: 10.1017/S0022112000002871. URL: http://www.journals.cambridge.org/abstract_S0022112000002871 (visited on 09/05/2019).

Molin, B. et al. (2018). "On natural modes in moonpools and gaps in finite depth". In: *Journal of Fluid Mechanics* 840, pp. 530–554. ISSN: 0022-1120, 1469-7645. DOI: 10.1017/jfm.2018.69. URL: https://www.cambridge.org/core/product/identifier/S0022112018000691/type/journal_article (visited on 10/12/2019).

Myshkis, A. D. et al. (1987). "Low-Gravity Fluid Mechanics". In: p. 218. URL: https://ui.adsabs.harvard.edu/abs/1987lgfm.book.....M/abstract (visited on 11/11/2019).

Newman, J. N. (2003). "Low-frequency resonance of moonpools". In: *18th Workshop on Water Waves and Floating Bodies – Le Croisic, France*, p. 5.

Ravinthrakumar, S. (2020). "Numerical and Experimental Studies of Resonant Flow in Moonpools in Operational Conditions". Doctoral Thesis. Trondheim, Norway: NTNU. 296 pp.

Ravinthrakumar, S., T. Kristiansen, and B. Ommani (2019). "On the hydrodynamic interaction between ship and free-surface motions on vessels with moonpools". In: *Proceedings of the ASME 2019 38th International Conference on Ocean, Offshore and Arctic Engineering*. OMAE2019-95932, p. 9.

Ravinthrakumar, S. et al. (2020). "Coupled vessel and moonpool responses in regular and irregular waves". In: *Applied Ocean Research* 96, p. 102010. ISSN: 01411187. DOI: 10.1016/j.apor.2019.102010. URL: https://linkinghub.elsevier.com/retrieve/pii/S0141118719308132 (visited on 02/18/2020).

Reiersen, L. M. Utnes (2016). "Investigation of Moonpool Resonance as Vessel Damping Device". In: p. 262.

Reiersen, L. M. Utnes et al. (2018). "Investigation of moonpools as pitch motion reducing device". In: p. 27.

Vries, I. de et al. (2014). “Design Aspects of Large Diameter Turret Systems: Part 1 — Moonpool Piston Mode”. In: *Volume 1B: Offshore Technology*. ASME 2014 33rd International Conference on Ocean, Offshore and Arctic Engineering. San Francisco, California, USA: American Society of Mechanical Engineers, V01BT01A043. ISBN: 978-0-7918-4538-7. DOI: 10.1115/OMAE2014-24531. URL: https://asmedigitalcollection.asme.org/OMAE/proceedings/OMAE2014/45387/San%20Francisco,%20California,%20USA/278635 (visited on 05/19/2020).

Appendix

Appendix A: Surface Tension on Propagating Waves

A.1.1 Surface Tension on Propagating Waves

The surface tension's effect on the free surface is considered for two-dimensional propagating waves. It can be shown by the use of the free surface boundary condition (Faltinsen et al., 2009), that

$$\omega^2 = kg + k^3 T_s/\rho \tag{A.1.1}$$

where ω is the wave frequency, $k = \frac{2\pi}{\lambda}$ the wave number with λ the wave length, T_s the surface tension and ρ the water density.

Now, taking the phase speed of a dispersive wave, $c_p = \frac{\omega}{k}$ and inserting the relation above, one obtain

$$c_{p,st} = \frac{\lambda}{2\pi}\sqrt{g\frac{2\pi}{\lambda} + \left(\frac{2\pi}{\lambda}\right)^3 \frac{T_s}{\rho}} \tag{A.1.2}$$

where the subscript st denotes surface tension affected waves. The phase speed of a dispersive wave (where surface tension is neglected) is

$$c_{p,dw} = \frac{\omega}{k} = \frac{\lambda}{2\pi}\sqrt{\frac{2\pi}{\lambda}g} \tag{A.1.3}$$

where the subscript dw denotes regular waves in deep water.

Now, plotting the relation between the two against the wave length λ, we get

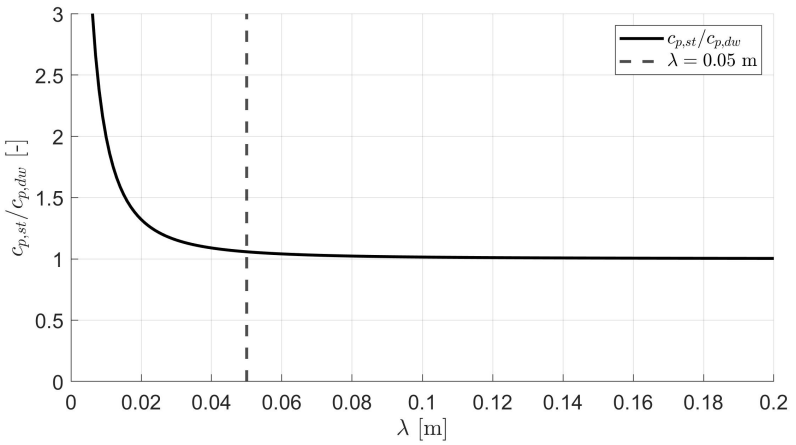

which indicates that surface tension can be neglected for wave lengths $\lambda \gtrsim 0.05$ m.

Appendix B: Analytical Model

B.1.1 Result from Molin (2001)

The integral

$$I_{0000} = \iiint\!\!\iint_{S_n} \frac{1}{\sqrt{(x-\zeta)^2 + (y-\eta)^2}} \mathrm{d}S_n \tag{B.1.4}$$

needs to be evaluated. For a moonpool of length l and width b, spanning the domain S_n, the solution is

$$I_{0000} = 2b^2 l \sinh^{-1}\left(\frac{l}{b}\right) + 2bl^2 \sinh^{-1}\left(\frac{b}{l}\right) + \frac{2}{3}\left(b^3 + l^3\right) - \frac{2}{3}\left(b^2 + l^2\right)^{3/2} \tag{B.1.5}$$

For a thorough deduction, please refer to Appendix A.2.1 in (Molin, 2001).

B.1.2 Solution of the Three-Moonpool Configuration

Following the procedure in Section 3.5, we want to find the non-trivial solutions of the equation system

$$\begin{bmatrix} \theta & B_1 & B_2 \\ B_1 & \theta & B1 \\ B_2 & B_1 & \theta \end{bmatrix} \boldsymbol{w_n} = 0, \qquad \theta \equiv \left(d - \frac{g}{\omega_{0,n}^2} + A\right) \tag{B.1.6}$$

The determinant of the matrix is

$$\det \begin{bmatrix} \theta & B_1 & B_2 \\ B_1 & \theta & B1 \\ B_2 & B_1 & \theta \end{bmatrix} = 2B_1^2 B_2 - 2B_1^2\theta - B_2^2\theta + \theta^3 \tag{B.1.7}$$

which has the roots $\boldsymbol{\lambda}$, given by

$$\lambda_1 = B_2 \tag{B.1.8}$$

$$\lambda_2 = \frac{1}{2}\left(-B_2 + \sqrt{8B_1^2 + B_2^2}\right) \tag{B.1.9}$$

$$\lambda_3 = \frac{1}{2}\left(-B_2 - \sqrt{8B_1^2 + B_2^2}\right) \tag{B.1.10}$$

To find $\boldsymbol{w}$, we solve

$$\begin{bmatrix} \lambda_i & B_1 & B_2 \\ B_1 & \lambda_i & B1 \\ B_2 & B_1 & \lambda_i \end{bmatrix} \begin{bmatrix} w_1 \\ w_2 \\ w_3 \end{bmatrix} = 0, \qquad i = 1, 2, 3, \tag{B.1.11}$$

which, for each root λ_i, is

$$\lambda_1 : \qquad \boldsymbol{w} = \begin{bmatrix} -1 \\ 0 \\ 1 \end{bmatrix} \tag{B.1.12}$$

$$\lambda_2 : \qquad \boldsymbol{w} = \begin{bmatrix} \frac{1}{4B_1}\left(B_2 - \sqrt{8B_1^2 + B_2^2}\right) \\ 1 \\ \frac{1}{4B_1}\left(B_2 - \sqrt{8B_1^2 + B_2^2}\right) \end{bmatrix} = \begin{bmatrix} -0.5931 \\ 1 \\ -0.5931 \end{bmatrix} \tag{B.1.13}$$

$$\lambda_3 : \qquad \boldsymbol{w} = \begin{bmatrix} \frac{1}{4B_1}\left(B_2 + \sqrt{8B_1^2 + B_2^2}\right) \\ 1 \\ \frac{1}{4B_1}\left(B_2 + \sqrt{8B_1^2 + B_2^2}\right) \end{bmatrix} = \begin{bmatrix} 0.8431 \\ 1 \\ 0.8431 \end{bmatrix} \tag{B.1.14}$$

where the geometry of the problem, $b = 0.10$ and $c = 0.40$ is applied. Remembering the geometry of each moonpool spaced apart $c/2$, the cross terms, Equation (3.11), becomes

$$B_1 = \frac{b^2}{2\pi\frac{c}{2}} = \frac{b^2}{\pi c}$$
$$B_2 = \frac{b^2}{2\pi c},$$

implying that the cross-moonpool couplings are stronger for adjacent moonpools, denoted by B_1, which intuitively is physically correct.

B.1.3 WAMIT Result for the Narrow Two-Moonpool Configuration

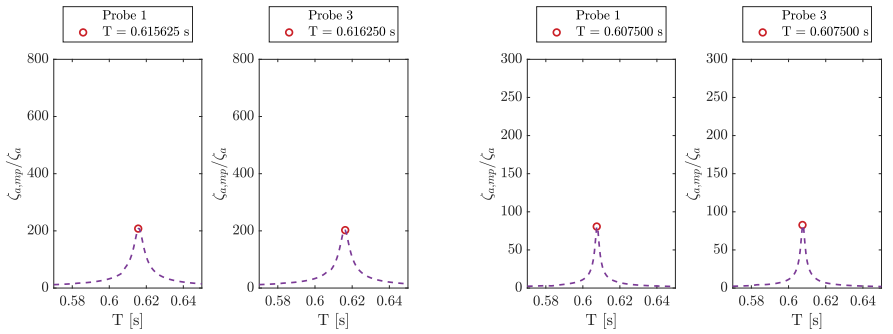

(a) Forced heave **(b)** Forced pitch

Figure B.1: WAMIT results for the analytical two-moonpool configuration for a width of 0.5 m. Numerical wave probe 1 is placed at $(x, y, z) = (0.2, 0, 0)$ and probe 3 at $(x, y, z) = (-0.2, 0, 0)$, cf. Figure 3.3. The vertical axes shows body-fixed RAO's at the numerical wave probes, while the horizontal axes shows the period of oscillation.

Appendix C: Experiments

C.1.1 Model Properties

Table C.1: Main properties of the vessel and different moonpool configurations. The calculations are done in the CAD software Rhino and in the Excel program *elmass*, written at MARINTEK. The center of the coordinate system is placed at the mean waterline a distance $L_{pp}/2$ from the stern along the center line.

		Model scale	Full scale
Length	(L_{pp})	1.0 m	138 m
Beam	(B)	0.2 m	27.6 m
Draft	(D)	0.05 m	6.9 m
		M1	
Moonpool length	(l)	0.5 m	69 m
Moonpool width	(b)	0.1 m	13.8 m
Moonpool center	((c_x, c_y, c_z))	(-0.0375 m, 0 m, 0 m)	(-5.175 m, 0 m, 0 m)
Vessel mass	(m)	5.839 kg	15345.3 t
Center of gyration	(COG)	(-0.018 m, 0 m, 0.023 m)	(-2.5 m, 0 m, 3.2 m)
Radius of gyration	((r_{44}, r_{55}, r_{66}))	(0.088 m, 0.280 m, 0.278 m)	(12.1 m, 38.6 m, 38.4 m)
		M2	
Moonpool length	(l)	0.1 m	13.8 m
Moonpool width	(b)	0.1 m	13.8 m
Fore moonpool center	((c_x, c_y, c_z))	(0.1625 m, 0 m, 0 m)	(22.425 m, 0 m, 0 m)
Aft moonpool center	((c_x, c_y, c_z))	(-0.2375 m, 0 m, 0 m)	(-32.775 m, 0 m, 0 m)
Vessel mass	(m)	7.339 kg	19287.4 t
Center of gyration	(COG)	(-0.022 m, 0 m, 0.020 m)	(-3.0 m, 0 m, 2.8 m)
Radius of gyration	((r_{44}, r_{55}, r_{66}))	(0.082 m, 0.254 m, 0.250 m)	(11.3 m, 35.0 m, 34.5 m)
		M3	
Moonpool length	(l)	0.1 m	13.8 m
Moonpool width	(b)	0.1 m	13.8 m
Fore moonpool center	((c_x, c_y, c_z))	(0.1625 m, 0 m, 0 m)	(22.425 m, 0 m, 0 m)
Middle moonpool center	((c_x, c_y, c_z))	(-0.0375 m, 0 m, 0 m)	(-5.175 m, 0 m, 0 m)
Aft moonpool center	((c_x, c_y, c_z))	(-0.2375 m, 0 m, 0 m)	(-32.775 m, 0 m, 0 m)
Vessel mass	(m)	6.839 kg	17973.4 t
Center of gyration	(COG)	(-0.021 m, 0 m, 0.022 m)	(-2.9 m, 0 m, 3.0 m)
Radius of gyration	((r_{44}, r_{55}, r_{66}))	(0.084 m, 0.262 m, 0.260 m)	(11.6 m, 36.1 m, 35.9 m)

C.1.2 Wave Probe Layout

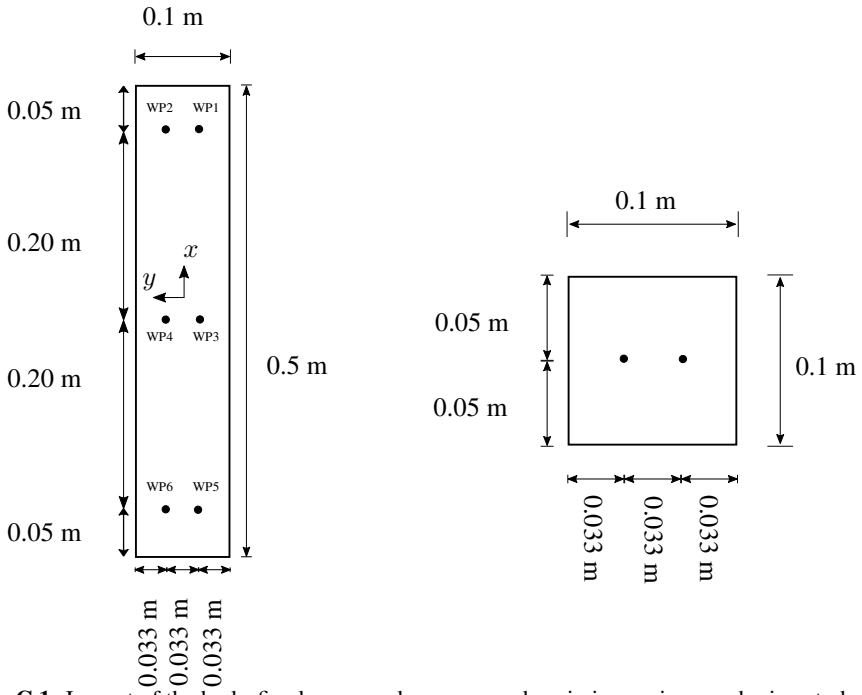

Figure C.1: Layout of the body-fixed wave probes wave probes, in increasing numbering starboard to port and from fore to aft. The probes are centred in the square moonpools, see Table C.1.

C.1.3 Natural Period in Surge

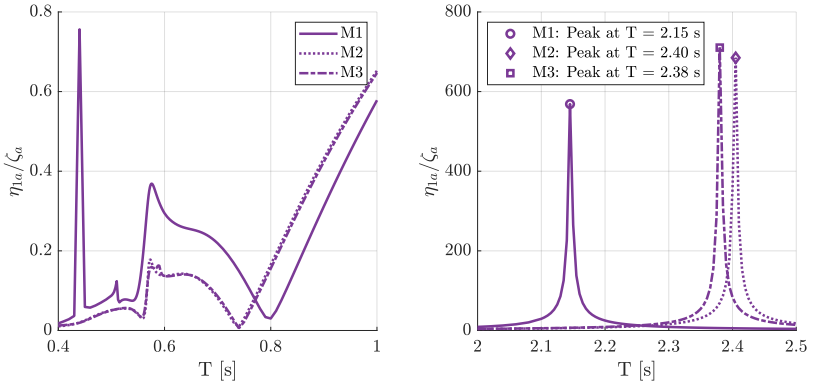

Figure C.2: The natural period in surge for M1, M2 and M3, as predicted by WAMIT.

C.1.4 Decay Test Time Series

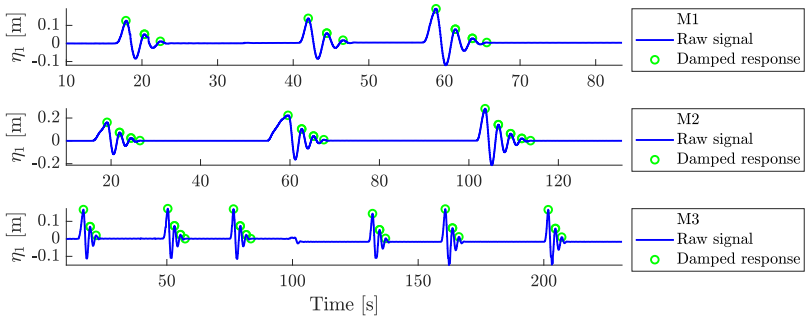

Figure C.3: Surge time series for the decay test

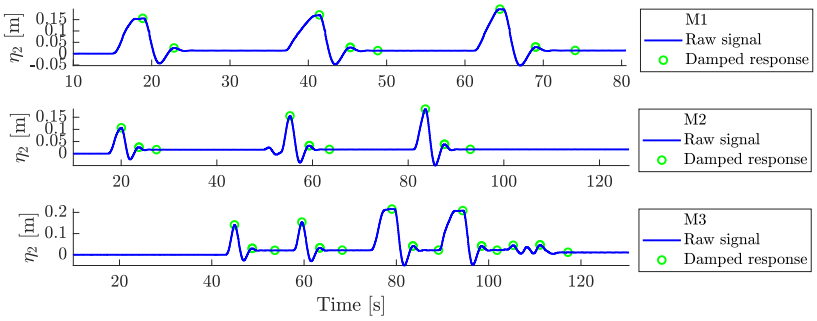

Figure C.4: Sway time series for the decay test

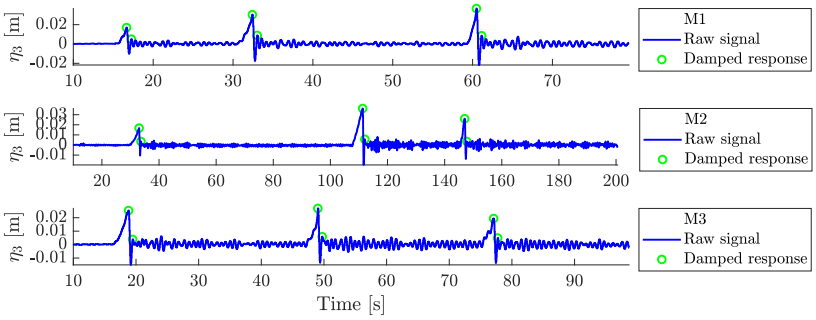

Figure C.5: Heave time series for the decay test

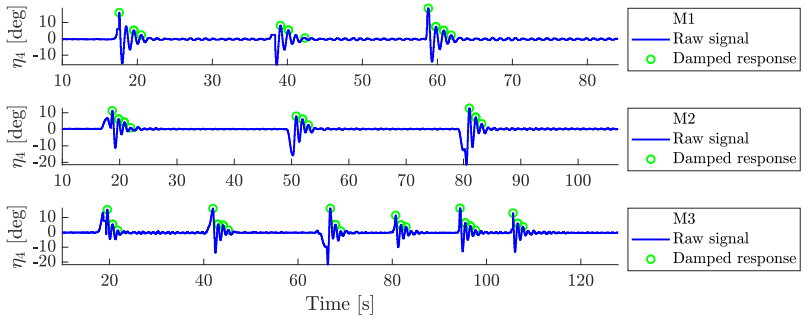

Figure C.6: Roll time series for the decay test

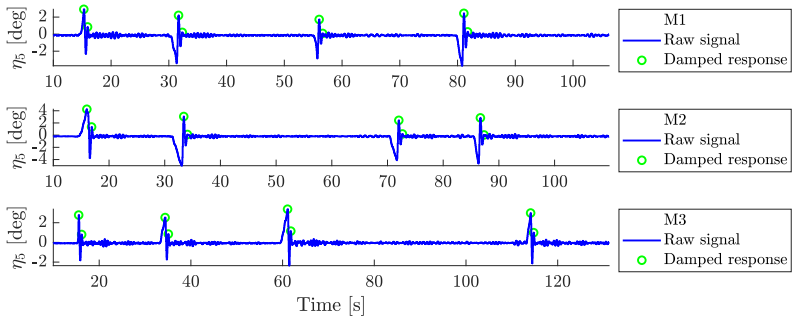

Figure C.7: Pitch time series for the decay test

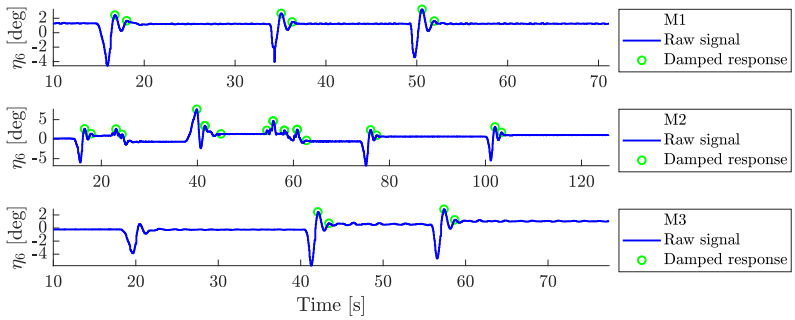

Figure C.8: Yaw time series for the decay test. The irregularities for M2 are not used in the post-processing.

C.1.5 Decay Test Coupled Modes for M1

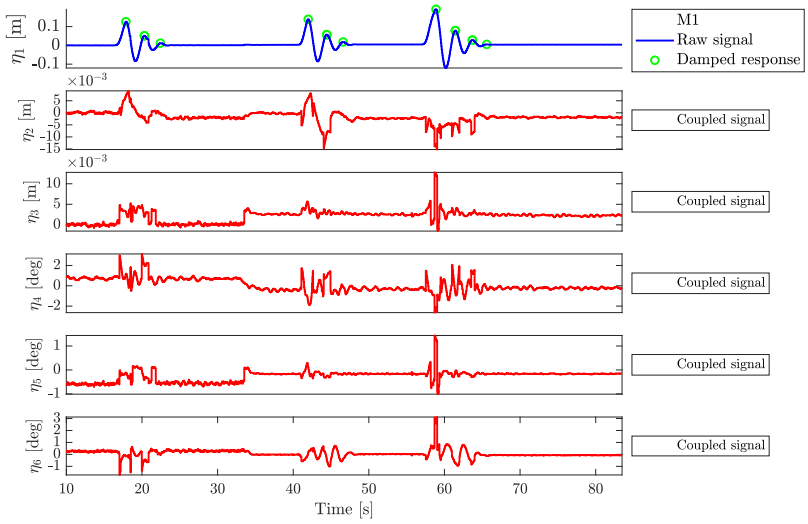

Figure C.9: Surge time series for the M1 decay test (upper). The lower sub-figures show the coupling between modes experienced in the given decay test.

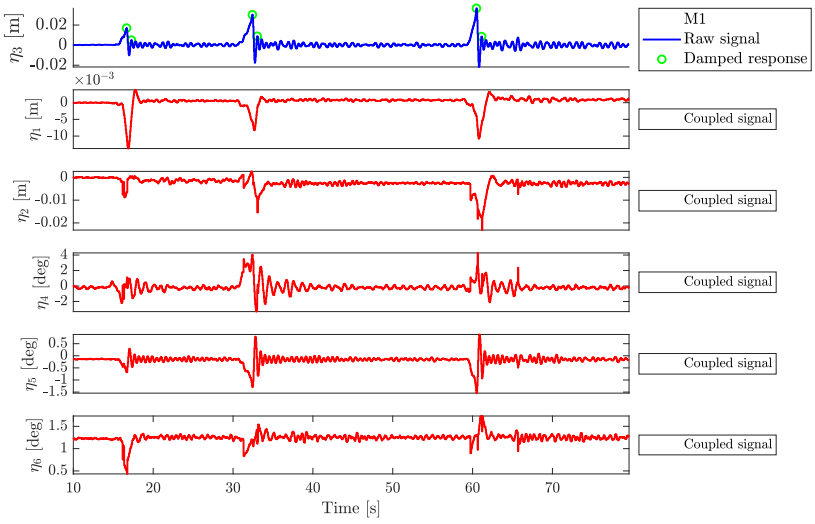

Figure C.10: Heave time series for the M1 decay test (upper). The lower sub-figures show the coupling between modes experienced in the given decay test.

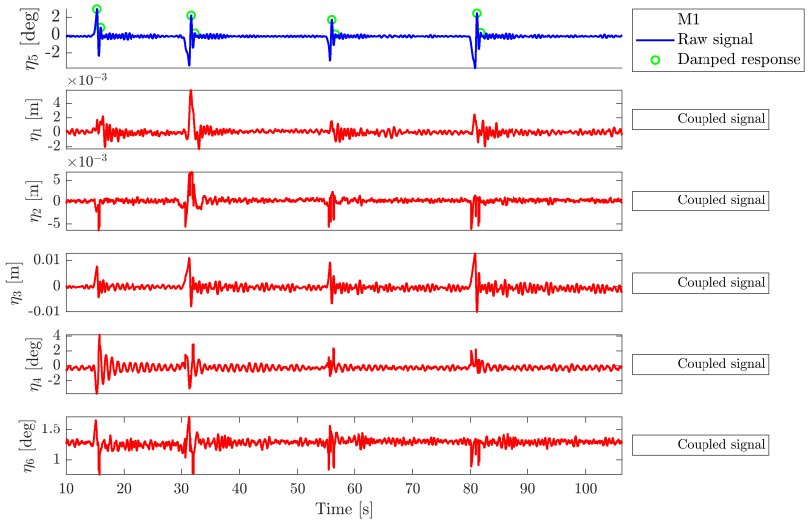

Figure C.11: Pitch time series for the M1 decay test (upper). The lower sub-figures show the coupling between modes experienced in the given decay test.

C.1.6 Non-Uniform Time Series

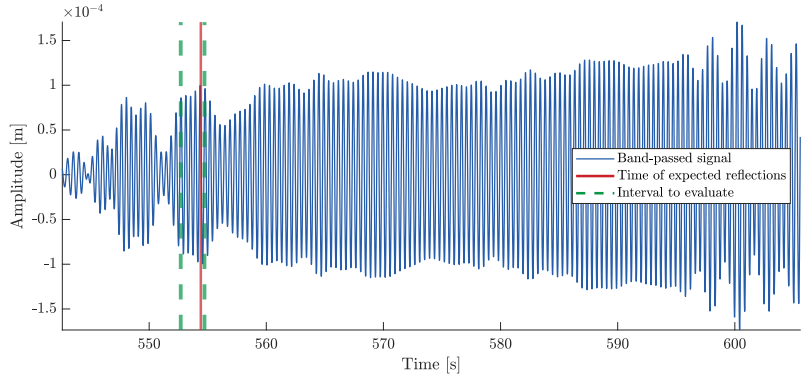

Figure C.12: Time series of the moonpool response of M1 with $H/\lambda = 1/100$ for $T = 0.42$ s. The interval is qualitatively chosen, based on values into the time series. Note the small dimensions on the vertical axis.

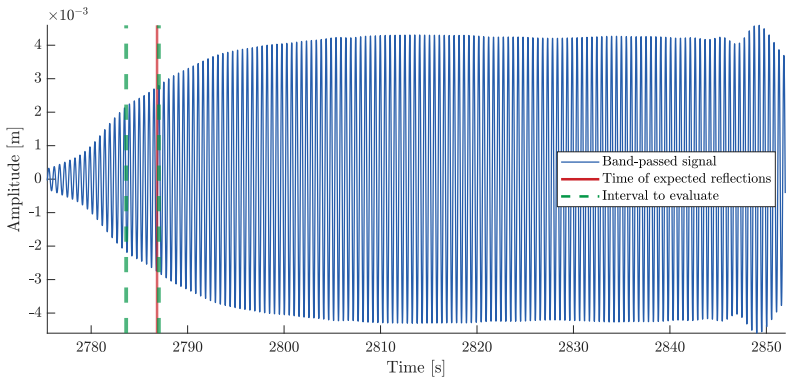

Figure C.13: Time series of the moonpool response of M1 with $H/\lambda = 1/100$ for $T = 0.51$ s. The interval is qualitatively chosen, as the slope in the response seems to decay before the reflection line.

C.1.7 Measured Wave Amplitude for M1 and M2

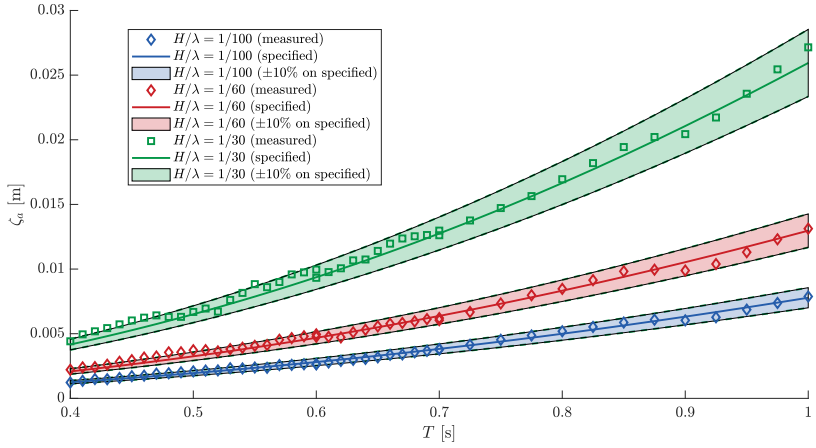

Figure C.14: Measured and theoretical wave amplitudes at each wave period during the M1 tests. A interval of $\pm 10\%$ to the specified wave amplitude is shown. In general, most waves are inside this interval.

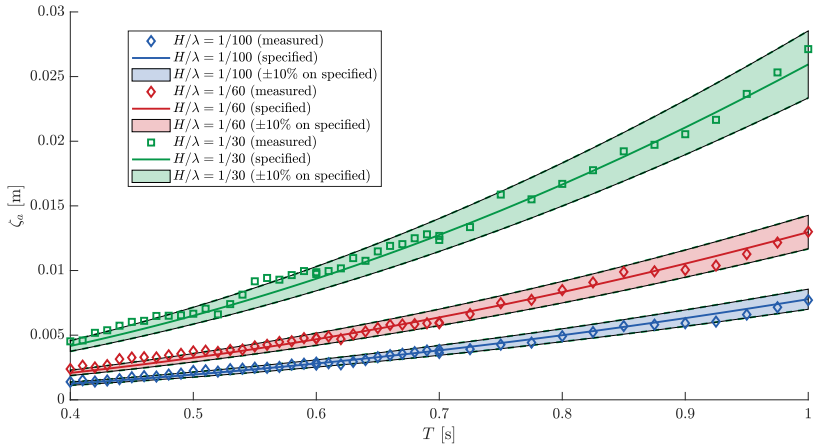

Figure C.15: Measured and theoretical wave amplitudes at each wave period during the M2 tests. A interval of $\pm 10\%$ to the specified wave amplitude is shown. In general, most waves are inside this interval.

Appendix D: Parametric Study

D.1.1 Wave Steepness

Table D.1: Representative joint peak frequency of significant wave height and spectral peak period in the northern North Sea (Faltinsen, 1990).

H_S \ T_p	3	4	5	(6)	7	(8)	9	(10)	11	(12)	13	14	15	16	17	18	19	21	22	Sum
1	59	403	1061	1569	1634	1362	982	643	395	232	132	74	41	22	12	7	4	2	2	8636
2	9	212	1233	3223	5106	5814	5284	4102	2846	1821	1098	634	355	194	105	56	30	16	17	32155
3	0	8	146	831	2295	3896	4707	4456	3531	2452	1543	901	497	263	135	67	33	16	15	25792
4	0	0	6	85	481	1371	2406	2960	2796	2163	1437	849	458	231	110	50	22	10	7	15442
5	0	0	0	4	57	315	898	1564	1879	1696	1228	748	398	191	84	35	13	5	3	9118
6	0	0	0	0	3	39	207	571	950	1069	885	575	309	142	58	21	7	2	1	4839
7	0	0	0	0	0	2	27	136	347	528	533	387	217	98	37	12	4	1	0	2329
8	0	0	0	0	0	0	2	20	88	197	261	226	138	64	23	7	2	0	0	1028
9	0	0	0	0	0	0	0	2	15	54	101	111	78	39	14	4	1	0	0	419
10	0	0	0	0	0	0	0	0	2	11	30	45	39	22	8	2	1	0	0	160
11	0	0	0	0	0	0	0	0	0	2	7	15	16	11	5	1	0	0	0	57
12	0	0	0	0	0	0	0	0	0	0	1	4	6	5	2	1	0	0	0	19
13	0	0	0	0	0	0	0	0	0	0	0	1	2	2	1	0	0	0	0	6
14	0	0	0	0	0	0	0	0	0	0	0	0	0	1	0	0	0	0	0	1
15	0	0	0	0	0	0	0	0	0	0	0	0	0	0	0	0	0	0	0	0
Sum	68	623	2446	5712	9576	12799	14513	14454	12849	10225	7256	4570	2554	1285	594	263	117	52	45	100001

The mean H_S, $\bar{H}_S$, wave length λ_p (based on the spectral peak period), assuming finite water depth of 110.40 m, and significant steepness is given in Table D.2.

Table D.2: Mean H_S, λ_p (based on the spectral peak period) and the significant wave steepness.

Tp	3	4	5	6	7	8	9	10	11	12	13	14	15	16	17	18	19	21	22
$\bar{H}_S$ [m]	1.13	1.37	1.63	1.90	2.19	2.50	2.84	3.21	3.60	3.98	4.31	4.56	4.66	4.61	4.34	3.95	3.60	3.19	2.89
λ_p [m]	14.05	24.98	39.03	56.21	76.50	99.92	126.46	156.09	188.68	223.91	261.27	300.07	339.66	379.55	419.37	458.92	498.11	575.23	613.19
$\bar{H}_S/\lambda$	0.0806	0.0547	0.0418	0.0339	0.0286	0.0250	0.0225	0.0206	0.0191	0.0178	0.0165	0.0152	0.0137	0.0121	0.0103	0.0086	0.0072	0.0055	0.0047
$\lambda/\bar{H}_S$	12.41	18.29	23.93	(29.54)	34.96	(39.99)	44.51	(48.59)	52.42	(56.30)	60.62	65.86	72.86	82.38	96.70	116.05	138.43	180.19	212.26

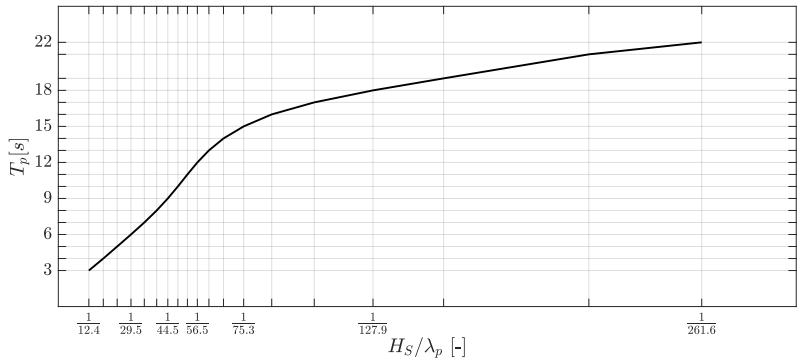

Figure D.1: Significant steepness versus peak period.

D.1.2 Adapted Experimental RAOs for the Parametric Study

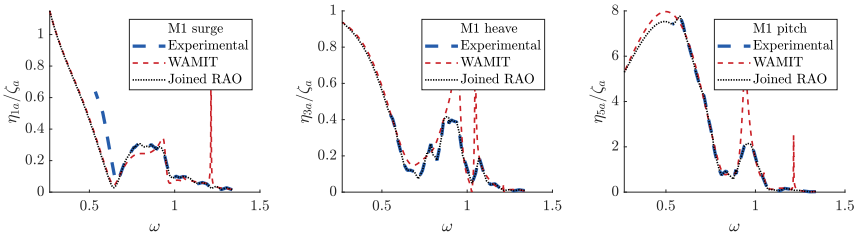

(a) Surge

(b) Heave

(c) Pitch

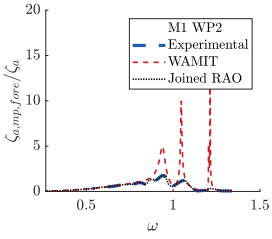

(d) Fore moonpool

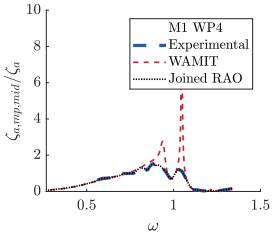

(e) Middle moonpool

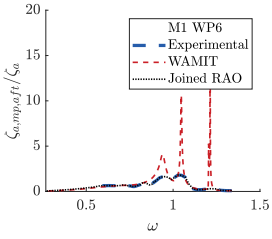

(f) Aft moonopool

Figure D.2: Adapted M1 RAOs for the parametric study

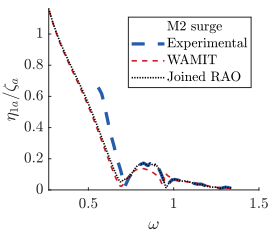

(a) Surge

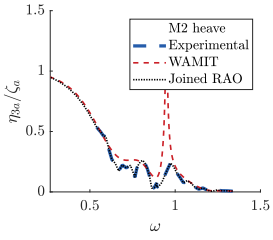

(b) Heave

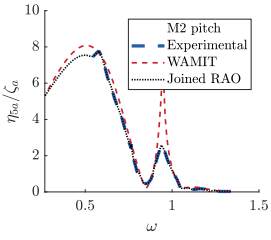

(c) Pitch

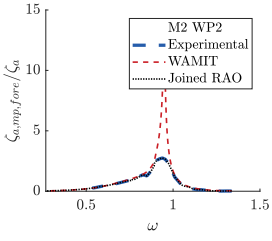

(d) Fore moonpool

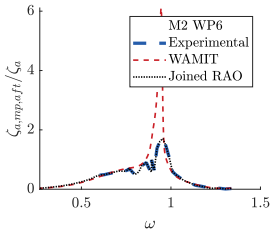

(e) Aft moonpool

Figure D.3: Adapted M2 RAOs for the parametric study

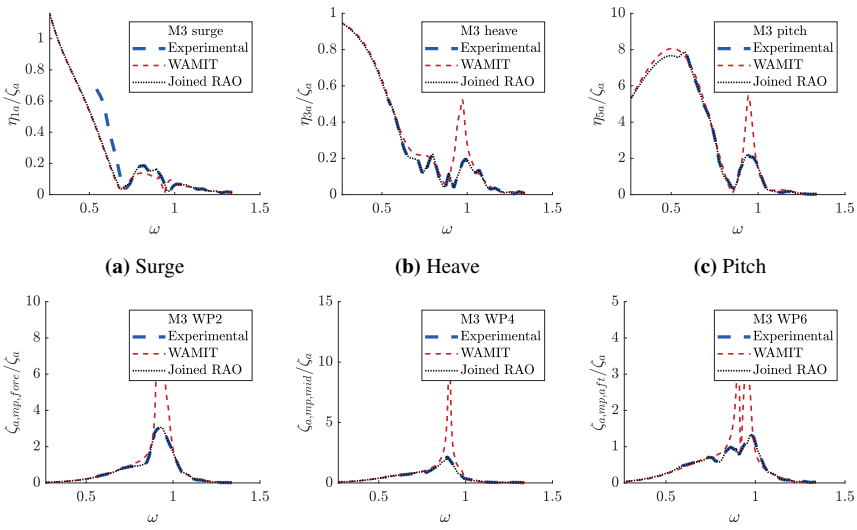

(a) Surge **(b)** Heave **(c)** Pitch

(d) Fore moonpool **(e)** Middle moonpool **(f)** Aft moonopool

Figure D.4: Adapted M3 RAOs for the parametric study

Appendix E: Experimental Results

E.1.1 M1 RAOs

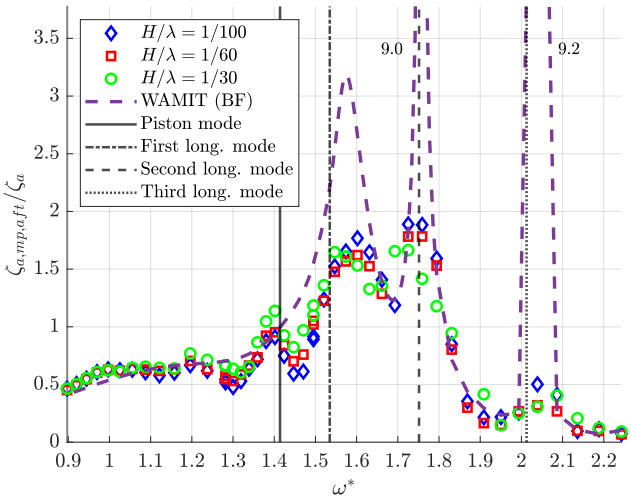

Figure E.1: M1 aft wave probe RAO

E.1.2 M2 RAOs

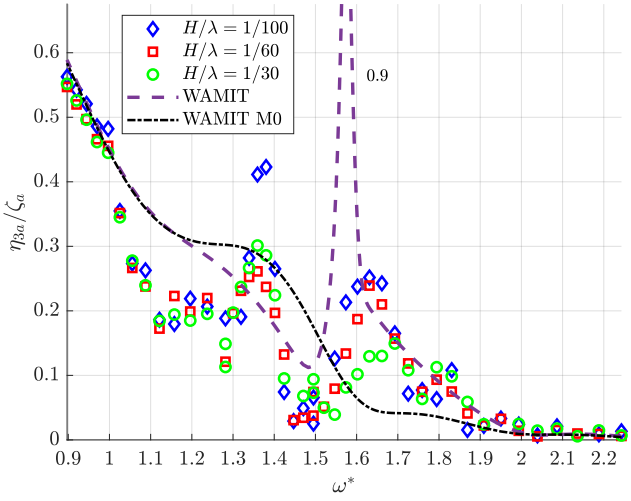

Figure E.2: M2 heave RAO

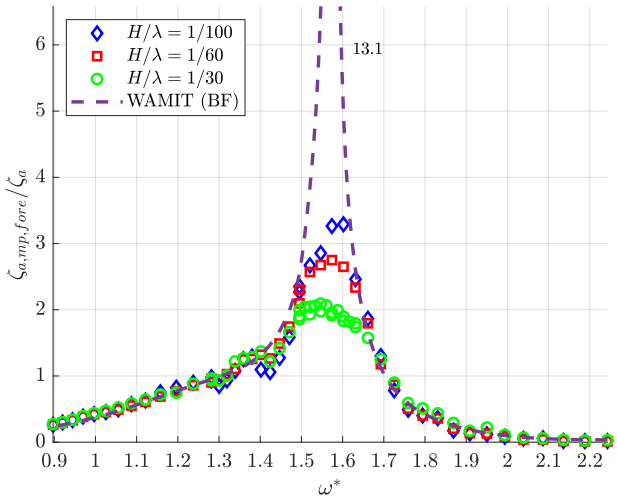

Figure E.3: M2 fore moonpool RAO

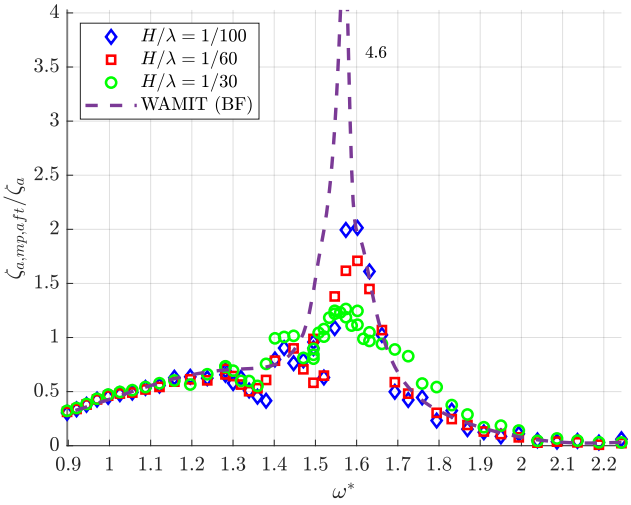

Figure E.4: M2 aft moonpool RAO

E.1.3 M3 RAOs

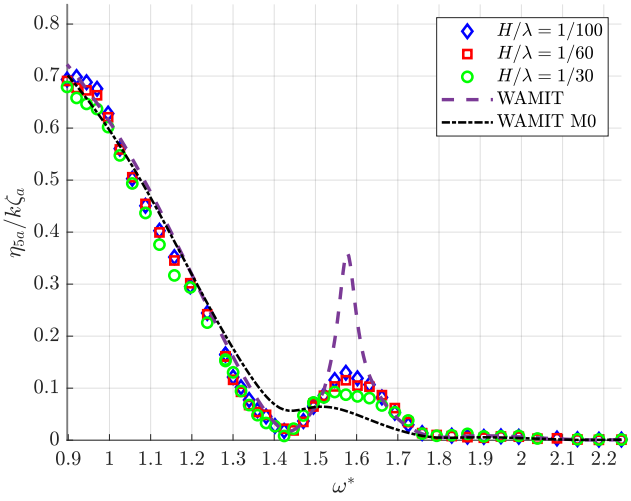

Figure E.5: M3 pitch RAO

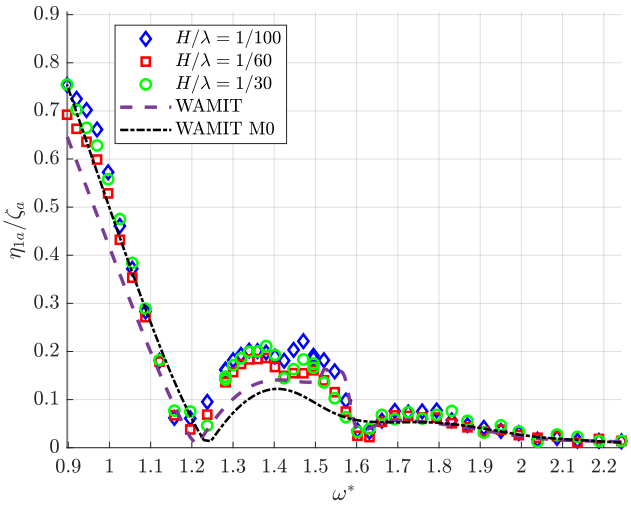

Figure E.6: M3 surge RAO

Appendix F: Parametric Study Results

F.1.1 M1

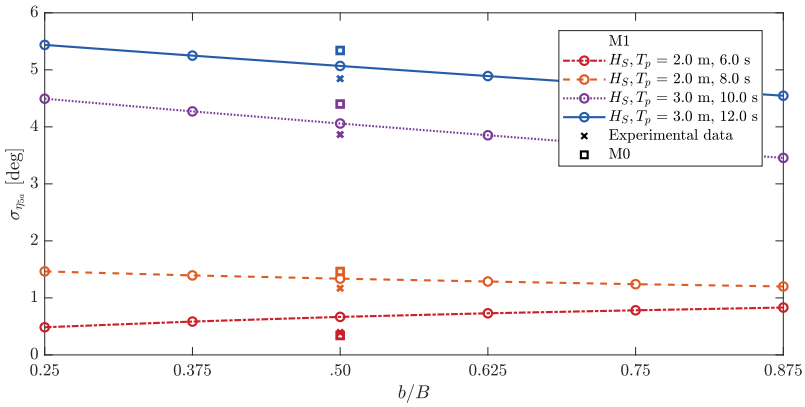

Figure F.1: The standard deviation of the pitch amplitude, $\sigma_{\eta_{5a}}$, of M1 for a set of moonpool width-to-vessel beam ratios and operational sea states. Experimental data and data for M0 is included for comparison.

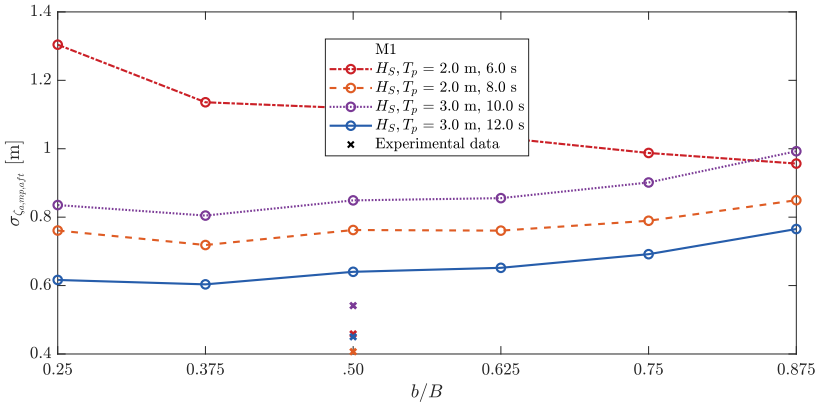

Figure F.2: The standard deviation of the moonpool response amplitude at the aft of the moonpool, $\sigma_{\zeta_{a,mp,aft}}$, of M1 for a set of moonpool width-to-vessel beam ratios and operational sea states. Experimental data is included for comparison.

F.1.2 M2

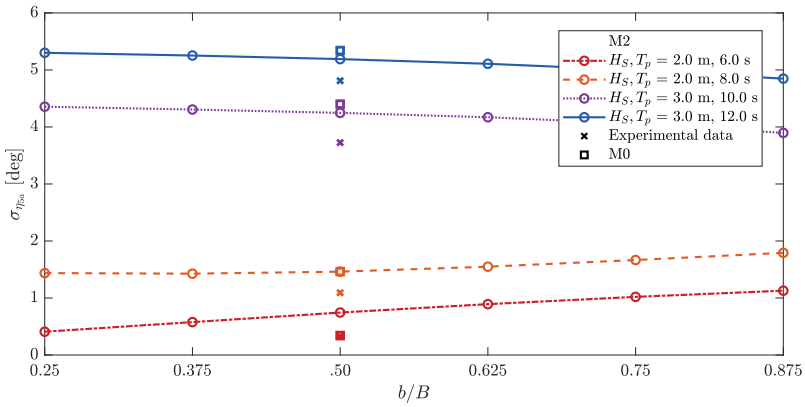

Figure F.3: The standard deviation of the pitch amplitude, $\sigma_{\eta_{5a}}$, of M2 for a set of moonpool width-to-vessel beam ratios and operational sea states. Experimental data and data for M0 is included for comparison.

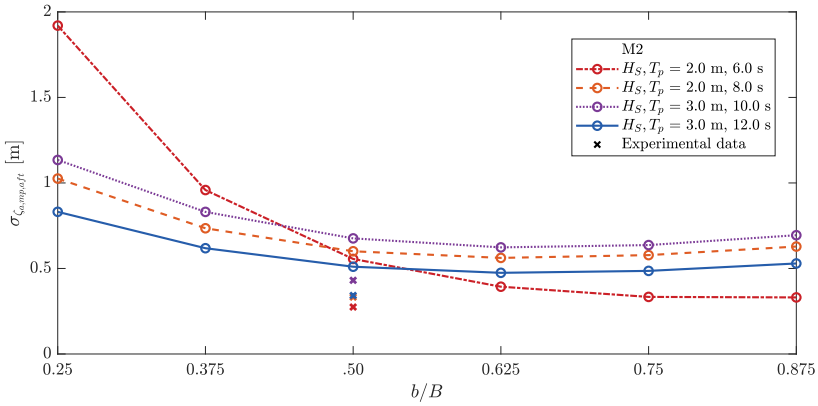

Figure F.4: The standard deviation of the moonpool response amplitude at the aft moonpool, $\sigma_{\zeta_{a,mp,aft}}$, of M2 for a set of moonpool width-to-vessel beam ratios and operational sea states. Experimental data is included for comparison.

F.1.3 M3

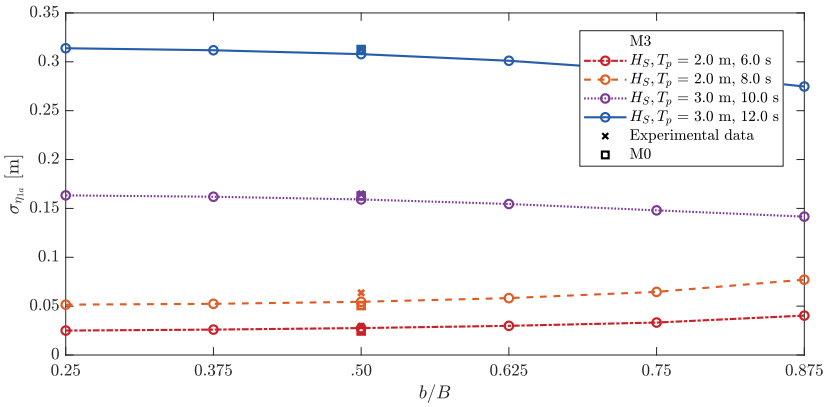

Figure F.5: The standard deviation of the surge amplitude, $\sigma_{\eta_{1a}}$, of M3 for a set of moonpool width-to-vessel beam ratios and operational sea states. Experimental data and data for M0 is included for comparison.

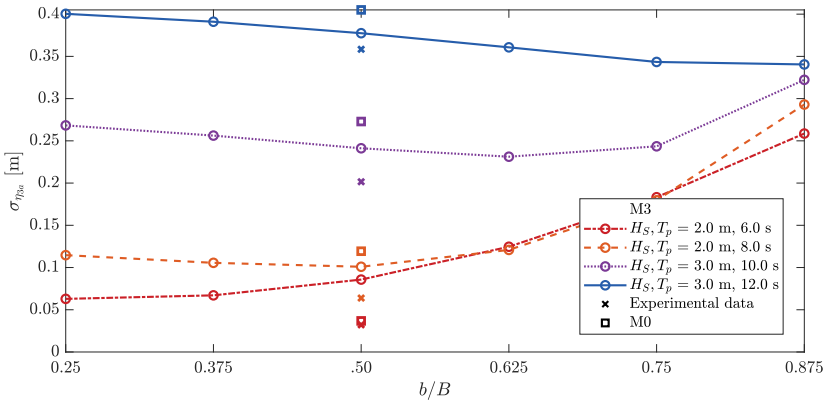

Figure F.6: The standard deviation of the heave amplitude, $\sigma_{\eta_{3a}}$, of M3 for a set of moonpool width-to-vessel beam ratios and operational sea states. Experimental data and data for M0 is included for comparison.

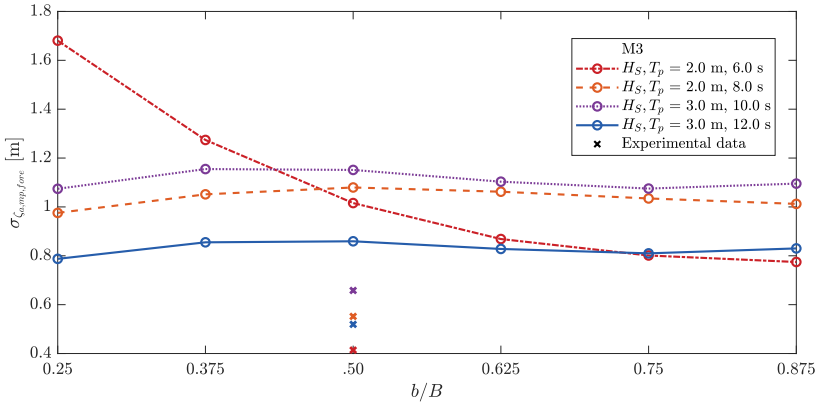

Figure F.7: The standard deviation of the moonpool response amplitude at the aft moonpool, $\sigma_{\zeta_{a,mp,fore}}$, of M3 for a set of moonpool width-to-vessel beam ratios and operational sea states. Experimental data is included for comparison.

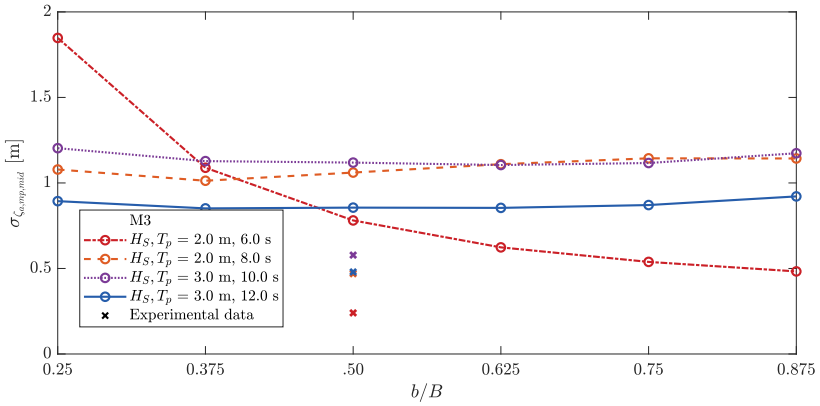

Figure F.8: The standard deviation of the moonpool response amplitude at the middle moonpool, $\sigma_{\zeta_{a,mp,mid}}$, of M3 for a set of moonpool width-to-vessel beam ratios and operational sea states. Experimental data is included for comparison.

F.1.4 M1 Heave Response Spectra

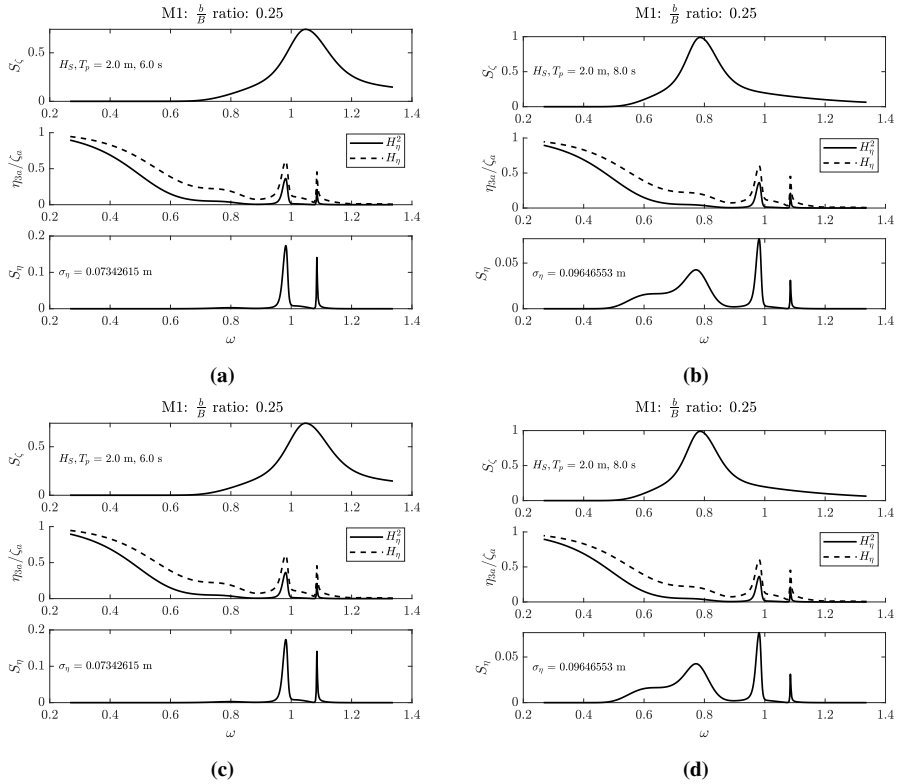

Figure F.9: M1 heave response spectra for $b/B = 0.25$.

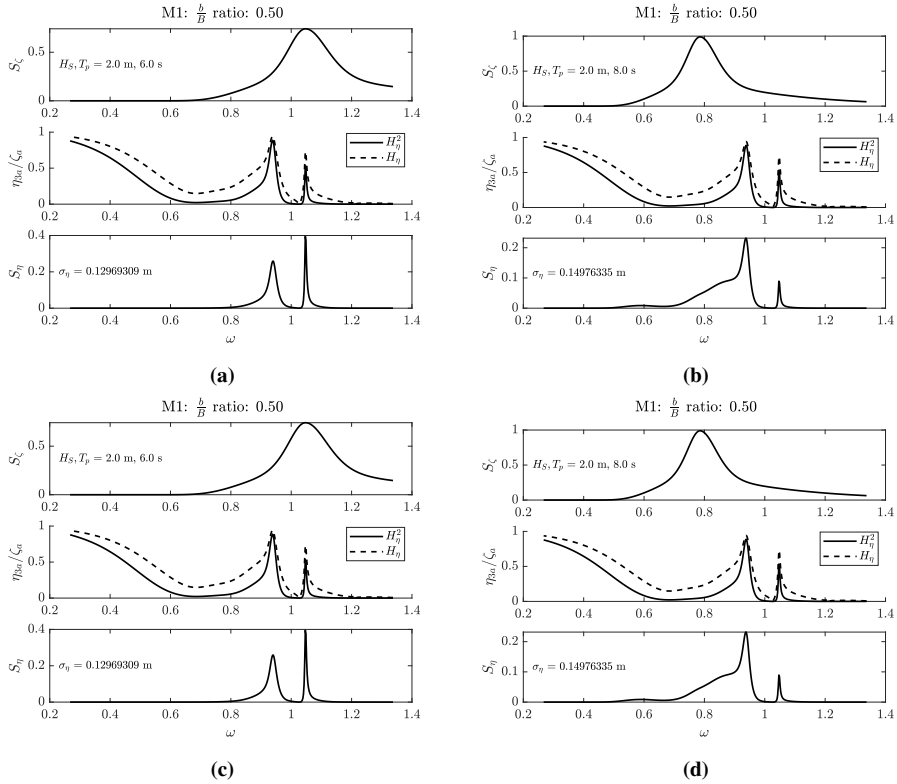

Figure F.10: M1 heave response spectra for $b/B = 0.50$.

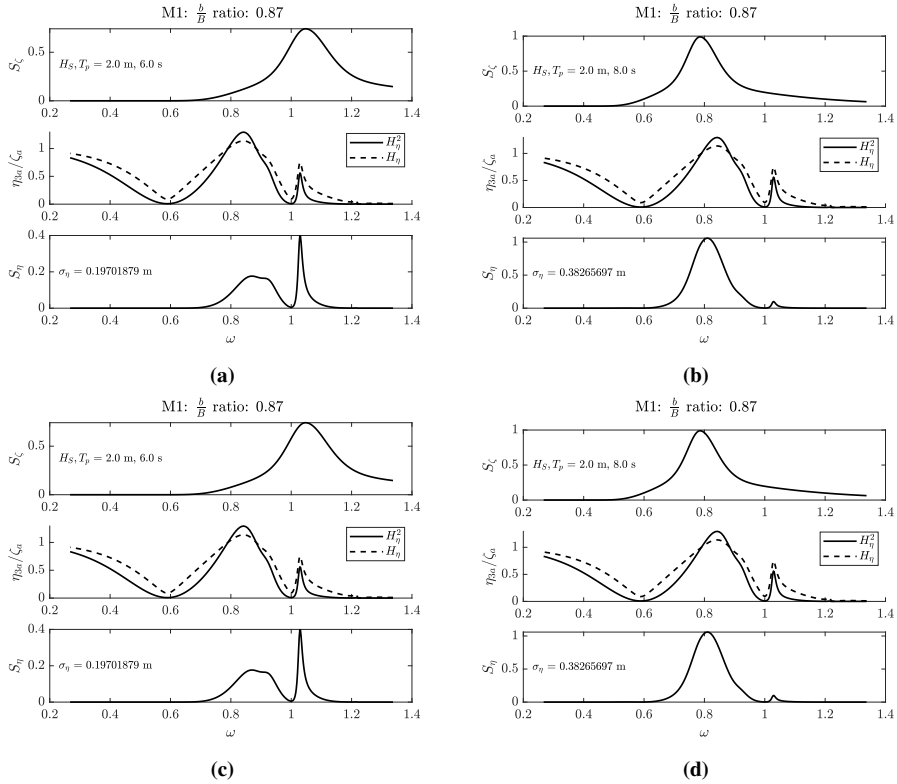

Figure F.11: M1 heave response spectra for $b/B = 8750$.

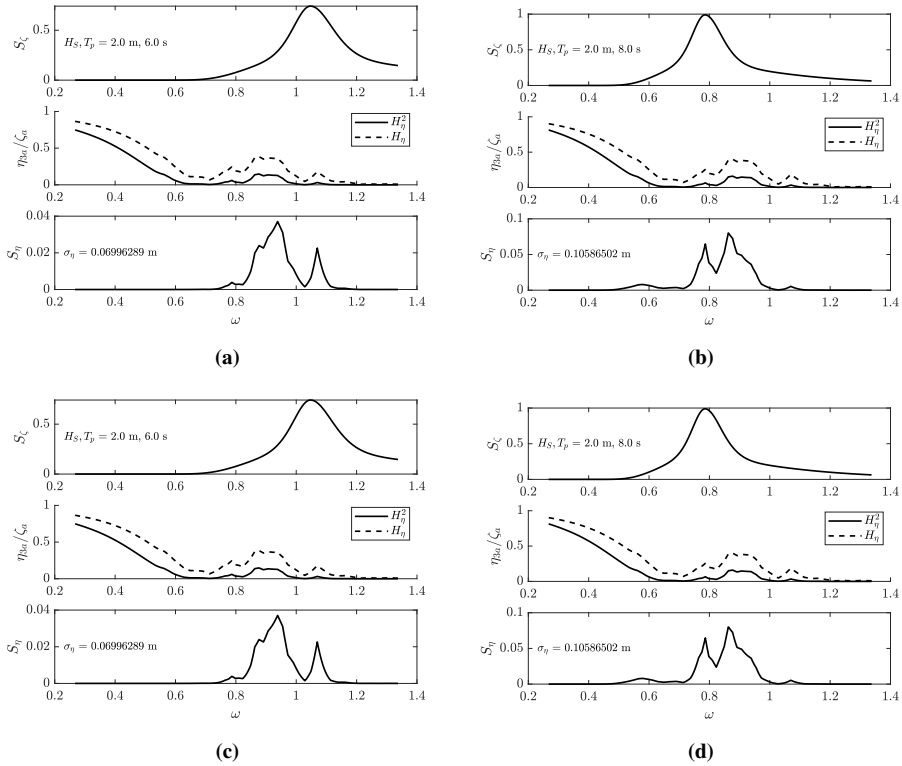

Figure F.12: M1 experimental heave response spectra.

F.1.5 M2 Heave Response Spectra

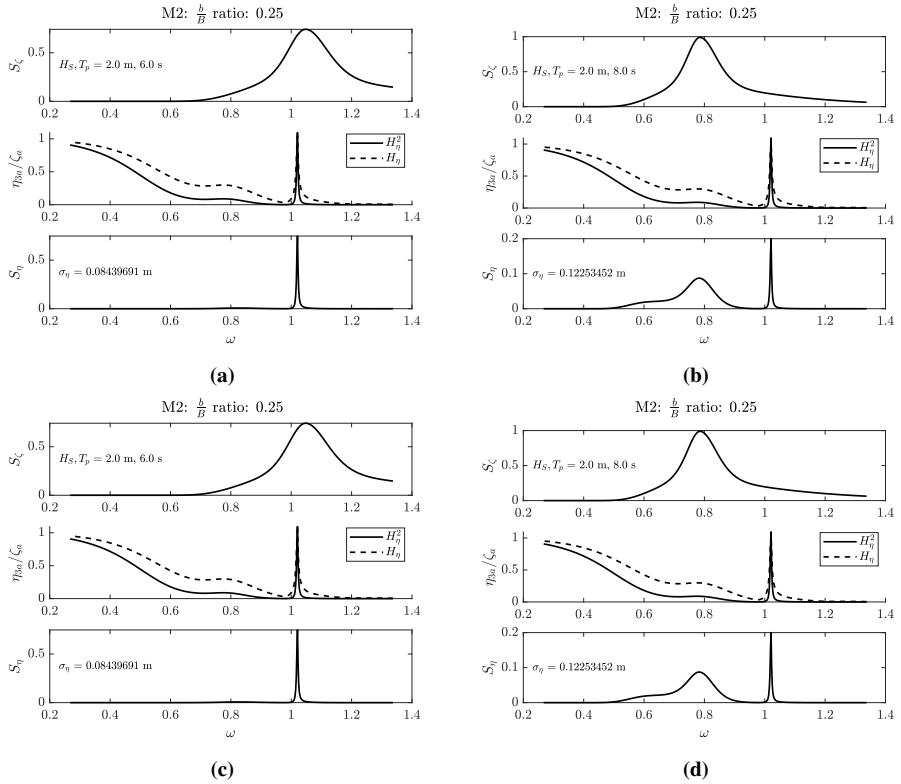

Figure F.13: M2 heave response spectra for $b/B = 0.25$.

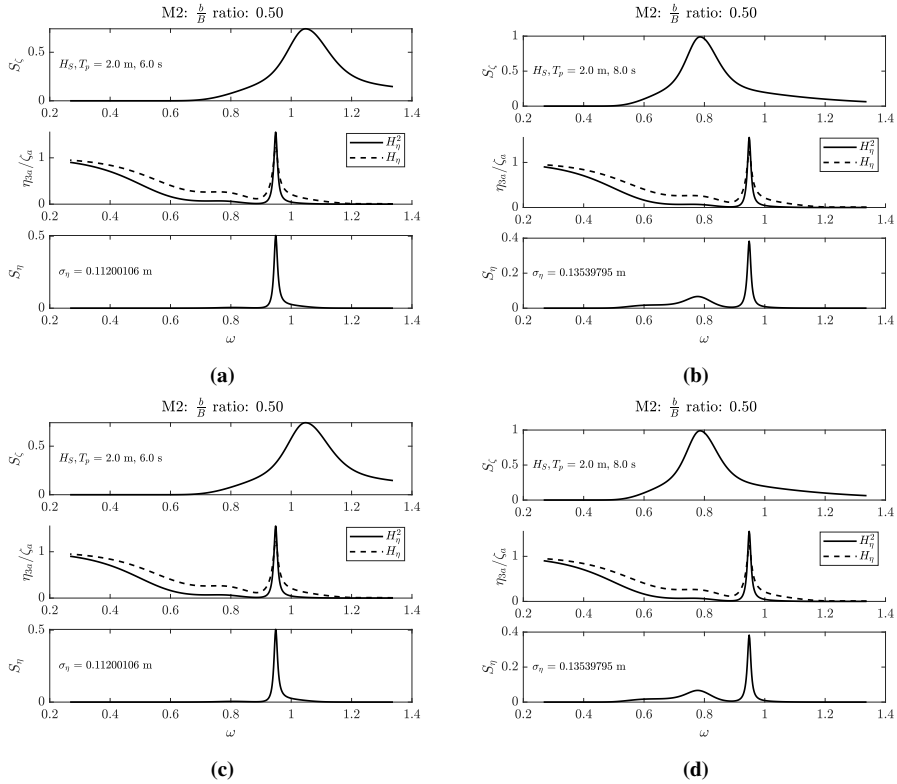

Figure F.14: M2 heave response spectra for $b/B = 0.50$.

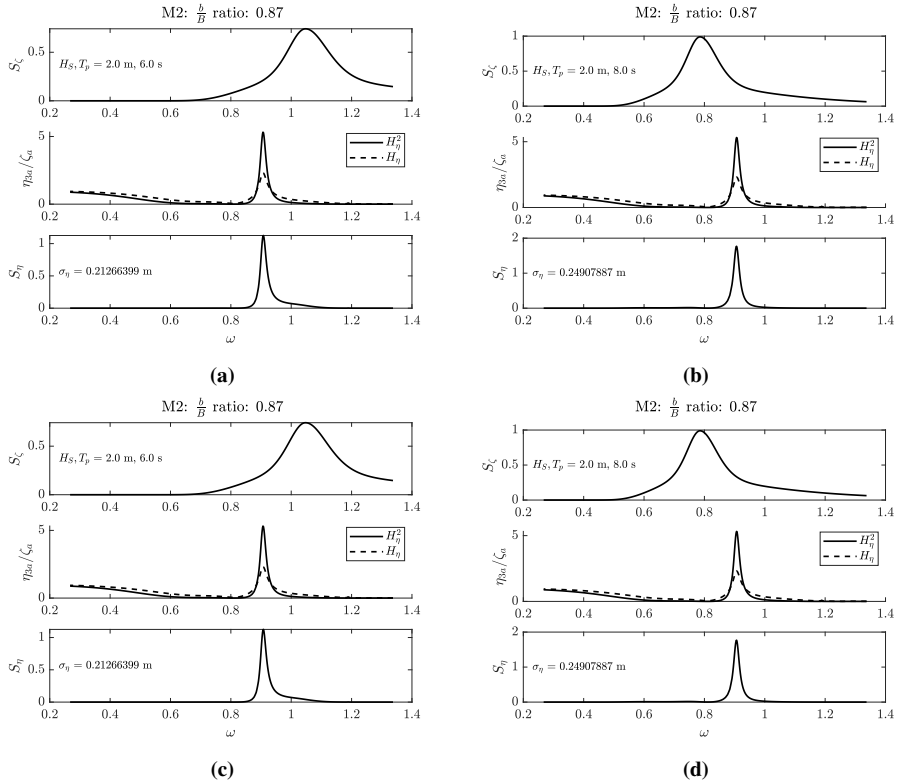

Figure F.15: M2 heave response spectra for $b/B = 8750$.

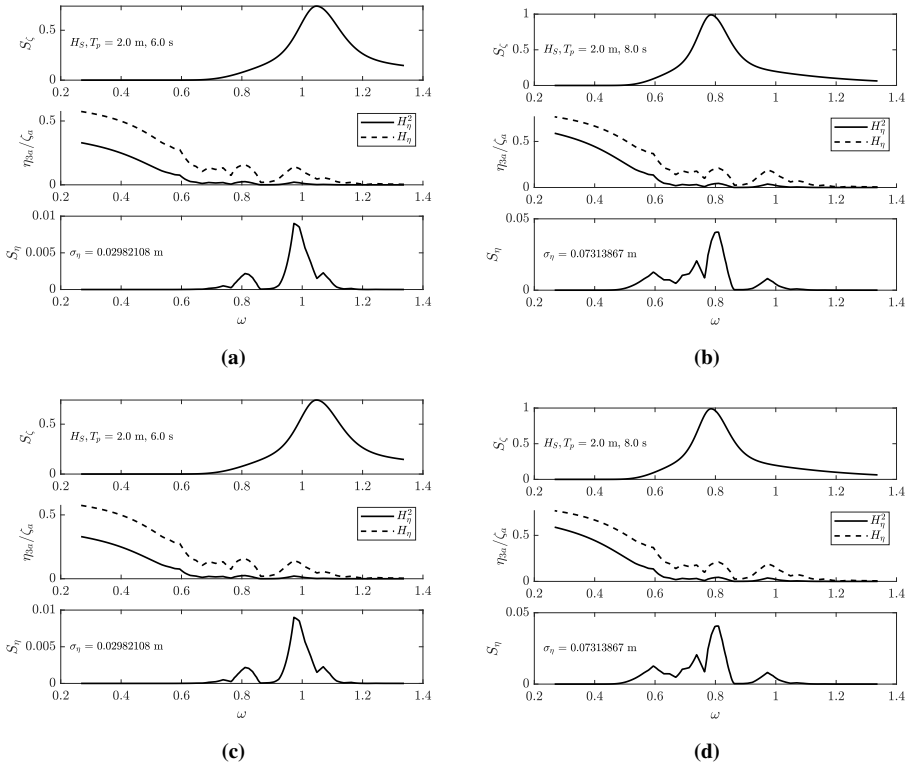

Figure F.16: M2 experimental heave response spectra.

F.1.6 M3 Pitch Response Spectra

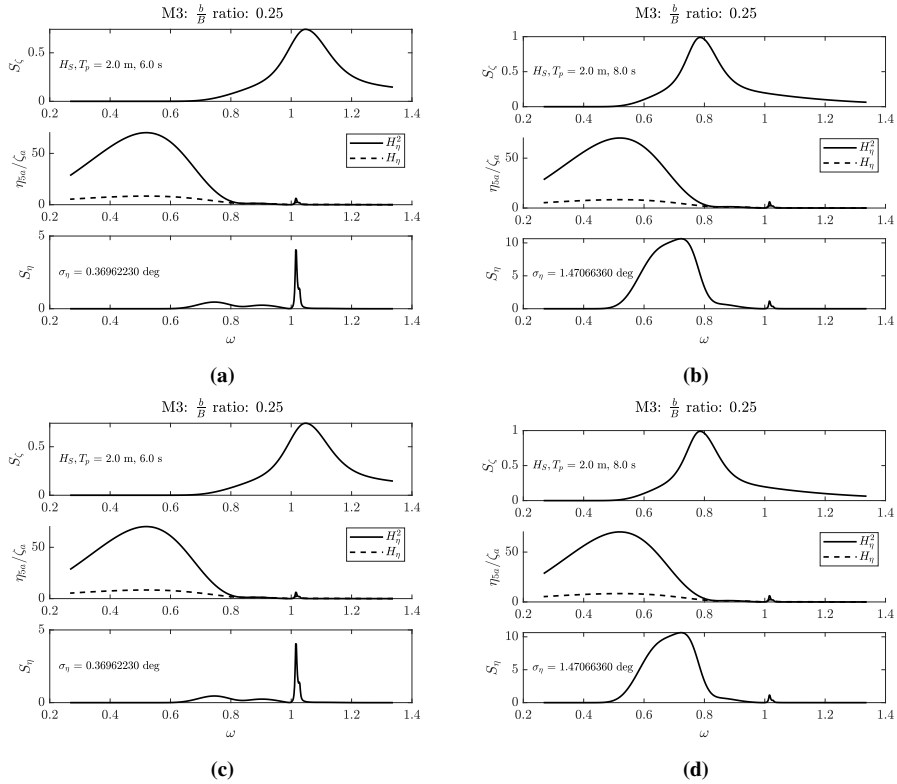

Figure F.17: M3 pitch response spectra for $b/B = 0.25$.

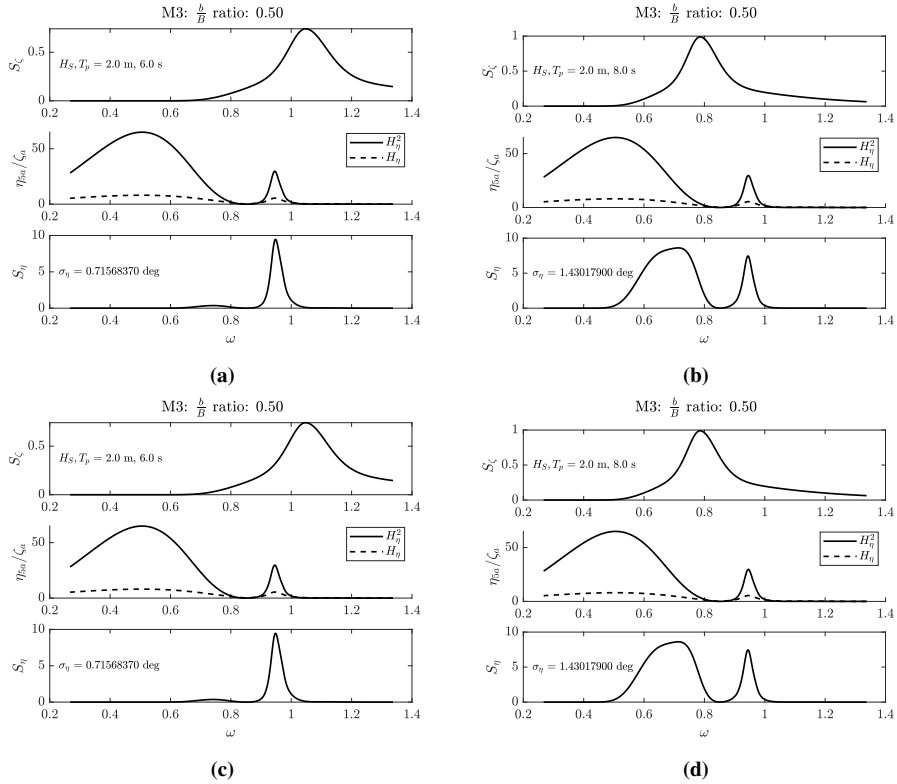

Figure F.18: M3 pitch response spectra for $b/B = 0.50$.

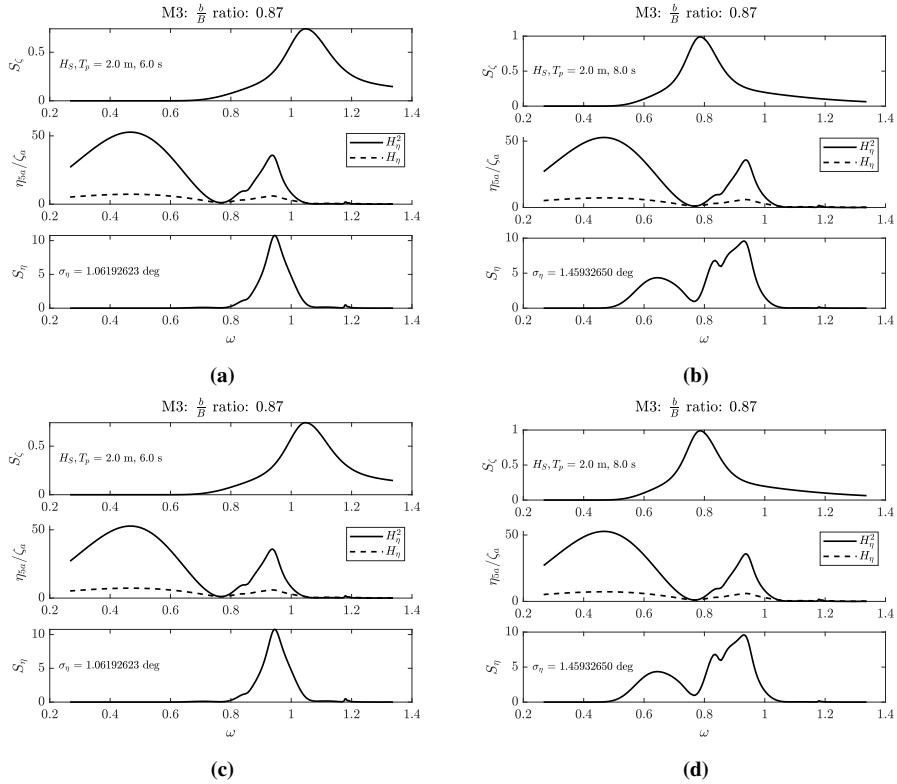

Figure F.19: M3 pitch response spectra for $b/B = 8750$.

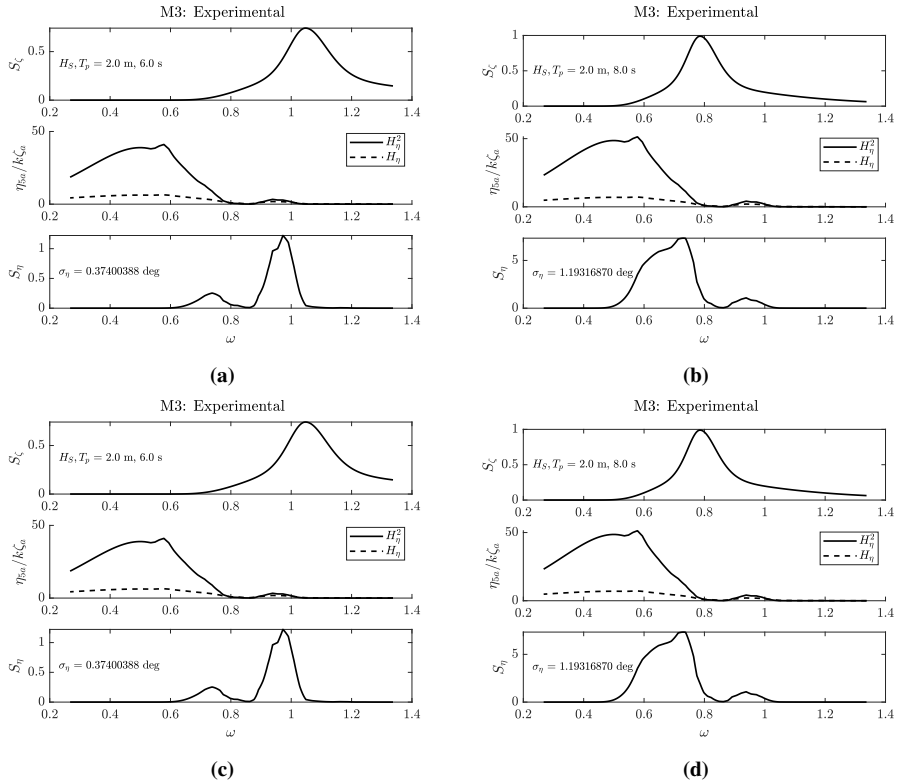

Figure F.20: M3 experimental pitch response spectra.

F.1.7 M1 Response Spectra, Fore Part of the Moonpool

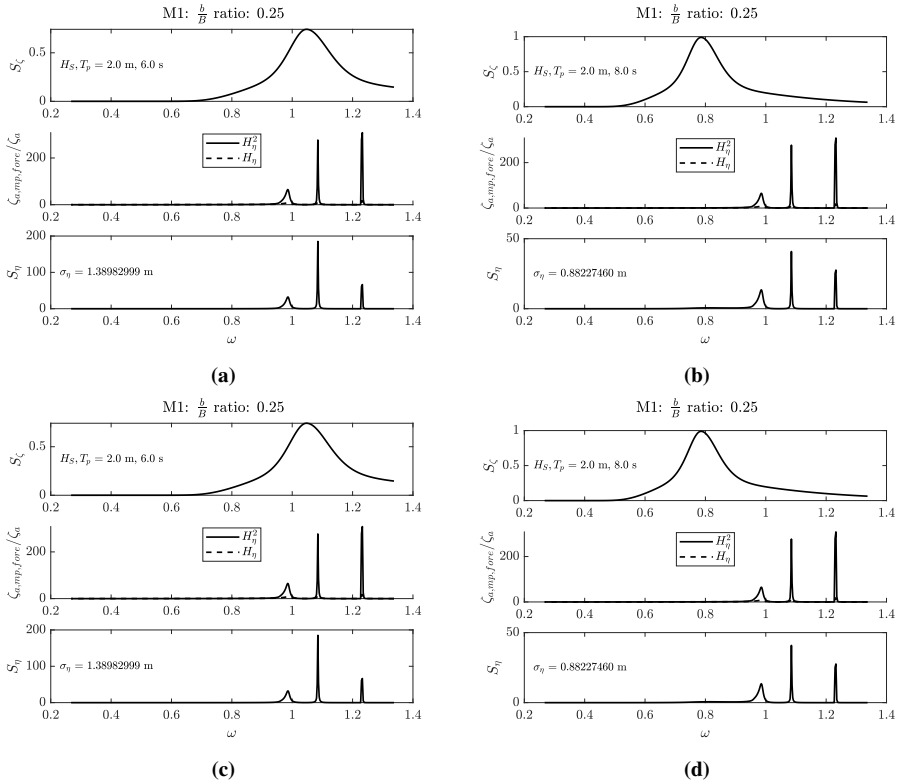

Figure F.21: M1 fore moonpool response spectra for $b/B = 0.25$.

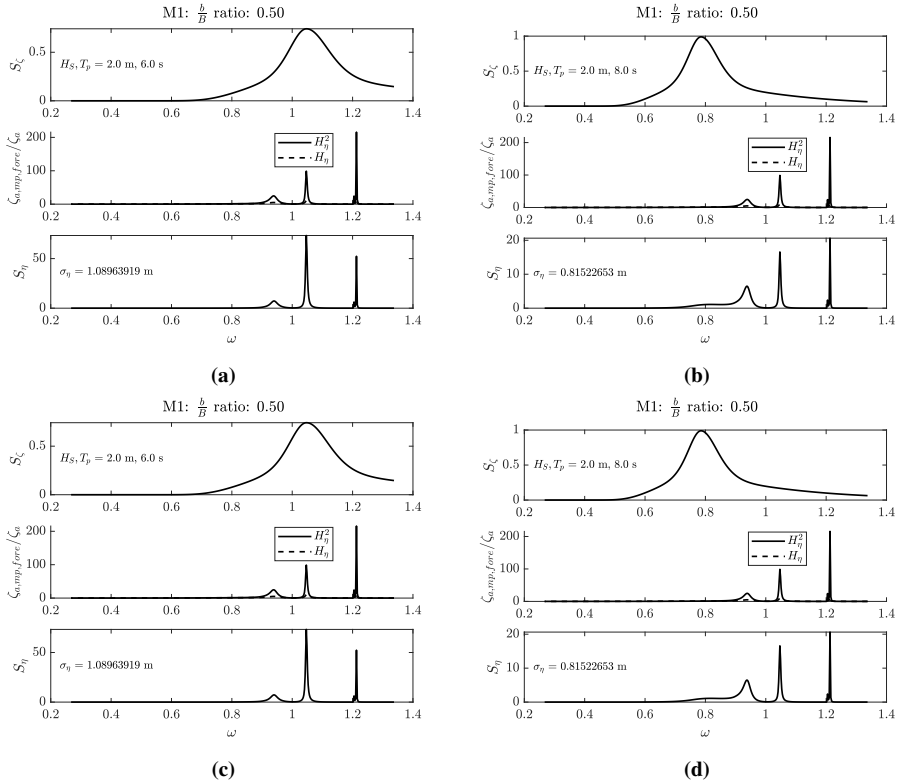

Figure F.22: M1 fore moonpool response spectra for $b/B = 0.50$.

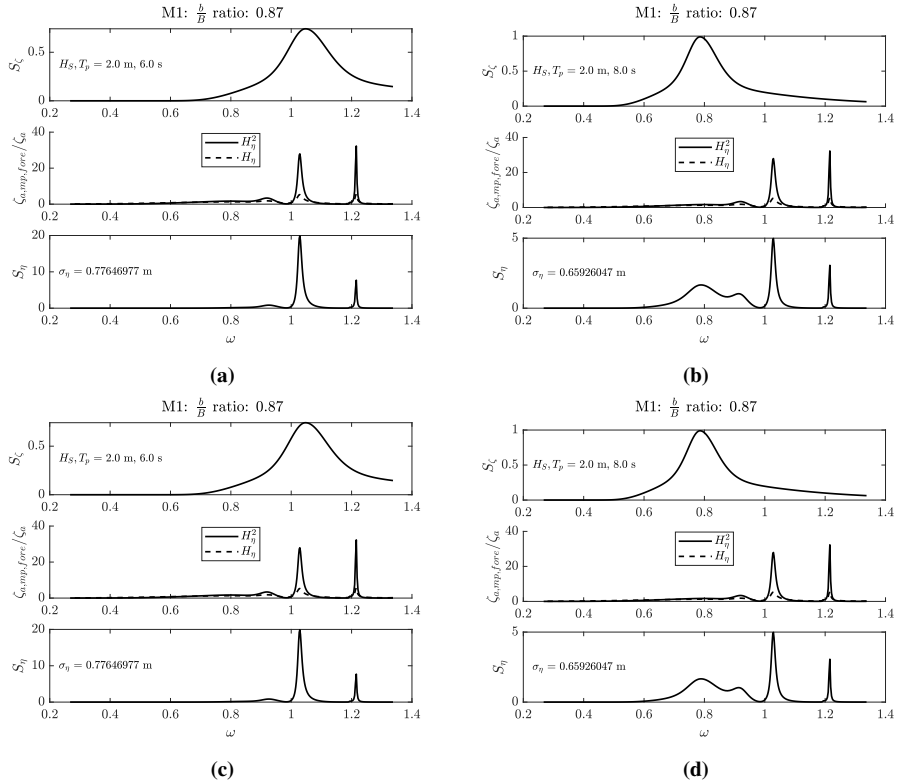

Figure F.23: M1 fore moonpool response spectra for $b/B = 8750$.

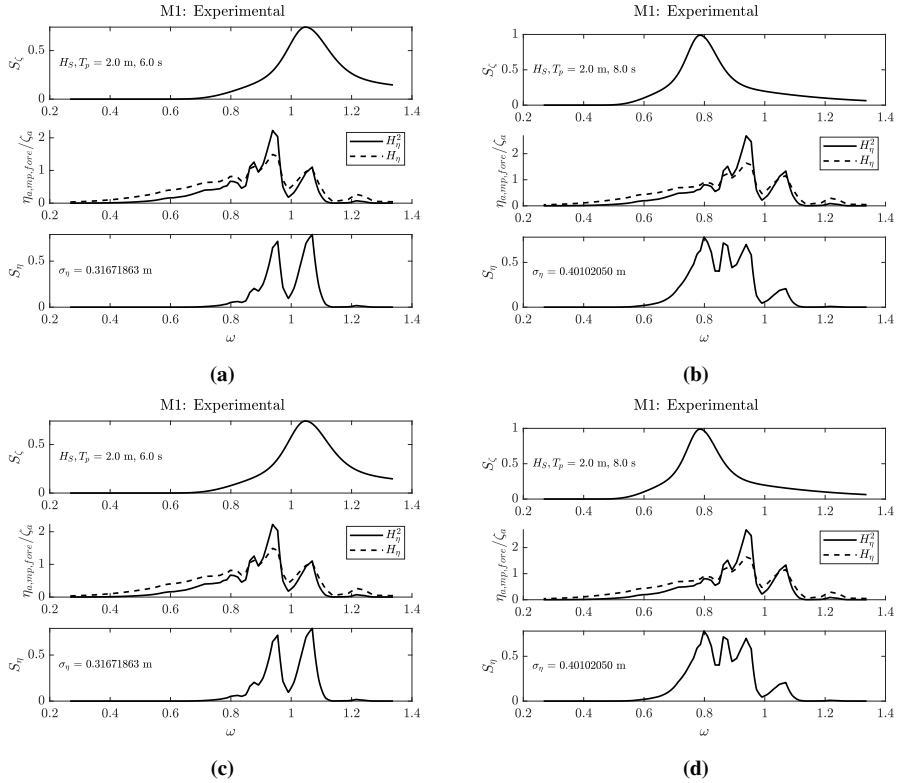

Figure F.24: M1 experimental fore moonpool response spectra.

F.1.8 M1 Response Spectra, Middle Part of the Moonpool

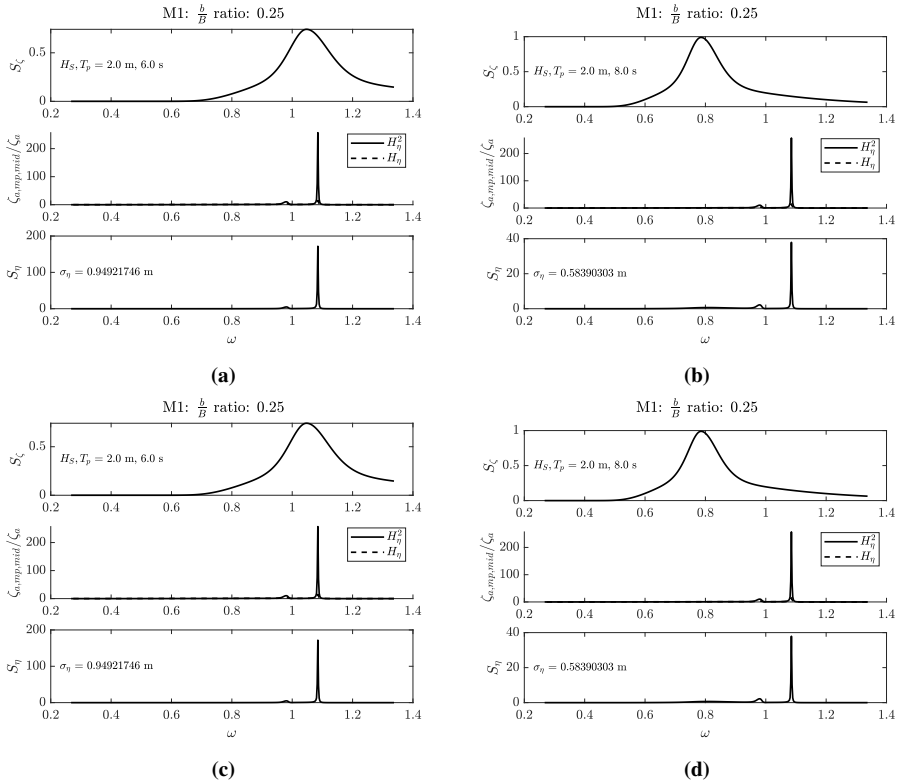

Figure F.25: M1 response spectra in the middle of the moonpool for $b/B = 0.25$.

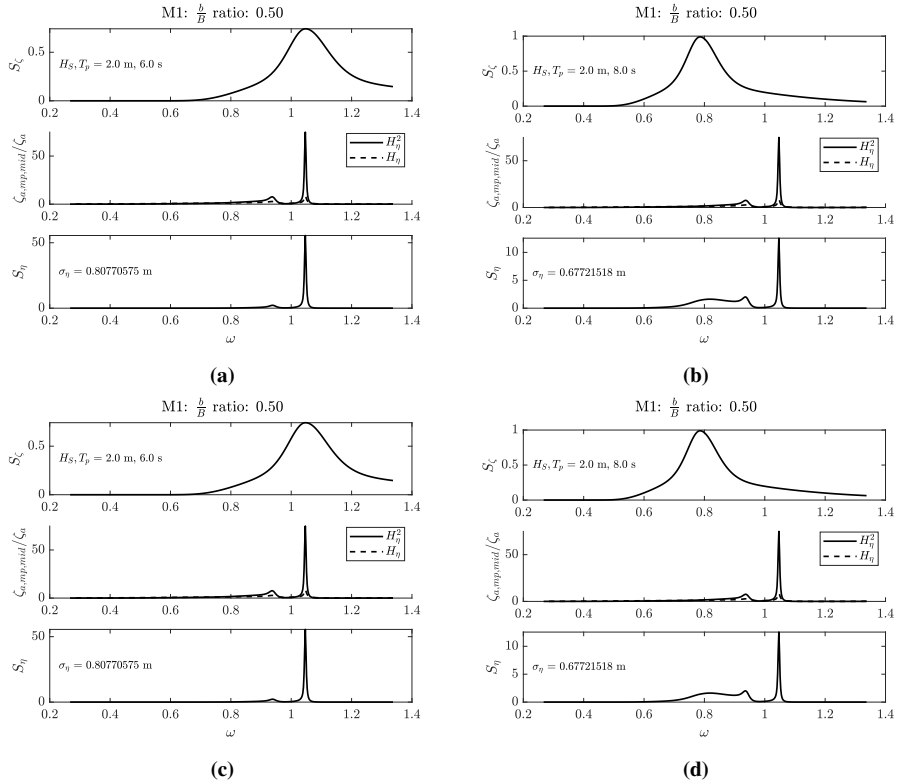

Figure F.26: M1 response spectra in the middle of the moonpool for $b/B = 0.50$.

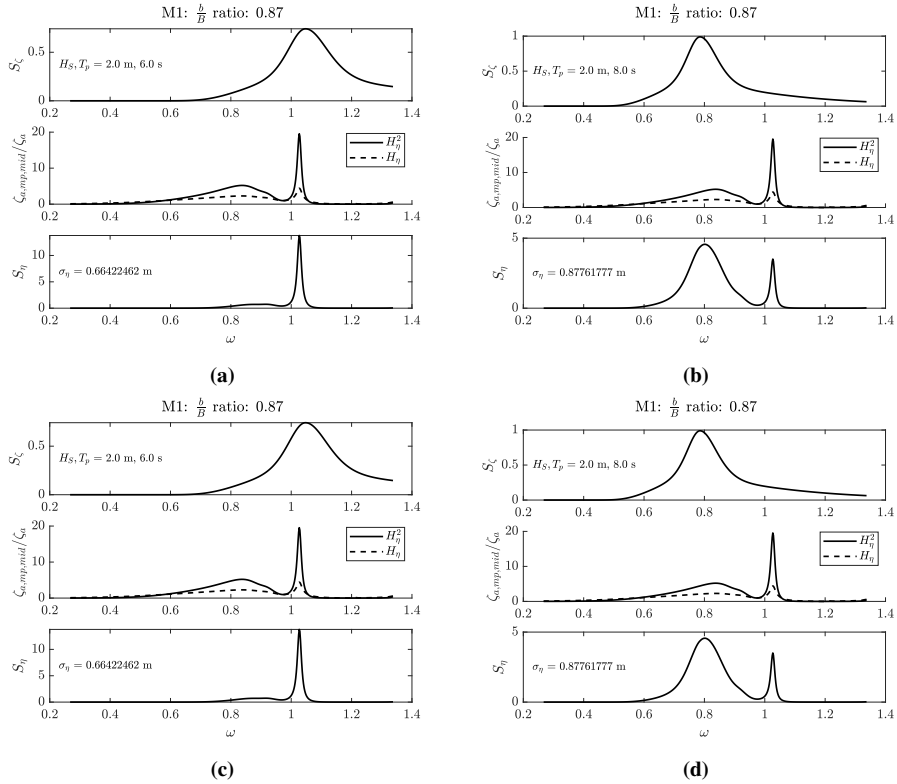

Figure F.27: M1 response spectra in the middle of the moonpool for $b/B = 8750$.

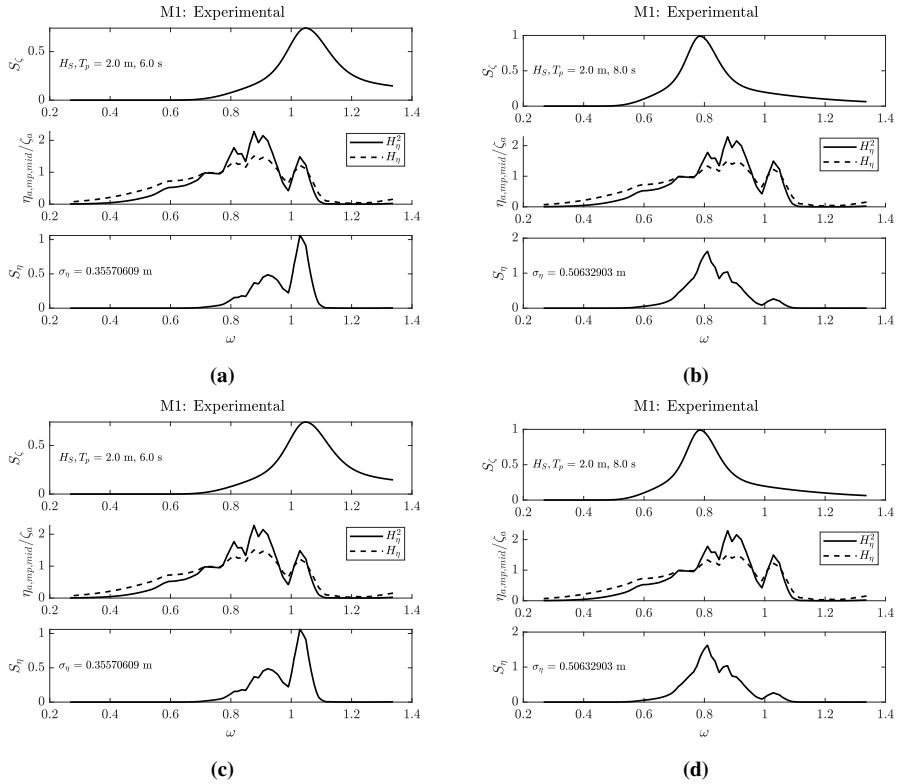

Figure F.28: M1 experimental response spectra in the middle of the moonpool.

F.1.9 Non-referred Experimental Response Spectra

Non-referred experimental response spectra for the four sea states in the parametric study follows. The quasi-experimental RAOs in Appendix D.1.2 are used.

M1 Surge

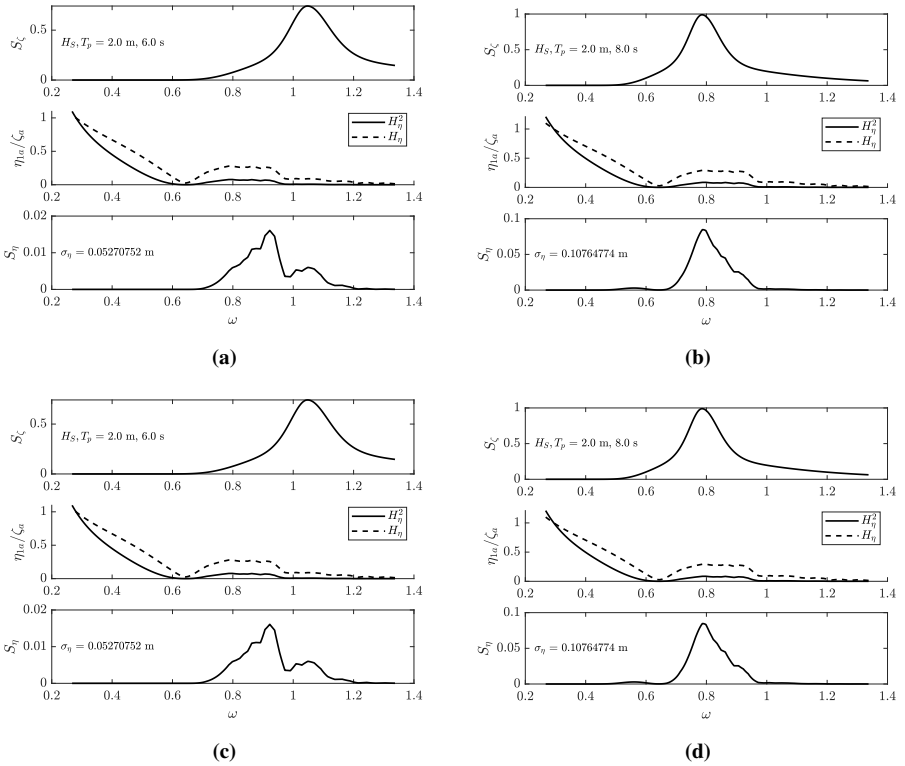

Figure F.29: M1 experimental surge response spectra.

M1 Pitch

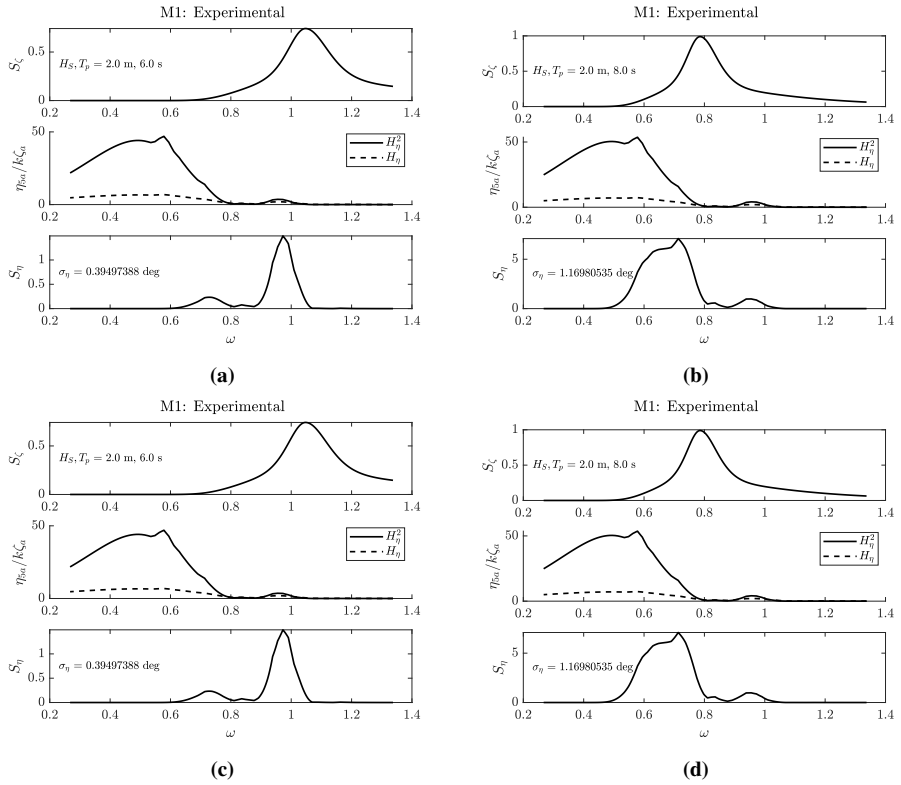

Figure F.30: M1 experimental pitch response spectra.

M1, Aft Part of the Moonpool

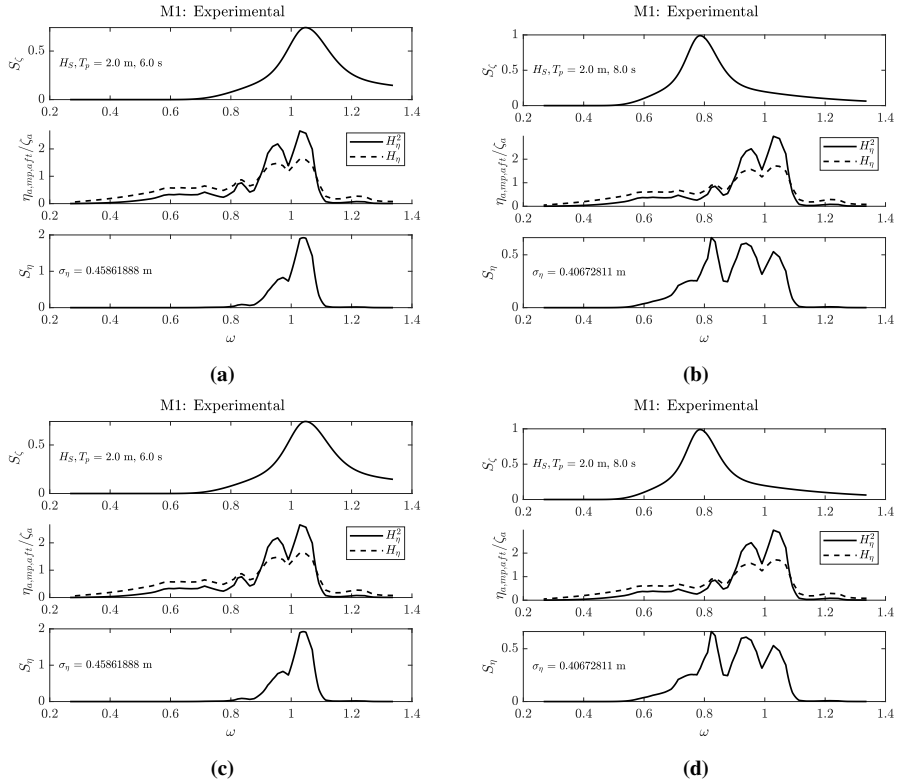

Figure F.31: M1 experimental response spectra for the aft part of the moonpool.

M2 Surge

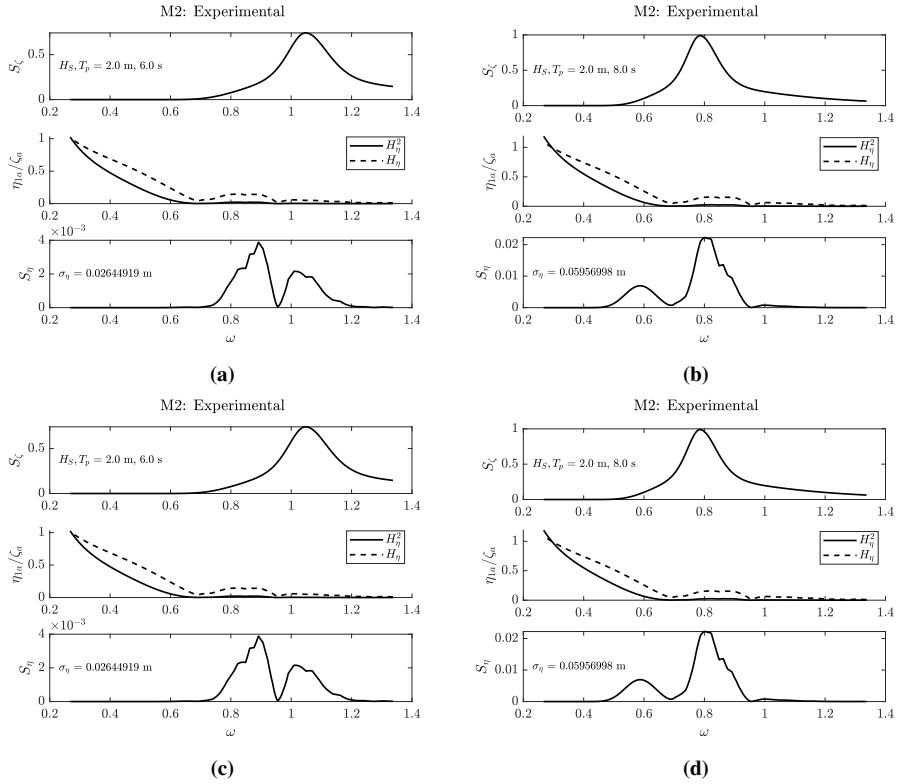

Figure F.32: M2 experimental surge response spectra.

M2 Pitch

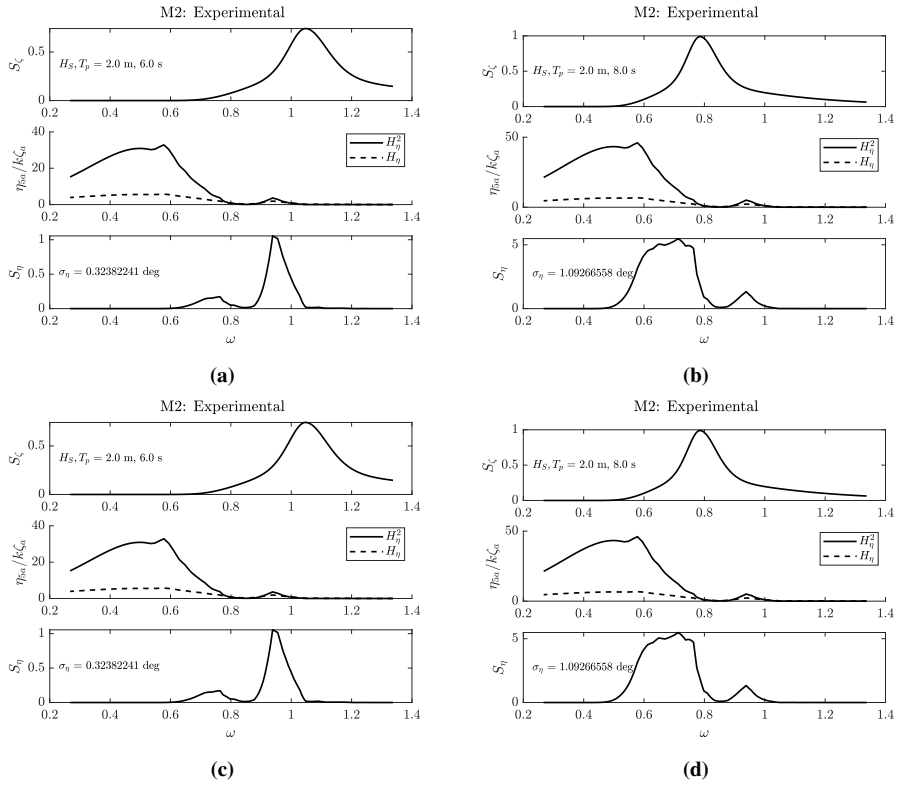

Figure F.33: M2 experimental pitch response spectra.

M2, Fore Moonpool

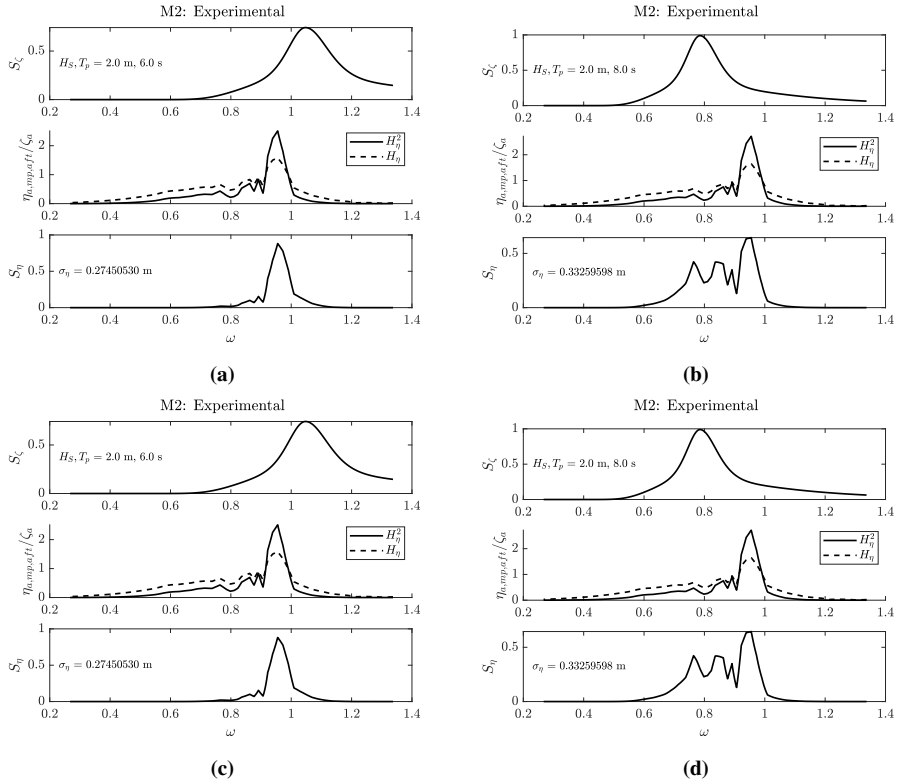

Figure F.34: M2 experimental response spectra for the fore moonpool.

M2, Aft Moonpool

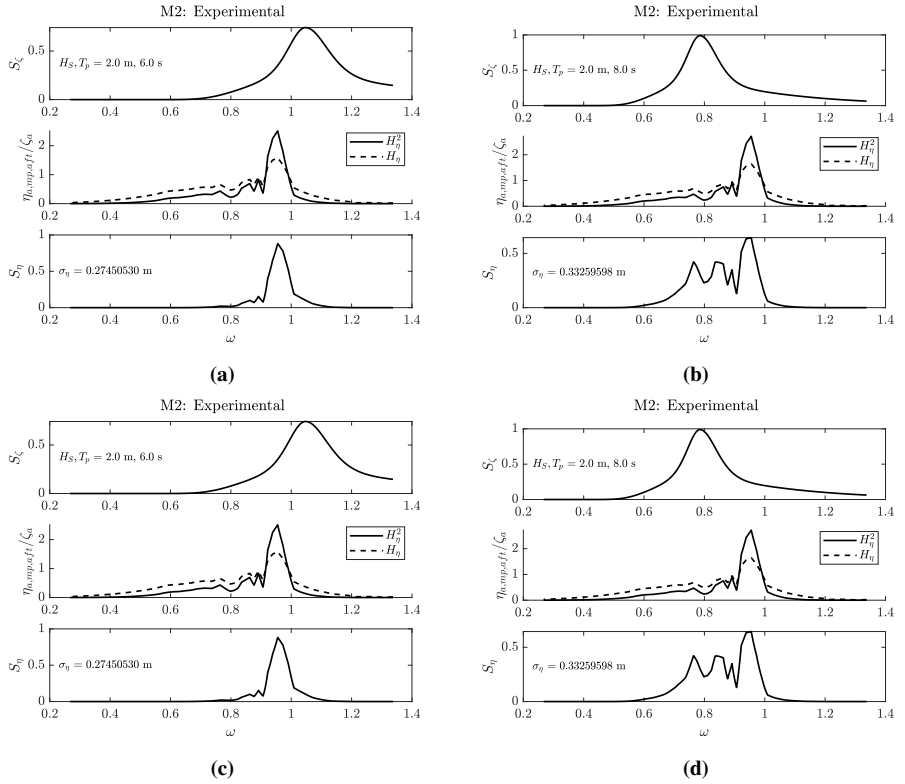

Figure F.35: M2 experimental response spectra for the aft moonpool.

M3 Surge

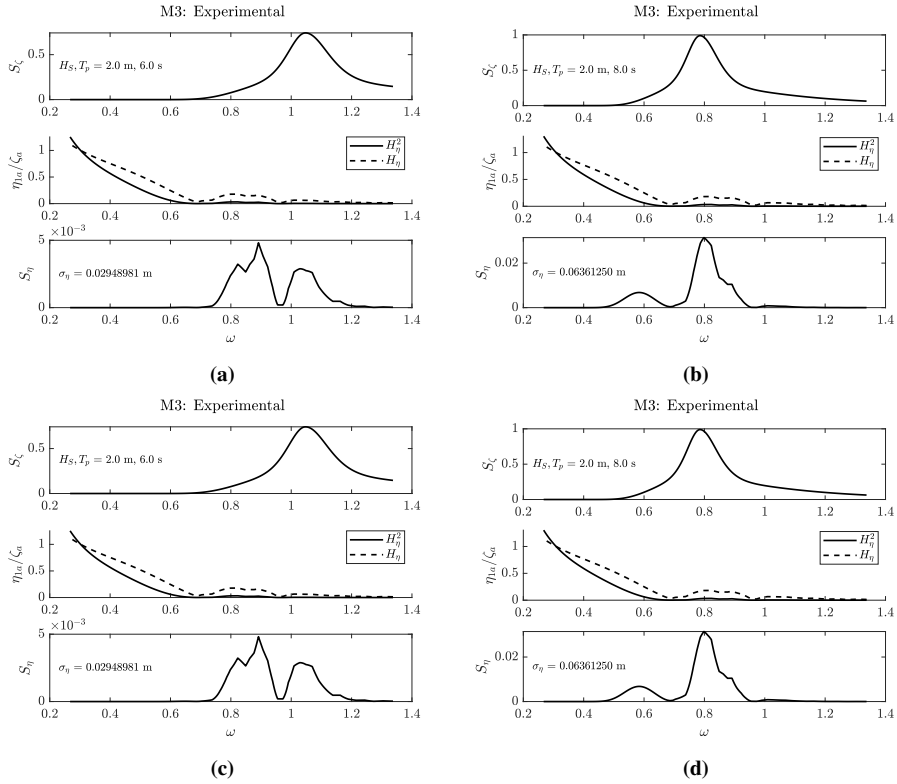

Figure F.36: M3 experimental surge response spectra.

M3 Heave

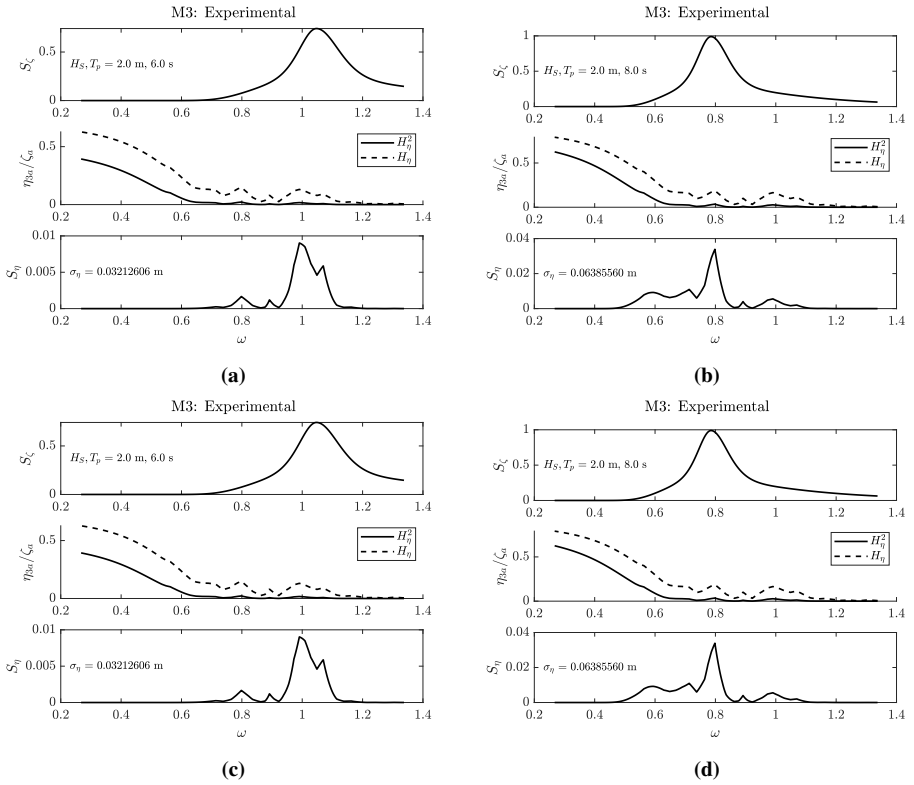

Figure F.37: M3 experimental heave response spectra.

M3, Fore Moonpool

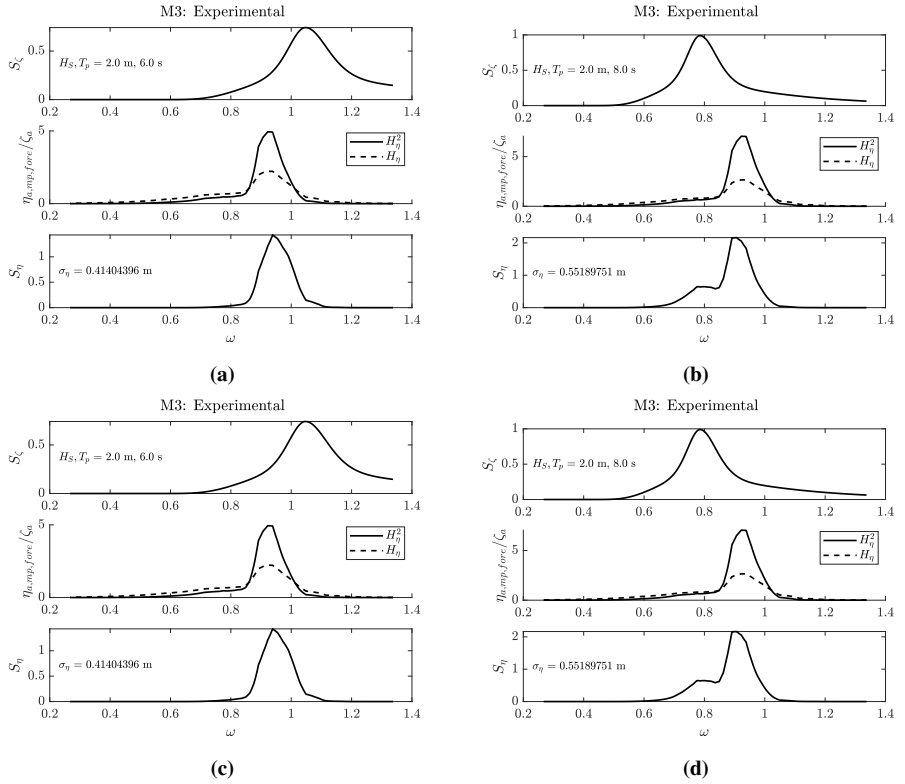

Figure F.38: M3 experimental response spectra for the fore moonpool.

M3, Middle Moonpool

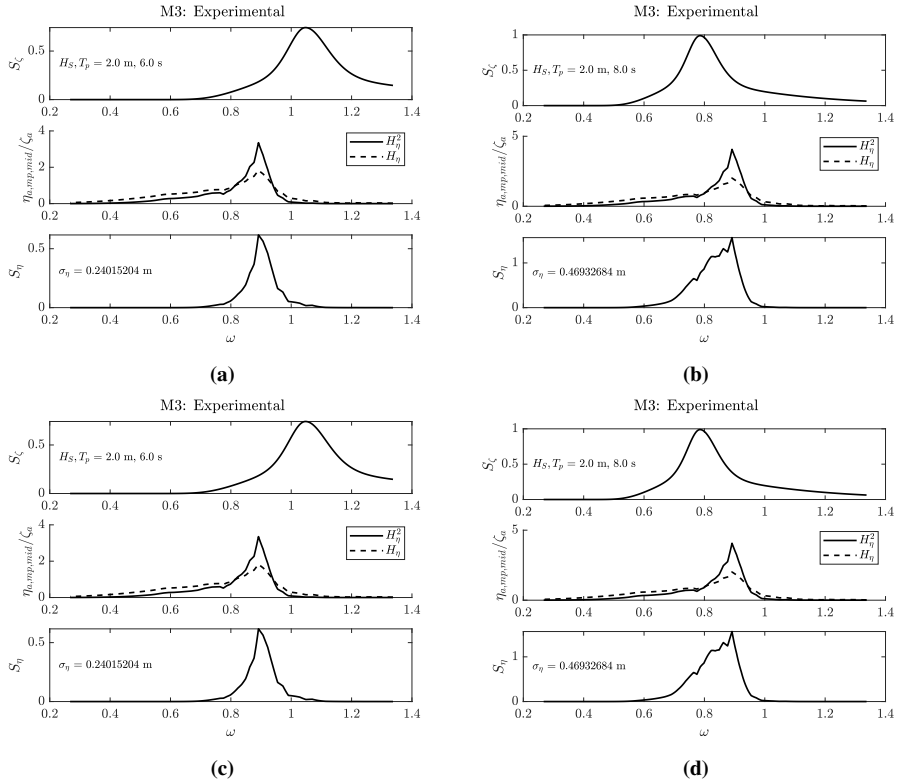

Figure F.39: M3 experimental response spectra for the middle moonpool.

M3, Aft Moonpool

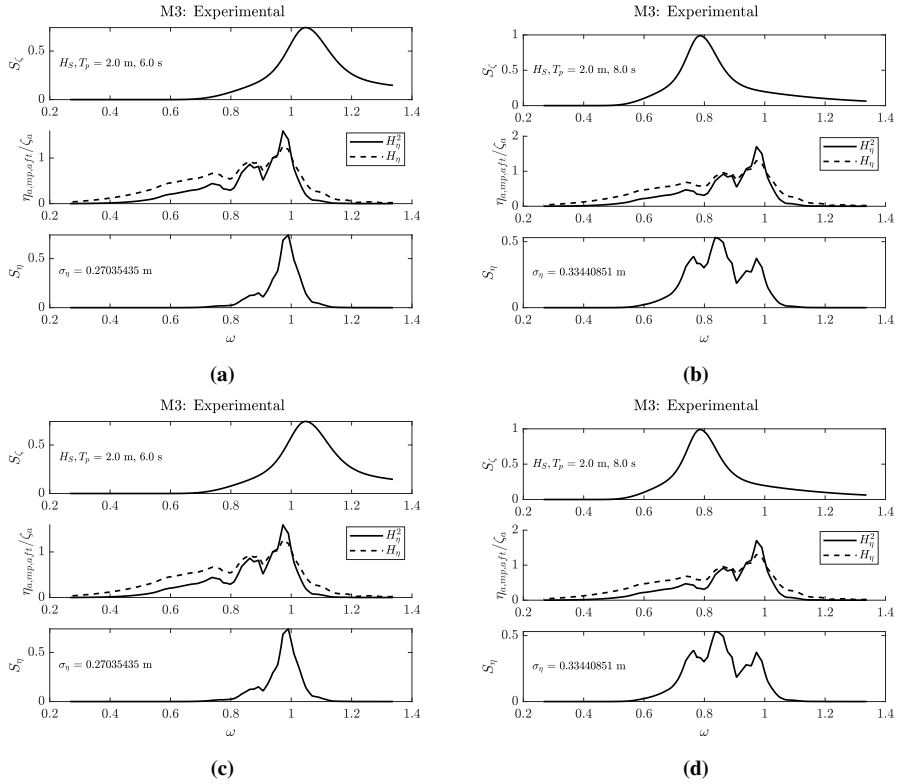

Figure F.40: M3 experimental response spectra for the aft moonpool.

Jonas Ravndal Kildal

Experimental and Numerical Investigation of Coupled Vessel and Moonpool Responses

NTNU
Norwegian University of
Science and Technology